PRECISE THREE-DIMENSIONAL MANIPULATION OF MICROTUBULE FILAMENTS TO PROBE MECHANISMS OF CARGO TRANSPORT

by

Jared Peter Bergman

A dissertation submitted to the faculty of
The University of Utah
in partial fulfillment of the requirements for the degree of

Doctor of Philosphy

Department of Biology

The University of Utah

August 2017

The University of Utah Graduate School

STATEMENT OF DISSERTATION APPROVAL

The dissertation of **Jared Peter Bergman**

has been approved by the following supervisory committee members:

Michael Davidovich Vershinin	, Chair	**5/18/17** Date Approved
Markus Babst	, Member	**5/18/17** Date Approved
Erik Jorgensen	, Member	**5/18/17** Date Approved
Jody Rosenblatt	, Member	**5/18/17** Date Approved
Saveez Saffarian	, Member	**5/18/17** Date Approved

and by **Denise Dearing** , Chair/Dean of

the Department/College/School of **Biology**

and by David B. Kieda, Dean of The Graduate School.

ABSTRACT

Intracellular cargos are shuttled around the cell via molecular motor proteins along their respective filament substrates. For decades, biophysicists have taken advantage of *in vitro* techniques to study fine details of the molecular motor machinery. Today, thanks in large part to *in vitro* experimentation, a great deal is known about the structure-function relationship of various motors, including kinesin-1.

The field is now shifting to investigate how multiple motors work together to transport cargos around the cell's complex microtubule (MT) network. Due to the complexity of the cell's complex biochemical makeup and the heterogeneity of its three-dimensional (3D) MT network, this topic is virtually impossible to address quantitatively in the native cellular environment. Instead, *in vitro* experiments must be used to ensure full control over all relevant variables to study how geometry alone, impacts cargo transport.

Traditional *in vitro* bead assays cannot faithfully model the cell's 3D MT network, and thus cannot be used to test how MT network geometry (orthogonal filament separation, or crossing angle) affects cargo transport. To remedy this, we developed a novel *in vitro* method to manipulate individual MT filaments in 3D with nanometer precision. With this technique, we constructed MT-MT crossings with various geometries to test how separation distance and angle between MT filaments impact transport behaviors of artificial model cargos driven by kinesin-1.

We find that variable separation distance and angle influence cargo navigational behaviors at MT-MT crossings. We also use our experimental data to constrain a 3D simulation to probe aspects of the overall transport system that are not possible to assay experimentally. We propose detailed mechanisms that underlie the MT network's influence on cargo transport.

I dedicate this work to my parents, and to my mentors.

I am forever grateful for their support and tutelage.

TABLE OF CONTENTS

LIST OF FIGURES

Figures

ACKNOWLEDGEMENTS

First and foremost, I would like to acknowledge my doctoral advisor, Dr. Michael Vershinin. Michael, I thank you for taking me under your wing. Thank you for taking a chance on a person without a bachelor's in physics. I know I have come a long, long way from when I first joined the lab. If I can argue with a genius like you, I know must be getting somewhere! If I had to do it all over again, I would. This has been a fabulous developmental experience. I am forever indebted to you.

I also would like to acknowledge my late mentor, Dr. Karl Pfenninger. Not only was Karl an excellent scientific mentor, Karl also assuaged my fears regards moving to Salt Lake City to begin my doctoral studies. I am glad he did, because moving to SLC was an excellent decision. I miss you, Karl.

I would be remiss not to acknowledge Shannon Nielsen who always made sure I followed protocol with regards to committee meetings, health insurance, and graduation! Shannon, you do an excellent job, and I am very happy my organizational deficits were made up for by your supervision. I am sure all the graduate students in the biology department feel the same. You are truly awesome!

To my committee members: Dr. Markus Babst, Dr. Erik Jorgensen, Dr. Jody Rosenblatt, and Dr. Saveez Saffarian: Thank you serving on my committee. At first, the idea of presenting in front of you caused fright, but now I am very grateful for having gone through the "gauntlet," multiple times. I know that if I can stand up in front of four

esteemed scientists, no audience will ever be able to rattle my nerves again… I think the skills that makes me stand out from other scientists is my ability to communicate and present. Thank you for helping me hone those skills.

To my friends, and family: You do not have to ask how much longer I have left anymore! I did it! Completing a PhD. program can be mentally challenging, so I thank you for all the laughs we shared.

To my parents: Thank you for your love and support. Your encouragement did not fall on deaf ears. It has been a bit of an arduous journey, but… we got there! I love you both very, very much.

CHAPTER 1

INTRODUCTION

1.1 Overview

In the eukaryotic cell, many different types of organelles may be considered cargo, i.e., lysosomes, lipid droplets, endosomes, mitochondria. To transport cargo more quickly and/or efficiently than would be possible via diffusion, the cell relies on intricate cytoskeletal networks comprised of actin filaments (AFs) and microtubules (MTs). Cargo motility is made possible by cytoskeletal motors of the kinesin, dynein, and myosin families which can both link cargos to filaments, and produce mechanical force to displace cargos, relative to the filaments.

Many details of the components involved in this system are now understood. Protein structures for actin, tubulin, and many of their polymeric forms have been resolved and their important features mapped. Likewise, structures for many molecular motors are now sufficiently understood to extrapolate structure-function relationships even for large complex motors like cytoplasmic dynein. Overall, single-molecule dynamics are now well understood for many motors, and their respective substrates, through a combination of extremely precise biochemical and biophysical experiments. While many gaps remain to be filled at the single-molecule level, the imperative of our day requires an effort to reconcile our detailed single-molecule understanding with the complex cellular environment in which motors normally function (Ross et al., 2008a).

The cell introduces many layers of complexity, but first consider that intracellular cargos are most likely transported via multiple motors, often by teams of kinesin-1 motors) (Hirokawa et al., 2010). Thus, the transport field has recently shifted to investigate how multiple motors work together to transport cargo (Beeg et al., 2008; Mallik and Gross, 2004; Roux et al., 2002; Vershinin et al., 2007). To study this topic in fine detail,

biophysicists developed deoxyribonucleic acid (DNA) hybridization, antibody-coupling, and DNA origami methods to engineer precise assemblies of motor proteins to study *in vitro* (Derr et al., 2012; Furuta et al., 2013; Goodman and Reck-Peterson, 2014; Xu et al., 2012). These works have been instrumental in understanding how motors coordinate to carry out long distance transport along a single MT, but to understand transport in cells, we must consider another prominent layer of complexity the cellular environment begets: the MT network's geometric heterogeneity.

The MT network is very complex with respect to its three-dimensional (3D) geometry (Bo Huang. et al., 2008). In the 3D environs of a cell, MT filaments can converge at virtually any angle to form MT-MT crosses with extreme separation variability. Thus, in cells, cargos are immersed within a 3D mesh-like array of MT filaments; each of which serves as a potential binding partner. This environment almost ensures the motile cargo, driven by multiple motors, will at some point interact with multiple MTs simultaneously. Indeed, this is regularly seen *in vivo* (Bálint et al., 2013; Mudrakola et al., 2009; Osunbayo et al., 2015).

Near various MT-MT junctions the cargo can potentially disassociate from the original MT filament, giving rise to a switch (Bálint et al., 2013; Osunbayo et al., 2015; Ross et al., 2008b). Corroborating this statement, cargos are known to be transported along multiple distinct MT filaments throughout its intracellular journey (Lakadamyali et al., 2003; Mudrakola et al., 2009). As one could imagine, switches could drastically impact a cargo's transport route. This then begs the question, *How does the geometry of the MT network regulate switching?*

To address the above question, and to gain a better understanding of intracellular

cargo transport, it is paramount to learn how the underlying geometry of the MT network influences cargo navigational outcome at MT-MT crossings. This is an important question to study because aberrant intracellular cargo transport could lead to an imbalance in cargo distribution, which could bring about decreased cellular function, such as in β-cell insulin secretion (Zhu et al., 2015), or neurodegenerative diseases (Hirokawa and Tanaka, 2015)

A recent live cell study set out to investigate MT-MT crossing geometry and how it influences cargo transport behavior (Bálint et al., 2013). By correlating lysosome transport outcomes with MT-MT separation distance, it was suggested that the MT network's 3D geometry significantly influences navigational outcome. Unfortunately, due to the complexity of the cell, a live cell approach has limited effectiveness in identifying how the geometry of the MT network impacts cargo transport. With so many complicating protein factors *in vivo*, both known and unknown, teasing out the exact role MT network geometry plays in regulating transport behavior, is challenging. Thus, this question is well suited to be subjected to a highly controlled *in vitro* investigation.

Although the MT network's 3D geometry is suggested to be a critical regulator of intracellular transport *in vivo*, the topic has received relatively little attention from biophysicists. This is not due to disinterest, but is due to an inability to properly model the cell's 3D MT network *in vitro*. In the few reports where biophysicists addressed this question, they did so by engendering planar networks of MTs on glass surfaces (Ross et al., 2008b; Vershinin et al., 2007). Considering the 3D nature of the cell, it is easy to understand why this approach has limited effectiveness. Glass deposited MTs can only model zero separation MT-MT crossings, and with limited effectiveness (glass slide backings used in traditional bead assays sterically hinders the bead's motion). Although

zero separation scenarios are observed in the cell, a large proportion of crossings fall under the non-zero separation category, as well (Bálint et al., 2013).

We aimed to study how MT network geometry (angle and separation distance) influences cargo transport by experimenting within a simple *in vitro* system that can faithfully model the 3D nature of the MT network in a cell. To accomplish this, we first developed a method to manipulate multiple distinct MT filaments in 3D (Bergman et al., 2015). This operation is performed via precise 3D holographic optical trapping (Sinclair et al., 2004). In essence, we adsorb trappable silica nodes to opposing ends of a MT filament, and then capture and place the nodes precisely in 3D with a holographic optical trap system, so that the MT suspended between them is stretched taut in the desired orientation. With this novel technique, we can construct customizable MT-MT crossings *in vitro*, with respect to crossing angle, and filament separation. With this system, we can then probe how the MT-MT crossing's geometry impacts transport behaviors of a kinesin-1 driven model cargo.

Like the biophysical groups who developed methods to probe new questions regarding multiple motor transport with high precision, we developed a precise method to probe new questions relating to cargo transport upon complex 3D MT-MT crossings. With this experimental setup, we begin to elucidate mechanisms that underlie the differential cargo navigational outcomes observed at variable crossing geometries.

We also collaborate with theoretical physicists who developed a 3D simulation to model cargo transport across MT-MT crossings. We use our experimental data to constrain their computer simulations to gain further insight into our model transport system. With these *in vitro* and *in silico* approaches, we start to build a quantitative model so that we

may begin to extrapolate how various geometric parameters impact cargo routing at simple MT-MT intersections; after all, at its core, the MT cytoskeleton can be explained as a network comprised of a vast series of many individual MT-MT crossings.

Overall, we find that variable crossing geometry (angle and separation parameters) significantly influence cargo transport behaviors. In other words: *various MT network geometries favor specific navigational outcomes*. For example, a cargo that faces a MT-MT crossing with near-zero separation will be much more likely to switch filaments compared to an equivalent cargo that negotiates MT-MT crossings with separation distances on par with the diameter of the cargo. In this introduction, I will (1) introduce motor proteins, microtubules, and (2) discuss previous studies that investigate cargo transport across MT networks. Then I will (3) describe what modifications were implemented in our optical trap system to accommodate 3D MT network construction. I will then (4) discuss the method of 3D MT network construction, (5) consider pragmatic details that potential MT network builders would appreciate, and then (6) discuss our findings regarding how MCs behave at various MT-MT crossings.

1.2 The individual microtubule, and the complex environment in which the microtubule functions

The MT cytoskeleton plays many roles in the cell. The MT network provides structure and support, it serves as the apparatus for chromosomal segregation, and it acts as the highway network for long range intracellular cargo transport via kinesin and dynein family motors. In this MT overview, I will discuss details of the individual MT (superstructure, substructure, dynamic instability), and will consider the vast complexity

of MT network regulating components within the cellular environment (diversity of MT associated proteins). Together, these details will help us to understand and appreciate the inherent difficulties of studying cargo transport within the immeasurably complex intracellular environment.

1.2.1 MT superstructure

The MT is a tubular filament with an outside diameter of ~25nm and an inside diameter of ~15nm (Nogales, 2001). The MT filament is comprised of multiple (8-17 with 13-15 being typical, Hunyadi et al., 2007) protofilaments which can be thought of as "chains" of α/β tubulin subunit dimers which polymerize in repeating, head-to-tail fashion. These protofilaments arrange to form a hollow, tubular cylinder which can grow many micrometers in length (tens of micrometers).

The MT's tubular structure lends it some unique properties; even though they may appear to be a fragile elongated protein structure, MTs are actually considered rigid filaments. Their persistence length is ~ three orders of magnitude greater than that of an actin filament, and their persistence length is far greater than the actual length of the largest MT filaments (Gittes et al., 1993). The persistence length of the MT scales with its contour length as interactions between longer chains of protofilaments garner increased lateral interactions, which increase persistence length/rigidity (Pampaloni et al., 2006). The cell is suggested to take advantage of the MT's rigidity to use as mechano-transducing agents to stimulate transmembrane channels during osmotically induced cell shrinkage (Prager-Khoutorsky et al., 2014).

1.2.2 MT substructure

Although the α and β subunits only have 40% identity, they have nearly identical structures as the density maps for α and β tubulin are almost completely superimposable (Nogales et al., 1998). Their monomeric structure is very compact, but can be divided into three functional domains: (1) the amino-terminal domain containing the guanine nucleotide-binding region, (2) an intermediate domain containing the taxol-binding site (a very commonly used, small molecule MT-stabilizing agent), and (3) the carboxy-terminal domain, which comprises the binding surface for motor proteins (Nogales et al., 1998).

Both α and β tubulin subunits are GTPase proteins which each bind a single molecule of GTP nucleotide. The binding of GTP to α tubulin at the N site is nonexchangeable, and nonhydrolysable whereas the binding of GTP to β tubulin at the E site is exchangeable and hydrolysable. Only α/β dimers with GTP in their β tubulin E site can be incorporated into a MT, unless taxol is used(Nogales, 2015). After polymerization into a MT filament, the GTP in the β tubulin "exchangeable" site will become hydrolyzed over time (Weisenberg et al., 1976).

GTP hydrolysis in β tubulin is only performed in the polymerized MT form because β tubulin itself lacks the crucial residues to hydrolyze the nucleotide. Hydrolysis of β tubulin GTP is triggered once an additional α/β dimer has been added to the protofilament. The polymerization of an additional dimer leads to GTP hydrolysis in the previously incorporated dimer because the key hydrolytic residues, absent in β tubulin, are contributed by the newly added α tubulin subunit (Nogales et al., 1999). Thus, in a MT, most of the incorporated β tubulin subunits are in the GDP state.

MT polymerization requires GTP-bound α/β tubulin dimer because the dimer acts

like a bent spring, which resists straightening until ushered into a growing MT by GTP-mediated interactions (Rice et al., 2008). Once GTP in β tubulin is hydrolyzed to GDP, the β tubulin subunits would take on a "bent" conformation again, but this conformational change is suppressed by the dimer's incorporation into the whole MT structure. The positive end of the MT is stabilized by the GTP-bound α/β tubulin at the MT's forefront, which is referred to as the GTP cap. These GTP-bound tubulin dimers resist bending, and thus remain in a stable conformation. Their presence at the positive end of the MT forces previously incorporated GDP-bound tubulin dimers to remain "straight."

If the GTP cap is removed, the GDP-bound α/β tubulin dimers tend to depolymerize because they are no longer held "straight." When this happens, the tubulin dimers start to bend, which reduces the strength of lateral interactions between protofilaments, and leads to an unfurling of the MT (Rice et al., 2008). Thus, GTP hydrolysis over time, initiated by MT incorporation, is what allows MTs to be rapidly depolymerized. This mechanism is what gives rise to the dynamic instability phenomenon of the MT. In our experiments, we suppress dynamic instability by addition of taxol, a MT-stabilizing drug. Taxol addition to polymerized microtubules is very common in the *in vitro* motor proteins field.

1.2.3 MT dynamic instability

MT polymerization/depolymerization follows what is called dynamic instability. This means that MTs can exhibit phases of slow growth and rapid shrinkage (Mitchison and Kirschner, 1984). Dynamic instability is important because it serves as a cellular mechanism to remodel the MT network during the cell cycle, or during development (Howard and Hyman, 2003). Dynamic instability is partially dependent upon the guanine

nucleotide status of the tubulin dimers that make up the MT.

In the cell, the GTP cap is actually comprised of patches of tubulin in both the GTP and GDP state. The GTP-bound β tubulin subunits confers a stable MT (Seetapun et al., 2012). This patchwork is possible because hydrolysis of GTP lags behind the binding of new GTP-tubulin and occurs randomly; this lag is what creates a relatively large cap of GTP-tubulin at the microtubule plus end, compared to previous *in vitro* measurements (Carlier and Pantaloni, 1981; Seetapun et al., 2012). The GTP cap can be considered a basal level of regulation. The cell has machinery to further regulate the rates of MT polymerization and depolymerization through certain classes of MT-associated proteins (Howard and Hyman, 2003) like MCAK (mitotic centromere-associated kinesins, depolymerizing agents) and +TIPs (plus-end-binding proteins, stabilizing agents).

1.2.4 Complexity of the MT cytoskeleton

In this section, we must consider the different tubulin isoforms that make up a MT, the posttranslational modifications (PTMs) that tubulin undergo, and consider the multitude of MT-associated proteins (MAPs) found in cells. We already briefly discussed a couple MAPs (MCAK, +TIPs) which regulate the MT's mechanism of dynamic instability, but the cellular environment is extremely complex, and contains a multitude of MAPs which modify the MT track, which we have not yet considered. It is important to consider the diversity of tubulin, PTMs, and MAPs so that one may appreciate the complexity of the MT cytoskeleton.

The cell is an extraordinarily complex environment. In humans, there are eight isoforms of both α and β tubulin, and they are found to have specific distributions in

different cell types (Leandro-García et al., 2010). Some MTs are comprised of heterogenous tubulin isoforms, while others are more homogenous (Miller and Joshi, 1996). To further complicate matters, the cell is known to posttranslationally modify MTs via acetylation, detyrosination, phosphorylation, glutamylation, glycylation, amination, and plays host to a bevy of MAPs, both known, and unknown (Verhey and Gaertig, 2007).

Effects of PTMs are still being elucidated, but we now know that PTMs of tubulin affect, not only dynamics of the microtubules, but also their organization and interaction with other cellular components (Song and Brady, 2015). Due to the complexity of the MT cytoskeletal system, it is very difficult to study the functions of MT PTMs *in vivo*. In the cell, sites of MT PTMs are heterogenous, meaning multiple PTMs can be intermingled or concentrated in distinct domains. Multiple PTMs can even affect the same tubulin dimer (Song and Brady, 2015). Thus, it is virtually impossible to account for all the various PTMs on the MT, especially in a cellular context. Like the heterogeneity of tubulin isoforms, as discussed above, PTMs could be considered an additional layer of MT cytoskeletal complexity. To state "the impact of these layers of complexity are still completely unresolved," is not an overstatement. As if those two layers were not confounding enough, the MT cytoskeletal system has yet another layer of complexity at the MT modification level: the existence of MT-associated proteins (MAPs).

MAPs include a very large group of diverse types of proteins: single long a-helices (stathmin), helical coiled-coils (APC), helical hairpins (XMAP215/ch-TOG), extended random coil (tau) and 3 unrelated globular folds (EB1, CAP-Gly and doublecortin) (Amos and Schlieper, 2005). MAPs, like the ones listed above have been traditionally subject of MT stabilizing/destabilizing studies, but recently more groups have begun to investigate

how their presence on the MT might impact motor transport characteristics.

For example, Tau, a MAP famously implicated in Alzheimer's disease, is known to stabilize MTs (Santarella et al., 2004), but also may serve as an impediment to forward progression for certain motor proteins, like conventional kinesin (Vershinin et al., 2007). To make the matter more complicated, different tau isoforms, of which there are 6 (Buée et al., 2000), have different influence on the motors (Dixit et al., 2008; Sparacino et al., 2014; Vershinin et al., 2007). Other structural proteins such as MAP4 affect seem to impact kinesin transport *in vitro*, but these findings, and Tau findings may not be reflected *in vivo* (Atherton et al., 2013).

Overall, the MT network *in vivo* is extraordinarily complex. To learn about how MT network geometry impacts cargo transport, experiments must be conducted in highly controlled environments which feature little complexity. A controlled environment allows one to make confident assertions about how the system functions. We negate the complexity of the cell's MT network by conducting our 3D MT network geometry experiments in an *in vitro* environment.

1.3 Kinesin-1, a single-molecule perspective

Kinesin-1 is a highly processive MT-based motor protein comprised of two ~960 amino acid "heavy chains" subunits which form homodimers. The heavy chain is comprised of 3 domains: the motor domain, the neck linker, and the tail domain (which is responsible for dimerization of two kinesin heavy chains). This protein is referred to as kinesin-1, or conventional kinesin, due to being the first motor protein discovered to translocate upon purified MTs, *in vitro* (Vale et al., 1985). Kinesin-1, hereafter referred to

simply as kinesin, translocates across the MT in what is known as a “hand over hand” mechanism (Yildiz et al., 2004). Kinesin stepping brings about a net motor displacement of ~8nm, a distance which correlates perfectly with the space between kinesin binding sites (Fehr et al., 2008). This movement is mediated by the motor domain and neck linker.

Approximately one-third of the amino acids that make up kinesin-1 are considered the motor domain. This domain produces force to facilitate MT translocation by hydrolyzing ATP to convert the chemical energy stored in the terminal phosphoanhydride bond, to mechanical energy (Cross, 2016). This energy conversion manifests in a conformational change of heavy chain’s motor domain/neck linker, referred to as the “powerstroke.”

The powerstroke is the motion produced by the neck linker as it docks along the motor domain, enabling the motor to “walk” along the MT. The neck linker is the short peptide sequence that swings forward to generate the powerstroke. The neck linker is a ~14 amino acid sequence at the carboxy-terminus of the motor domain (Rice et al., 1999). The neck linker also serves to “link” the motor domain to the rest of the heavy chain, which dimerizes with the tail domain of its partner to form a stalk-like “coiled-coil.” The coiled-coil is a ~40-55nm long, ~5nm wide projection which serves to associate with kinesin-1’s cargo-binding “light chains” and cargo itself (Cuevas et al., 1992; Friedman and Vale, 1999).

Kinesin-1 steps processively by carefully coordinating its motor domains to function in an “out of phase” cycle (Andreasson et al., 2015). To explain the stepping cycle, imagine kinesin being bound to a MT by one of its heads, while the other is unbound from the MT. The MT-disassociated head is referred to as the tethered head because

although it is not directly bound to the MT, it is indirectly "tethered" to the MT via the bound head. Upon ATP binding, the MT-bound head exerts force to displace the tethered head ~16nm towards the MT's plus end. This 16nm displacement positions the tethered head in very close proximity to the next binding site, along the same protofilament (Yildiz et al., 2004). A successful stepping cycle is considered complete when the tethered head rebinds the MT at the next forward position, and the bound head disassociates from the MT. This cycle then continues in an alternating fashion, until the kinesin molecule completely disassociates from the MT.

Kinesin can advance through this stepping cycle many times before completely dissociating from the MT. *Kinein's extraordinary processivity is still an area of active study*. Kinesin's high processivity (ability to step multiple times in a row) arises from its ability to carefully coordinate its two heads so that at least one head remains directly attached to the MT during the stepping cycle (Toprak et al., 2009). Although kinesin can walk for long distances without completely disassociating from the MT, with every step, there is a ~ 1% chance that the stepping mechanism will fail. The failure seems to occur at the stage when kinesin is in the one-head bound state (Milic et al., 2014). When kinesin "falls off" the MT, this indicates that the bound motor domain detached from the MT lattice before the tethered head was able to bind to the MTs. Since the kinesin can undergo ~100 steps before failure, and each step displaces the dimer's center of mass by ~8nm, a single kinesin can routinely walk for ~800nm before dissociating from the MT. Kinesin's incredible processivity arises from its ability to coordinate its two motor domains by "gating," a mechanism which is still hotly debated (Andreasson et al., 2015; Sindelar, 2011; Yildiz et al., 2008).

To provide a solid foundation on which to understand the intricacies of kinesin, and its processivity, a key motor feature, I will discuss the structure and function of the motor domain and neck linker.

1.3.1 Motor domain

Kinesin-1 binds the MT by its motor domain to translocate across the filament. The motor domain contains an ATPase that drives conformational changes to provide both force to step, and structural changes to modulate kinesin-MT affinity. Although the stepping cycle mechanism has not been completely resolved, much is known about the motor domain's ability to: (1) bind and hydrolyze ATP, (2) bind MTs, (3) exert force, and (4) coordinate heads, to perform processive transport. I will briefly discuss these single-molecule aspects of kinesin-1.

1) Kinesin-1 is a NTPase, meaning it can bind nucleotides (generally ATP), and hydrolyze them to peform work. Unlike other NTPases, like small g-proteins, kinesin structure can amplify small structural changes in the motor domain that modulates the motor domain's MT-affinity, and gives rise to force exertion responsible for swinging the tethered head forward to the next binding site. This is referred to as mechanochemical coupling (Woehlke and Schliwa, 2000). Binding of ATP leads to a conformational change in which two motor domain motifs, "switch 1" and "switch 2" close upon the ATP molecule. This binding event and subsequent "clamshell" closure spur the formation of a salt bridge between key residues Glu236 and Arg 203 which strengthens the "closed state" (Shang et al., 2014). Switch closure facilitates ATP hydrolysis by coordinating the ATP's γ-phosphate and a couple of water molecules to undergo a nucleophilic attack (Parke et al.,

2010). Without the formation of this salt bride (Glu236 and Arg 203), ATP cannot be hydrolyzed normally, and thus, the kinesin cannot step. *As you will find in subsequent chapters of this dissertation, we use this information to our advantage by mutating Glu236 (residue in switch 2), to an alanine to produce a nonmotile kinesin. We use this kinesin mutant as an agent to "glue" MTs to a solid support structure, in our case, a 2um silica microsphere.*

2) Kinesin-1 makes electrostatic interactions with the MT by docking on both α- and β-tubulin monomers, although it may bind mainly to β-tubulin (Marx et al., 2006). These interactions are mediated by a cluster of positively charged residues that reside on Loop 12 and α-helix 5, structural motifs on the MT-facing portion of the motor domain (Woehlke et al., 1997). These positively charged residues interact with multiple negatively charged residues on the MT surface to garner an interaction which is capable of adopting multiple high and low Kinesin-MT affinity states (Uchimura et al., 2006).

Affinity modulation is paramount, because in order to step, "hand over hand," the motor domain must be able to adopt a low MT-affinity state so that the trailing head may dissociarte from the MT, propel forward via the bound head's powerstroke, and then rebind to the MT with high affinity. Kinesin-MT affinity modulation is enabled by conformational changes in the motor domain structure that arise from the current nucleotide-binding state of the motor domain; this affinity modulation mechanism functions in tandem with the powerstroke mechanism to coordinate the heads to walk in a hand-over-hand manner (discussed in next section). The motor domain maintains high affinity for the MT in the nucleotide-free state and ATP-bound state. When ATP hydrolysis occurs, and the inorganic phosphate is released, in the ADP state, the motor

domain adopts a conformation which maintains a low MT-affinity state (Shang et al., 2014).

3) Apart from driving variable MT-affinity states, kinesin's different nucleotide states also bring about conformational changes that generate the powerstroke to propel the tethered head. To step, the tethered Kinesin head is propelled forward by the bound head's neck linker in what is called a "powerstroke." The powerstroke force exertion is powered by the neck linker, a structureless ~ 15 amino acid sequence at the carboxy-terminus of the motor domain (Rice et al., 1999). In the APO state, the neck linker takes the form of a disordered loop, but upon ATP binding and hydrolysis, the neck linker swings forward to dock onto the head domain to form a β-sheet with the N-terminal coverstrand (Khalil et al., 2008) forming the, "cover neck bundle." This neck linker displacement and subsequent docking occurs because ATP binding and hydrolysis exposes a site on the motor domain's side where the disordered neck linker structure complements the coverstrand's amino acid sequence to form a β-sheet. Electrostatic interactions between the neck linker and coverstrand are what drive this large conformational change known as the powerstroke (Cross, 2016). This docking mechanism enables kinesin to exert up to ~ 5 pN of force (Svoboda and Block, 1994). The neck linker's transition from a disordered loop state, to a forward docked "cover neck bundle" state, essentially pulls the trailing tethered head forward to adopt a position close to the next binding site on the MT protofilament. Kinesin's neck linker is only long enough to reach the next binding site on the same protofilament; accordingly, kinesin-1 only steps along a single protofilament (Fehr et al., 2008; Schaap et al., 2011). Recent work suggests that the powerstroke actually happens in two steps: a pre-docked transition state that coordinates with ATP binding, and the fully

docked state that seems to be coordinated with ATP hydrolysis (Milic et al., 2014).

4) Perhaps the most extraordinary feature of kinesin is its ability to walk many steps in a coordinated manner, before encountering a cycle failure. Details of kinesin's processivity have recently been subject to extensive scrutiny (Block, 2007; Thoresen and Gelles, 2008). This topic has not reached consensus, but generally, Kinesin's processivity is attributed to coordination between the heads that is mediated through the neck linkers in what is called intramolecular strain. Essentially, the strain is believed to regulate the motor domain's ability to bind ATP, or release inorganic phosphate. This mechanism is what allows kinesin to coordinate its movements to retain high processivity.

1.4 Transport via multiple kinesin motors

Kinesin has been studied from a single-molecule perspective for decades. From this vantage point, many exquisite details of its function have been discovered, as discussed in previous sections. At the single-molecule level, there only remain a few more mysteries regarding kinesin's structure and function, the largest mystery being kinesin's ability to walk processively. Fortunately, for biophysicists in the motors field, there are still many more decades of work to understand how kinesins function together at the multiple motor level to transport cargos around the cell. Multiple motors of various types are used to effectively distribute cargos in an ordered fashion (Levi et al., 2006). Our group and many others are now attempting to discern the various mechanisms that underlie this feat.

Organized intracellular cargo distribution is undoubtedly made possible by various layers of cellular regulation. I have mentioned in the microtubule section how the MT structure, and its associated structural proteins can regulate motor transport by modulating

motor-filament affinities, but we have not yet considered how the composition of a cargo's motor assembly can affect transport. This is an important topic to consider because in cells, motor proteins are often found to function in cooperative teams comprised of various motor types (Gross et al., 2007; Hendricks et al., 2012; Kural et al., 2005). It has also been suggested that intracellular cargo transport is regulated by the coordination of motors in various assemblies (Mallik et al., 2013).

Single-molecule investigations of motor proteins have informed our understanding of how motors may function in ensembles, but these results cannot be used exclusively to extrapolate how multiple motor cooperate; this is due to geometric complexity associated with a multiple motor system. Contemplating the role of cargo shape and motor distributions will help the reader appreciate why it is important to move past single-molecule investigations of motors. The field has begun to conduct experiments that study how multiple motor proteins work together to transport cargos through the MT network.

Studying how motors function together is very difficult due to many confounding factors. Many of the difficulties arise from the intrinsic three dimensionalities of transport systems. Cargos in cells are obviously not point objects, so one must consider the geometry of the cargo, and the geometry of the motors distributed on the cargo's surface. Although a few works have published electron micrographs of intracellular cargos with what appears to be native motors on the cargo (Ashkin et al., 1990; Hirokawa, 1996), we still do not have a solid idea of how motors are truly distributed on cargos. *Are motors on intracellular cargos clustered? Are they evenly distributed? How close are they situated to each other?* All of these factors impact how a cargo would interact with MT filaments in its environment.

To address this, scientists began to purposefully incubate beads with higher concentrations of motor protein to ensure that when beads bound to MTs, there was a high probability of transport being mediated by multiple motors. Indeed, placing enough motors on a cargo will allow multiple motors to work together as they progress along the MT.

Model cargos driven by multiple motors are able to travel for longer distances than cargos driven by a single motor (Block et al., 1990; Vershinin et al., 2007). Vershinin et al. (2007) proposed that multiple motors can transport a cargo much for much longer distances because of the way cooperative motors compensate for each other's failures (MT-dissociation). In a tandem team, if one motor dissociates from the MT, the neighboring kinesin-1 motor may continue to walk along the MT, which serves to tether the cargo to the MT. This tethering effect would keep the bead in close proximity to the MT, which would allow the detached kinesin to rebind. Thus, a cooperative team of multiple motors can travel for extraordinarily long distances. The mean field model suggests the formula: $5^{N-1}/N$ to predict run lengths for various numbers of motors involved, with N being the maximal number of motors involved (Klumpp and Liposky, 2005). In reality, this model does not reflect how motors truly cooperate to share load (Kunwar et al., 2008), but serves a good first order approximation for how increased number of motors can quickly increase run lengths.

To further investigate how multiple motors work together, various biophysical labs developed various, yet similar methods, to precisely forge one-dimensional arrays of various motor protein assemblies (Furuta et al., 2013; Goodman and Reck-Peterson, 2014; Rogers et al., 2009). Currently, with standard bead-motor protein incubation techniques, it is challenging to understand how many motors are on the bead, and how they are

distributed. Groups concerned with single molecule experiments have in the past relied on a bead binding fraction of 30% to confidently state that they were testing exclusively the behavior of a single molecule. Currently, bead binding fractions are only a reliable way to tell if only a single motor is bound to the motor. At higher binding fractions, i.e., 60%, it is difficult to know how many motors can team-up walk along a MT simultaneously. This problem has recently been examined (Li et al., 2016).

1.5 Commentaries on prior reports pertaining to cargo transport through MT-MT intersections

The topic of the 3D MT network geometry, and its impact on cargo transport, is a relatively new subject area. So far, only a few groups have conducted experiments to investigate this problem. It is important to discuss the results and methods of these reports, so that the reader of this dissertation will have a better understanding of the current state of the field.

Out of the handful (~ 4) of papers that consider cargo transport through networks of cytoskeletal filaments, I will discuss two papers which focused exclusively on motor transport behaviors at MT-MT crossings: Ross et al. (2008), and Balint et al. (2013). These two papers provide insight into this problem, but their approaches neglected key aspects of the cell's complexity

1.5.1 Commentary on Ross et al. (2008)

In this paper, the group created planar crisscross arrangements of MTs on glass surface via biotin-streptavidin-biotin linkages to study how single motors, and model

cargos (laden with multiple motors), navigate through MT-MT intersections. The orientation of the MT-MT intersection (which MT is on top, which MT is on bottom) was controlled by flowing MT filaments into the flow chamber in 2 different steps. MTs that were flowed first aligned in one orientation, while a second wave of MT filaments were flowed in so that they would adopt an arrangement perpendicular to the filaments that were first introduced. In this way, Ross et al. (2008) could confidently state which MT served as the "overpass" filament and which served as the "underpass" filament.

The group then recorded navigational outcomes of either, single K560 motors, or ensembles of K560 motors (attached to polystyrene beads) with respect to the overpass/underpass filament orientation. *It is important to note that K560 motors do not have a full length coiled-coil domain; this is an important geometric feature which most likely impact cargo transport.* Ross et al. (2008) also investigated single dynein-dynactin motors and ensembles of dynein-dynactin, but I will just discuss their kinesin results, because my work used kinesin-1 exclusively.

This group first set out to observe how single motors would navigate through a MT-MT crossing. They found that single truncated kinesin-1 motors (K560), could display 4 different behaviors: pass, pause, switch, or disassociate. A transport event was scored a "pass" if the motor moved at least 300nm beyond the intersection. A "pause" event was recorded if the motor spent at least 1 sec at the intersection (did not move 300nm out of the intersection zone). A "switch" was recorded if the motor moved out of the intersection zone (300nm) on the transverse filament. And, a "disassociation" event was tallied if the fluorescent signal vanished near the intersection. It is important to consider the transport event scoring rules to highlight the uncertainty inherent within their system.

The group observed that the two most prominent behaviors for single K560 motors was passing, or disassociation. The incidence of these rates was significantly influenced by the orientation of the intersection, i.e., whether the motor started on the overpass or underpass MT. They found that passing was more prevalent when the motor started on the overpass, and that disassociation was more common when the motor started on the underpass. In their single motor analysis, pausing and switching were observed, but only a fraction of the time (~7% for both overpass/underpass orientations).

Considering the geometry of the planar intersections, the geometry of K560, and the processive characteristics of a single K560 motor, the high rates of passing and disassociation they detected are expected. Also worth noting, K560 was much less likely to switch to the transverse filament when compared to dynein-dynactin, which has a much larger size, and larger stride. They state: “Kinesin, with its smaller stride length, and straight path, is less likely to switch. It is more likely to remain on an individual protofilament and pass the intersection without influence from the intersection microtubule” (Ross et al., 2008b).

Based on kinesin’s single protofilament procession behavior (Shibata et al., 2012), it is not surprising that passes were prevalent when the kinesin started on the overpass. In this configuration, K560 is unlikely to interact with the crossing MT, resulting in a pass. It takes a little imagination, but if one considers K560’s small size, and the geometry of the planar MT-MT crossing, one can easily envision how a single truncated motor protein would be able to “pass” even if the motor starts on the underpass MT. Ross et al. (2008) propose that the truncated motor protein (proceeding upon the underpass MT) could completely avoid the overpass MT obstacle if it proceeds upon one of the MT’s ~13

protofilaments which are not in contact with the overlying MT. Overall, the behaviors observed for single kinesin motors are not surprising, and the mechanisms to describe the observed results are logical.

Like the single K560 motor, ensembles of K560 motors on .8μm polystyrene bead scaffolds (used as artificial intracellular cargo models) also display the same types of navigational outcomes, but with vastly different rates of prevalence. In the "multiple motor bead assay" section of the article, Ross et al. (2008) vary the concentrations of motor proteins on the bead to test how bead-motor concentration, impacts cargo transport at planar MT-MT crossings. They observed that a bead traveling on the overpass MT displays similar outcome rates when compared to the single motor assays, but the story changes drastically when considering the K560 driven model cargos that proceed upon the underpass MT.

Switch outcomes are much more prevalent when their model cargo travels upon the underpass MT. In their experiments, this rate was largely independent of motor concentration. Switching was far more prominent in the underpass geometry because motors on the cargo surface are more likely to interact with the transverse MT; cargos traveling along the overpass MT, are much less likely to interact the crossing MT due to the system architechture. When the bead comes into proximity of the transverse MT, a subset of the bead's motors will have the opportunity to engage the transverse MT. When motors engage the transverse MT, the cargo may switch from one filament to the other. The authors propose two mechanisms for the "apparent cooperativity between kinesin motors," that lead to switching. One mechanism suggests that the kinesin motors walking on the underpass MT would disassociate once they encountered the transverse MT, which

would lead to a switch if a group of motors had already engaged the transverse MT. The other mechanism suggests that the motors are coordinated through strain that is generated by the two motor teams trying to proceed in two different directions. Overall, the authors propose that the mechanisms are not mutually exclusive, and that switch rates are elevated for motors walking on the underpass MT because, "the bead would interact with both MTs easily in that situation." This paper certainly offers insight into the mechanisms of filament switching, but there are problems inherent in the traditional bead assay system they employed.

The first problem to consider is the method in which the MT networks were engendered. Like stated above, the MT filaments were deposited onto a glass surface. Apart from sterically hindering the model cargo with a glass surface, another drawback of this system is its inability to model MT intersections with separations greater than zero. Although near-zero separation intersections are found in cells, MT filaments exist in many different planes (Bo Huang et al., 2008). Hence, this method employed by Ross et al. (2008) is only able to model this one specific scenario that occurs in the cellular environment. To address this methodological pitfall, we developed a technique to conduct similar experiments in a system that enables one to create MT-MT crossings with customizable separation, and angle.

Another shortcoming of Ross et al. (2008) is that they relied on slow fluorescent imaging techniques. For the single K560 experiments, they recorded 2 FPS, and for the bead assay experiments, they recorded at 4 FPS. At such slow frame rates, the fast dynamics of the transport events cannot be resolved, which reduces the experimental power of the system. In our experiments, we chose to not rely on slow fluorescent imaging, and

instead chose to record with standard brightfield imaging. This enabled us to record videos at 20 FPS, and localize particle positions with sub-100nm precision. This imaging method provided enough spatiotemporal resolution to observe intricate cargo dynamics associated with MT intersection navigation.

Another experimental drawback of Ross et al. (2008) to highlight is their use of a truncated kinesin-1 motor. K560 is a popular construct to employ in single molecule studies due to ease of production, and inability to self-inhibit (due to lack of tail); but K560's geometry is inherently different than natural full length kinesin-1. K560 is much shorter (Shishido et al., 2010) than full length kinesin, which would most likely how the cargo navigates at intersections. To negate this concern, we employed full-length kinesin constructs.

I deemed it necessary to write this commentary because it helps the reader appreciate the reasons why we invested considerable resources and time to develop our unique, "suspended MT" bead assay system.

1.5.2 Commentary on Balint et al. (2013)

This report originated from a group whose traditional focus is not intracellular transport. Balint et al. (2013), showcased a new method the group had developed: a live cell particle tracking system featuring post-hoc specimen fixation in conjunction with correlative 3D super-resolution fluorescence microscopy.

Specifically, this group tracked the fluorescent signature of lysosomes in African green monkey kidney cells via epifluorescent microscopy. As the lysosomes shuttled around the cellular environment, their trajectory was recorded at a relatively slow temporal

resolution (2 FPS), but since they resolved single lysosomes in a lysosome-sparse environment, the group was able to precisely localize the particle in 2D space.

After tracking a few lysosome trajectories around the cell, the imaged cell was immediately fixated via 3% volume/volume paraformaldehyde and 0.1% glutaraldehyde. In this way, the group could preserve the underlying MT network in order to perform the slow process of 3D stochastic optical reconstruction microscopy (3D STORM). The authors claim their STORM system is capable of 20 nm resolution in the lateral plane, and 55 nm resolution in the axial plane. Thus, with this experimental approach, the group could track the path of the lysosome cargos, and then place their trajectory ontop of a 3D map of the MT network. This allowed the group to correlate lysosome navigational behaviors with the underlying topology of the 3D MT network.

In their analysis, they found that intracellular cargo transport, displayed in their cells, exhibited behaviors similar to those observed in *in vitro* experiments by Ross et al. (2008). Lysosomes were seen passing, switching, pausing, and reversing at MT-MT intersections. Pausing behaviors, which they defined as having "no net centroid position displacement for 1 sec or longer," correlated strongly with the smallest separation distances they could resolve (<100 nm). From this correlation, the authors suggest that the near-zero separation intersections give rise to "pauses" because the crossing MT will act as an obstacle to the motor(s) moving along the primary MT. Usually, the paused cargos eventually navigate through the intersection, either passing, switching, or dissasociating.

This paper serves as an excellent reference for our study, because it highlights the importance of the MT network's geometry in cargo transport. Due to the methods employed, this report is unable to delve deep into the mechanisms underlying the

navigational behaviors they observed. Although their system is novel, and advanced, it cannot overcome the uncertainties associated with the highly complex cellular environment

First, even though their spatial resolution is relatively precise, it is unable to perfectly resolve various important features associated with the MT network system. For example, although their set up can resolve spacing (in the z-axis) between MTs with ~55nm accuracy, they were unable to determine the polarity of the MTs, or the orientation of the lysosome cargo, in relation to the MT-MT intersection. In other words: *does the cargo actually encounter the crossing MT? Is the cargo in question situated between the intersecting MTs?* For example, the lysosome could skirt the intersection by traveling in a 3D zone which does not impinge the crossing MT. This geometric information, which they could not resolve, is critical when attempting to elucidate the mechanisms of transport through a MT network. Also, due to their dependence on fluorescence, their acquisition speeds were too slow to resolve fine cargo dynamics. Overall, although their data suggest MT network geometry is paramount, they can only offer a very simplistic model for how MT network geometry impacts cargo transport. This is because they cannot resolve high levels of detail.

This analysis of Balint et al. (2013) was included to highlight the complexity of the cellular environment, and to help the reader understand why we employed a controlled *in vitro* approach to ask a similar question: *how does MT network geometry impact cargo transport?*

1.6 References

Amos, L.A., and Schlieper, D. (2005). Microtubules and maps. Adv. Protein Chem. *71*, 257–298.

Andreasson, J.O.L., Milic, B., Chen, G.Y., Guydosh, N.R., Hancock, W.O., and Block, S.M. (2015). Examining kinesin processivity within a general gating framework. Elife *2015*, 1–44.

Ashkin, A., Schütze, K., Dziedzic, J.M., Euteneuer, U., and Schliwa, M. (1990). Force generation of organelle transport measured in vivo by an infrared laser trap. Nature *348*, 346–348.

Atherton, J., Houdusse, A., and Moores, C. (2013). MAPping out distribution routes for kinesin couriers. Biol. Cell *105*, 465–487.

Bálint, Š., Verdeny Vilanova, I., Sandoval Álvarez, Á., and Lakadamyali, M. (2013). Correlative live-cell and superresolution microscopy reveals cargo transport dynamics at microtubule intersections. Proc. Natl. Acad. Sci. U. S. A. *110*, 3375–3380.

Van Battum, E.Y., Brignani, S., and Pasterkamp, R.J. (2015). Axon guidance proteins in neurological disorders. Lancet Neurol. *14*, 532–546.

Beeg, J., Klumpp, S., Dimova, R., Gracià, R.S., Unger, E., and Lipowsky, R. (2008). Transport of Beads by Several Kinesin Motors. Biophys. J. *94*, 532–541.

Bergman, J., Osunbayo, O., and Vershinin, M. (2015). Constructing 3D microtubule networks using holographic optical trapping. Sci. Rep. *5*, 18085.

Block, S.M. (2007). Kinesin motor mechanics: binding, stepping, tracking, gating, and limping. Biophys. J. *92*, 2986–2995.

Block, S.M., Goldstein, L.S., and Schnapp, B.J. (1990). Bead movement by single kinesin molecules studied with optical tweezers. Nature *348*, 348–352.

Bo Huang, Wenqin Wang, Mark Bates, and X.Z. (2008). Three-dimensional Super-resolution Imaging by Stochastic Optical Reconstruction Microscopy. Science (80-.). *319*, 810–813.

Buée, L., Bussière, T., Buée-Scherrer, V., Delacourte, A., and Hof, P.R. (2000). Tau protein isoforms, phosphorylation and role in neurodegenerative disorders. Brain Res. Rev. *33*, 95–130.

Carlier, M.F., and Pantaloni, D. (1981). Kinetic analysis of guanosine 5'-triphosphate hydrolysis associated with tubulin polymerization. Biochemistry *20*, 1918–1924.

Chesarone, M. a, DuPage, A.G., and Goode, B.L. (2010). Unleashing formins to

remodel the actin and microtubule cytoskeletons. Nat. Rev. Mol. Cell Biol. *11*, 62–74.

Cross, R.A. (2016). Review: Mechanochemistry of the kinesin-1 ATPase. Biopolymers *105*, 476–482.

Cuevas, M. De, Tao, T., and Goldstein, L.S.B. (1992). Evidence That the Stalk of Drosophila Kinesin Heavy Chain Is an a-Helical Coiled Coil. J. Cell Biol. *116*, 957–965.

Derr, N.D., Goodman, B.S., Jungmann, R., Leschziner, A.E., Shih, W.M., and Reck-Peterson, S.L. (2012). Tug-of-War in Motor Protein Ensembles. Science (80-.). *338*, 662–666.

Desai, A., and Mitchison, T.J. (1997). Microtubule Polymerization Dynamics. Annu. Rev. Cell Dev. Biol. *13*, 83–117.

Dixit, R., Ross, J.L., Goldman, Y.E., and Holzbaur, E.L.F. (2008). Differential Regulation of Dynein and Kinesin Motor Proteins by Tau. Science (80-.). *319*, 8–11.

Dong, B., Yang, X., Zhu, S., Bassham, D.C., and Fang, N. (2015). Stochastic Optical Reconstruction Microscopy Imaging of Microtubule Arrays in Intact Arabidopsis thaliana Seedling Roots. Sci. Rep. *5*, 15694.

Dumontet, C., Durán, G.E., Steger, K.A., Murphy, G.L., Sussman, H.H., and Sikic, B.I. (1996). Differential expression of tubulin isotypes during the cell cycle. Cell Motil. Cytoskeleton *35*, 49–58.

Erickson, R.P., Jia, Z., Gross, S.P., and Yu, C.C. (2011). How molecular motors are arranged on a cargo is important for vesicular transport. PLoS Comput. Biol. *7*.

Erickson, R.P., Gross, S.P., and Yu, C.C. (2013). Filament-Filament Switching Can Be Regulated by Separation Between Filaments Together with Cargo Motor Number. PLoS One *8*, 1–8.

Fehr, A.N., Asbury, C.L., and Block, S.M. (2008). Kinesin steps do not alternate in size. Biophys. J. *94*, L20-2.

Fink, G., Hajdo, L., Skowronek, K.J., Reuther, C., Kasprzak, A.A., and Diez, S. (2009). The mitotic kinesin-14 Ncd drives directional microtubule-microtubule sliding. Nat. Cell Biol. *11*, 717–723.

Friedman, D.S., and Vale, R.D. (1999). Single-molecule analysis of kinesin motility reveals regulation by the cargo-binding tail domain. Nat. Cell Biol. *1*, 293–297.

Furuta, K., Furuta, A., Toyoshima, Y.Y., Amino, M., Oiwa, K., and Kojima, H. (2013). Measuring collective transport by defined numbers of processive and nonprocessive kinesin motors. Proc. Natl. Acad. Sci. U. S. A. *110*, 501–506.

Galmarini, C.M., Kamath, K., Vanier-Viornery, A., Hervieu, V., Peiller, E.,

Falette, N., Puisieux, A., Ann Jordan, M., and Dumontet, C. (2003). Drug resistance associated with loss of p53 involves extensive alterations in microtubule composition and dynamics. Br. J. Cancer *88*, 1793–1799.

Gittes, F., Mickey, B., Nettleton, J., and Howard, J. (1993). Flexural rigidity of microtubules and actin filaments measured from thermal fluctuations in shape. J. Cell Biol. *120*, 923–934.

Gomez, J.M., Chumakova, L., Bulgakova, N.A., and Brown, N.H. (2016). Microtubule organization is determined by the shape of epithelial cells. Nat. Commun. *7*, 13172.

Goodman, B.S., and Reck-Peterson, S.L. (2014). Engineering defined motor ensembles with DNA origami (Elsevier Inc.).

Gross, S.P., Welte, M.A., Block, S.M., and Wieschaus, E.F. (2002). Coordination of opposite-polarity microtubule motors. J. Cell Biol. *156*, 715–724.

Gross, S.P., Vershinin, M., and Shubeita, G.T. (2007). Cargo transport: two motors are sometimes better than one. Curr. Biol. *17*, R478-86.

Hamant, O. (2013). Cell biology: Cytoskeleton network topology feeds back on its regulation. Curr. Biol. *23*, R963–R965.

Hendricks, A.G., Holzbaur, E.L.F., and Goldman, Y.E. (2012). Force measurements on cargoes in living cells reveal collective dynamics of microtubule motors. Proc. Nat. Acad. Sci. *109*, 18447–18452.

Hirokawa, N. (1996). The molecular mechanism of organelle transport along microtubules: the identification and characterization of KIFs (kinesin superfamily proteins). Cell Struct. Funct. *21*, 357–367.

Hirokawa, N., and Tanaka, Y. (2015). Kinesin superfamily proteins (KIFs): Various functions and their relevance for important phenomena in life and diseases. Exp. Cell Res. *334*, 16–25.

Hirokawa, N., Shiomura, Y., and Okabe, S. (1988). Tau proteins: the molecular structure and mode of binding on microtubules. J. Cell Biol. *107*, 1449–1459.

Hirokawa, N., Niwa, S., and Tanaka, Y. (2010). Molecular motors in neurons: Transport mechanisms and roles in brain function, development, and disease. Neuron *68*, 610–638.

Howard, J., and Hyman, A.A. (2003). Dynamics and mechanics of the microtubule plus end. Nature *422*, 753–758.

Hunyadi, V., Chrétien, D., Flyvbjerg, H., and Jánosi, I.M. (2007). Why is the microtubule lattice helical? Biol. Cell *99*, 117–128.

Kalil, K., and Dent, E.W. (2014). Branch management: mechanisms of axon branching in the developing vertebrate CNS. Nat. Rev. Neurosci. *15*, 7–18.

Khalil, A.S., Appleyard, D.C., Labno, A.K., Georges, A., Karplus, M., Belcher, A.M., Hwang, W., and Lang, M.J. (2008). Kinesin's cover-neck bundle folds forward to generate force. Proc. Natl. Acad. Sci. U. S. A. *105*, 19247–19252.

Klumpp, S., and Liposky, R. (2005). Cooperative cargo transport by several molecular motors. Proc. Natl. Acad. Sci. U. S. A. *102*, 17284–17289.

Kunwar, A., Vershinin, M., Xu, J., and Gross, S.P. (2008). Stepping, Strain Gating, and an Unexpected Force-Velocity Curve for Multiple-Motor-Based Transport. Curr. Biol. *18*, 1173–1183.

Kural, C., Kim, H., Syed, S., Goshima, G., Gelfand, V.I., and Selvin, P.R. (2005). Kinesin and dynein move a peroxisome in vivo: a tug-of-war or coordinated movement? Science *308*, 1469–1472.

Lakadamyali, M., Rust, M.J., Babcock, H.P., and Zhuang, X. (2003). Visualizing infection of individual influenza viruses. Proc. Natl. Acad. Sci. U. S. A. *100*, 9280–9285.

Leandro-García, L.J., Leskelä, S., Landa, I., Montero-Conde, C., López-Jiménez, E., Letón, R., Cascón, A., Robledo, M., and Rodríguez-Antona, C. (2010). Tumoral and tissue-specific expression of the major human alpha/beta-tubulin isotypes. Cytoskeleton *67*, 214–223.

Levi, V., Serpinskaya, A.S., Gratton, E., and Gelfand, V. (2006). Organelle transport along microtubules in Xenopus melanophores: evidence for cooperation between multiple motors. Biophys. J. *90*, 318–327.

Li, Q., King, S.J., Gopinathan, A., and Xu, J. (2016). Quantitative Determination of the Probability of Multiple-Motor Transport in Bead-Based Assays. Biophys. J. *110*, 2720–2728.

Mallik, R., and Gross, S.P. (2004). Molecular motors: Strategies to get along. Curr. Biol. *14*, 971–982.

Mallik, R., Rai, A.K., Barak, P., Rai, A., and Kunwar, A. (2013). Teamwork in microtubule motors. Trends Cell Biol. *23*, 575–582.

Marx, A., Müller, J., Mandelkow, E.M., Hoenger, A., and Mandelkow, E. (2006). Interaction of kinesin motors, microtubules, and MAPs. J. Muscle Res. Cell Motil. *27*, 125–137.

McKenney, R.J., Vershinin, M., Kunwar, A., Vallee, R.B., and Gross, S.P. (2010). LIS1 and NudE induce a persistent dynein force-producing state. Cell *141*, 304–314.

Milic, B., Andreasson, J.O.L., Hancock, W.O., and Block, S.M. (2014). Kinesin processivity is gated by phosphate release. Proc. Natl. Acad. Sci. U. S. A. *111*, 14136–14140.

Miller, K.E., and Joshi, H.C. (1996). Tubulin transport in neurons. J. Cell Biol. *133*, 1355–1366.

Mitchison, T., and Kirschner, M. (1984). Dynamic instability of microtubule growth. Nature *312*, 237–242.

Mudrakola, H. V., Zhang, K., and Cui, B. (2009). Optically Resolving Individual Microtubules in Live Axons. Structure *17*, 1433–1441.

Müller, M.J.I., Klumpp, S., Lipowsky, R., Muller, M.J., Klumpp, S., and Lipowsky, R. (2008). Tug-of-war as a cooperative mechanism for bidirectional cargo transport by molecular motors. Proc. Natl. Acad. Sci. USA *105*, 4609–4614.

Nogales, E. (2001). Structural Insights Into Micrtoubule Function. Annu. Rev. Biochem *69*, 277–302.

Nogales, E. (2015). An electron microscopy journey in the study of microtubule structure and dynamics. Protein Sci. *24*, 1912–1919.

Nogales, E., Wolf, S.G., and Downing, K.H. (1998). Structureof the alpha-beta tubulin dimer by electron crystallography. Nature *391*, 199–204.

Nogales, E., Whittaker, M., Milligan, R.A., and Downing, K.H. (1999). High-resolution model of the microtubule. Cell *96*, 79–88.

Osunbayo, O., Butterfield, J., Bergman, J., Mershon, L., Rodionov, V., and Vershinin, M. (2015). Cargo transport at microtubule crossings: Evidence for prolonged tug-of-war between kinesin motors. Biophys. J. *108*, 1480–1483.

Pampaloni, F., Lattanzi, G., Jonás, A., Surrey, T., Frey, E., and Florin, E.-L. (2006). Thermal fluctuations of grafted microtubules provide evidence of a length-dependent persistence length. Proc. Natl. Acad. Sci. U. S. A. *103*, 10248–10253.

Parke, C.L., Wojcik, E.J., Kim, S., and Worthylake, D.K. (2010). ATP hydrolysis in Eg5 kinesin involves a catalytic two-water mechanism. J. Biol. Chem. *285*, 5859–5867.

Parker, A.L., Kavallaris, M., and McCarroll, J.A. (2014). Microtubules and their role in cellular stress in cancer. Front. Oncol. *4*, 153.

Petry, S., Groen, A.C., Ishihara, K., Mitchison, T.J., and Vale, R.D. (2013). Branching microtubule nucleation in xenopus egg extracts mediated by augmin and TPX2. Cell *152*, 768–777.

Di Polo, A. (2015). Dendrite pathology and neurodegeneration: Focus on mTOR. Neural Regen. Res. *10*, 559–561.

Prager-Khoutorsky, M., Khoutorsky, A., and Bourque, C.W. (2014). Unique Interweaved Microtubule Scaffold Mediates Osmosensory Transduction via Physical Interaction with TRPV1. Neuron *83*, 866–878.

Rice, L.M., Montabana, E.A., and Agard, D.A. (2008). The lattice as allosteric effector: structural studies of alphabeta- and gamma-tubulin clarify the role of GTP in microtubule assembly. Proc. Natl. Acad. Sci. U. S. A. *105*, 5378–5383.

Rice, S., Lin, A.W., Safer, D., Hart, C.L., Naber, N., Carragher, B.O., Cain, S.M., Pechatnikova, E., Wilson-Kubalek, E.M., Whittaker, M., et al. (1999). A structural change in the kinesin motor protein that drives motility. Nature *402*, 778–784.

Rogers, A., Driver, Jonathan Constantinou, P., and Diehl, M.R. (2009). Negative interference dominates collective transport of kinesin motors in the absence of load. Phys. Chem. Chem. Phys. *11*, 4800–4803.

Ross, J.L., Ali, M.Y., and Warshaw, D.M. (2008a). Cargo transport: molecular motors navigate a complex cytoskeleton. Curr. Opin. Cell Biol. *20*, 41–47.

Ross, J.L., Shuman, H., Holzbaur, E.L.F., and Goldman, Y.E. (2008b). Kinesin and dynein-dynactin at intersecting microtubules: motor density affects dynein function. Biophys. J. *94*, 3115–3125.

Roux, A., Cappello, G., Cartaud, J., Prost, J., Goud, B., and Bassereau, P. (2002). A minimal system allowing tubulation with molecular motors pulling on giant liposomes. Proc. Natl. Acad. Sci. U. S. A. *99*, 5394–5399.

Santarella, R.A., Skiniotis, G., Goldie, K.N., Tittmann, P., Gross, H., Mandelkow, E.M., Mandelkow, E., and Hoenger, A. (2004). Surface-decoration of microtubules by human tau. J. Mol. Biol. *339*, 539–553.

Schaap, I.A.T., Carrasco, C., De Pablo, P.J., and Schmidt, C.F. (2011). Kinesin walks the line: Single motors observed by atomic force microscopy. Biophys. J. *100*, 2450–2456.

Schnorrenberg, S., Grotjohann, T., Vorbr??ggen, G., Herzig, A., Hell, S.W., and Jakobs, S. (2016). In vivo super-resolution RESOLFT microscopy of drosophila melanogaster. Elife *5*, 1–11.

Seetapun, D., Castle, B.T., McIntyre, A.J., Tran, P.T., and Odde, D.J. (2012). Estimating the microtubule GTP cap size in vivo. Curr. Biol. *22*, 1681–1687.

Shang, Z., Zhou, K., Xu, C., Csencsits, R., Cochran, J.C., and Sindelar, C. V. (2014). High-resolution structures of kinesin on microtubules provide a basis for nucleotide-gated force-generation. Elife *3*, e04686.

Shibata, K., Miura, M., Watanabe, Y., Saito, K., Nishimura, A., Furuta, K., and Toyoshima, Y.Y. (2012). A single protofilament is sufficient to support unidirectional walking of dynein and kinesin. PLoS One *7*.

Shishido, H., Nakazato, K., Katayama, E., Chaen, S., and Maruta, S. (2010). Kinesin-Calmodulin fusion protein as a molecular shuttle. J. Biochem. *147*, 213–223.

Sinclair, G., Jordan, P., Courtial, J., Padgett, M., and Laczik, Z.J. (2004). Assembly of 3 dimensional structures using programmable holographic optical tweezers,. Opt. Express *12*, 5475–5480.

Sindelar, C. V. (2011). A seesaw model for intermolecular gating in the kinesin motor protein. Biophys. Rev. *3*, 85–100.

Song, Y., and Brady, S.T. (2015). Post-translational modifications of tubulin: Pathways to functional diversity of microtubules. Trends Cell Biol. *25*, 125–136.

Sparacino, J., Farias, M.G., and Lamberti, P.W. (2014). Effect of the microtubule-associated protein tau on dynamics of single-headed motor proteins KIF1A. Phys. Rev. E - Stat. Nonlinear, Soft Matter Phys. *89*, 1–8.

Subramanian, R., Wilson-Kubalek, E.M., Arthur, C.P., Bick, M.J., Campbell, E.A., Darst, S.A., Milligan, R.A., and Kapoor, T.M. (2010). Insights into antiparallel microtubule crosslinking by PRC1, a conserved nonmotor microtubule binding protein. Cell *142*, 433–443.

Svoboda, K., and Block, S.M. (1994). Force and velocity measured for single kinesin molecules. Cell *77*, 773–784.

Thoresen, T., and Gelles, J. (2008). Processive movement by a kinesin heterodimer with an inactivating mutation in one head. Biochemistry *47*, 9514–9521.

Toprak, E., Yildiz, A., Hoffman, M.T., Rosenfeld, S.S., and Selvin, P.R. (2009). Why kinesin is so processive. Proc. Natl. Acad. Sci. U. S. A. *106*, 12717–12722.

Uchimura, S., Oguchi, Y., Katsuki, M., Usui, T., Osada, H., Nikawa, J., Ishiwata, S., and Muto, E. (2006). Identification of a strong binding site for kinesin on the microtubule using mutant analysis of tubulin. EMBO J. *25*, 5932–5941.

Vale, R.D., Reese, T.S., and Sheetz, M.P. (1985). Identification of a novel force-generating protein, kinesin, involved in microtubule-based motility. Cell *42*, 39–50.

Verhey, K.J., and Gaertig, J. (2007). The tubulin code. Cell Cycle *6*, 2152–2160.

Vershinin, M., Carter, B.C., Razafsky, D.S., King, S.J., and Gross, S.P. (2007). Multiple-motor based transport and its regulation by Tau. Proc. Natl. Acad. Sci. U. S. A. *104*, 87–92.

Weisenberg, R.C., Deery, W.J., and Dickinson, P.J. (1976). Tubulin-nucleotide interactions during the polymerization and depolymerization of microtubules. Biochemistry *15*, 4248–4254.

Woehlke, G., and Schliwa, M. (2000). Walking on Two Heads: the Many Talents of Kinesin. Nat. Rev. Mol. Cell Biol. *1*, 50–58.

Woehlke, G., Ruby, A.K., Hart, C.L., Ly, B., Hom-Booher, N., and Vale, R.D. (1997). Microtubule interaction site of the kinesin motor. Cell *90*, 207–216.

Xu, J., Shu, Z., King, S.J., and Gross, S.P. (2012). Tuning Multiple Motor Travel via Single Motor Velocity. Traffic *13*, 1198–1205.

Yildiz, A., Tomishige, M., Vale, R.D., and Selvin, P.R. (2004). Kinesin walks hand-over-hand. Science *303*, 676–678.

Yildiz, A., Tomishige, M., Gennerich, A., and Vale, R.D. (2008). Intramolecular Strain Coordinates Kinesin Stepping Behavior along Microtubules. Cell *134*, 1030–1041.

Young, K.G., Thurston, S.F., Copeland, S., Smallwood, C., and Copeland, J.W. (2008). INF1 is a novel microtubule-associated formin. Mol. Biol. Cell *19*, 5168–5180.

Zhu, X., Hu, R., Brissova, M., Stein, R.W., Powers, A.C., Gu, G., and Kaverina, I. (2015). Microtubules Negatively Regulate Insulin Secretion in Pancreatic Beta Cells. Dev. Cell *34*, 656–668.

CHAPTER 2

CONSTRUCTING 3D MICROTUBULE NETWORKS USING HOLOGRAPHIC OPTICAL TRAPPING

Reprinted from Bergman, J., Osunbayo, O., Vershinin, M. Constructing 3D microtubule networks using holographic optical trapping. Scientific Reports 5, article number 18085 2015. With permission from Nature Publishing Group.

www.nature.com/scientificreports

SCIENTIFIC REPORTS

OPEN

Constructing 3D microtubule networks using holographic optical trapping

Received: 09 September 2015
Accepted: 11 November 2015
Published: 10 December 2015

J. Bergman, O. Osunbayo & M. Vershinin

Developing abilities to assemble nanoscale structures is a major scientific and engineering challenge. We report a technique which allows precise positioning and manipulation of individual rigid filaments, enabling construction of custom-designed 3D filament networks. This approach uses holographic optical trapping (HOT) for nano-positioning and microtubules (MTs) as network building blocks. MTs are desirable engineering components due to their high aspect ratio, rigidity, and their ability to serve as substrate for directed nano-transport, reflecting their roles in the eukaryotic cytoskeleton. The 3D architecture of MT cytoskeleton is a significant component of its function, however experimental tools to study the roles of this geometric complexity in a controlled environment have been lacking. We demonstrate the broad capabilities of our system by building a self-supporting 3D MT-based nanostructure and by conducting a MT-based transport experiment on a dynamically adjustable 3D MT intersection. Our methodology not only will advance studies of cytoskeletal networks (and associated processes such as MT-based transport) but will also likely find use in engineering nanostructures and devices.

Precisely constructed networks of rigid filaments are of broad interest. MTs are intriguing building blocks for nanoscale construction and mechanical engineering due to their small diameter, high rigidity and ability to sustain directed transport. For example, biomimetic engineering applications are starting to adopt MT-based motility to route and deliver nanoscale cargo[1–4] but are severely limited by the lack of suitable nano-assembly techniques. Traditional *in vitro* approaches predominantly feature MTs fixed to a flat (typically coverslip) surface. Pillars and ridges on the coverslip surface have been used to produce suspended MTs that overhang freely or bridge several attachment points[5,6]. Such techniques are sufficient to sustain basic nano-transport but are neither flexible nor precise. Filaments cannot be positioned or re-positioned as needed, and 3D layouts are either impossible to achieve or highly restricted. Thus, existing approaches do not allow one to construct custom designed networks (whether the design is biologically inspired or technologically required).

Interest in constructing MT networks is further motivated by their importance in biological research. MT cytoskeletal networks in living cells are critical for tasks such as cell organization, and cargo transport. Despite this, the complexity of the 3D network and its role in cargo routing remains poorly characterized. It is often necessary to study cytoskeletal processes under controlled conditions[7] but current *in vitro* techniques are unable to model complex 3D networks[8,9]. For example, cargo distribution within living cells cannot be fully understood without taking into account the cytoskeleton's 3D nature e.g.[10,11]. *In vivo* research is advancing rapidly to accommodate this need. Live cell 3D particle tracking techniques are steadily growing in number and sophistication e.g.[12–14]. A live cell's 3D MT network can now be visualized via super-resolution microscopy[15,16], yet it is currently impossible to replicate the observed arrangement *in vitro*. Therefore, it is impossible to decouple the effects of intracellular regulation from the role of cytoskeletal topological complexity in a parallel *in vitro* study.

Our approach directly addresses these concerns. First, we demonstrate how to manipulate individual MTs in 3D. Refractive microspheres cross-linked to MTs serve as 3D positioning nodes which can be held and moved independently with HOTs. Key advantages of holography[17] are scalability (hundreds of traps can be created and manipulated independently), 3D capability (traps can be defined anywhere within the accessible flow cell volume) and compatibility (often, HOT can be added to a system without modifying the pre-existing optical setup[18]). Prior related HOT-based techniques e.g.[19,20] served as an inspiration for our work but cannot be directly applied to MTs.

Department of Physics & Astronomy, Department of Biology, Center for Cell and Genome Science, University of Utah, 84112 Salt Lake City UT. Correspondence and requests for materials should be addressed to M.V. (email: vershinin@physics.utah.edu)

Second, we show how to scale up our technique to assemble fully 3D MT networks, including efficient methodologies for assembling, storing, and integrating network building blocks. Finally, we demonstrate how our technique can be utilized to model and direct molecular motor transport by assembling 3D MT-MT crossings with dynamic control over filament angle and separation: features important for cargo routing[16,21].

Results

In this work we manipulate MTs devoid of artificially induced chemical modifications, or MT-associated proteins, to retain maximum flexibility in modeling MT-based transport and biomechanics (chemical complexity can be introduced via a straightforward alteration of our assay). We orient individual MTs by tethering refractive microspheres (hereafter bead handles or BHs) along each filament (Fig. 1) which can then be manipulated in 3D via HOTs to construct complex 3D MT networks (Figs 2 and 3). Model cargos with enzymatically active motors (hereafter motorized cargos or MCs) and chemical factors regulating their activity may be incorporated to study transport on these networks (Figs 1 and 4). This strategy presents several challenges: (1) BHs need to have robust affinity for MTs so that adsorption onto MTs is efficient and stable; (2) BHs with many high affinity MT sites on their surfaces may serve to cluster MTs, so special care must be taken to ensure MTs can be manipulated individually. Below we describe how each challenge was addressed in detail.

(1) BH-MT affinity. Silica is our chosen BH material due to its high density (see below). We biotinylate the BHs' surface (Biotin-PEG-Silane) and then attach biotin-tris-NTA via a neutravidin bridge (Fig. 1b). Finally, we specifically attach a full-length enzymatically dead kinesin-1 mutant (E237A in hKIF5A) with a C-terminus HIS6 tag to confer BH-MT affinity (Fig. 1a–c). BH surfaces can be functionalized with various amounts of E237A kinesins to tune the robustness of BH-MT attachment.

(2) BH-MT clustering. BH and MT concentrations can be tuned to prevent BHs and MTs from forming unintended mesh-works (Supplementary Video 1) during mixing. Optionally, BHs and MTs can be co-incubated briefly on a nutator to facilitate occasional BH-MT association (Figs 1d and 2a). Long term separation between these components within the flow cell is achieved by using high density materials for BHs (e.g. silica). Upon admission into the flow cell, BHs sink while MTs float, thus quickly and reliably separating these otherwise coalescing species. Note: coverslip surface must be blocked well to prevent BH and MT coverslip adhesion (see Methods).

Ideally, a flow chamber will exhibit sparse MT coverage with about 2–3 BHs per field of view. As discussed above, it is often easiest to start network construction by capturing a BH pre-attached to a MT (Fig. 2a) in one HOT. A standalone BH may then be captured by an independent HOT and held near the MT at a desired displacement from the already attached BH (Fig. 2b). Firm attachment is quickly observed for BHs functionalized with high amounts of enzymatically dead kinesin. We refer to BH-MT-BH assemblies as "dumbbells" due to their shape. Dumbbells are tested for structural integrity and are then moved by repositioning one or both of the BHs with a HOT (Fig. 2c).

It is often desirable to ascertain that two BHs are connected by a single MT rather than a MT bundle, however doing so via direct imaging often proves difficult. A third "reporter" bead may then be attached to the dumbbell a few microns away from the BHs (Supplementary Fig. 1) and its diffusion can be analyzed (Supplementary Fig. 2) to evaluate the stiffness of the dumbbell's backbone, similar to previous approaches[22]. This technique is convenient enough in practice to be used *in situ* as a generic quality control step. Other optical trapping based techniques[23] are also compatible with our setup.

Our assay also allows mechanical properties of filament networks to be varied. For example, BH-MT linkage stiffness can be tuned by varying the number of motor cross-bridges and/or the nature of the cross-bridges (e.g. using shorter motor constructs). Alternatively, mechanical and chemical properties of MTs could be adjusted by varying tubulin polymerization conditions or adding MT-associated proteins[24]. Notably, mechanical properties of individual MTs can be easily pre-screened (Supplementary Fig. 1,2), so that mechanically heterogeneous networks can be easily designed and built with our approach.

To increase network construction efficiency, building blocks (free BHs, single beads with an attached MT, or whole dumbbells) can be captured and/or fabricated anywhere within the flow cell and then stockpiled in a designated location for subsequent use. An added benefit of silica beads is their propensity to remain relatively stationary upon settling to the surface. This allows all building blocks to be stored in designated areas. A sample stage equipped with absolute position gauge with micron-scale readout precision facilitates repeatedly accessing the stockpile location.

To study transport across complex 3D MT networks, MCs can be added to the assay buffer (Fig. 1a,c,d) prior to admission into the flow cell (here: silica beads with WT hKIF5A motors). Beads of significantly different diameters are used to distinguish MCs from BHs. MT polarity for each dumbbell is readily determined *in situ* by observing the motility direction of an MC driven by a known motor type, e.g. kinesin-1 (Fig. 2d–g).

To demonstrate basic dynamic network construction, we depict assembly of a 3D MT-MT intersection - the fundamental unit of network complexity. Two dumbbells are stretched taut. One MT (horizontal MT, Fig. 3a and Supplementary Video 2) is raised high enough to move over the perpendicular MT without forming inadvertent BH-MT attachments (Fig. 3b), since BHs bind MTs nearly instantaneously on contact. After MT-MT cross formation, filament separation and intersection angle can be freely adjusted (Fig. 3c,d). Z-axis positioning is easily calibrated (Supplementary Fig. 3,4) and positioning precision of 50 nm is reliably achieved. This is comparable to or better than the relevant *in vivo* length scale[16].

Our approach also allows us to cross-link MT filaments into stable 3D arrangements, i.e. self-supporting 3D networks. Figure 3e–l demonstrates this capability. A MT cross (Fig. 3g) is initially deformed into a dome shape by HOTs (Fig. 3i). Additional dumbbells are then used to cross-link the base of the dome structure (Fig. 3i, j), resulting in a dome that maintains its shape without HOT support (Fig. 3k,l). This geometry was chosen for demonstration purposes because it is visually simple, while displaying the key features: all MTs are substantially bent so the integrity of the structure is immediately apparent upon inspection and the shape has significant extent in all three dimensions (no single plane intersects all the beads in this network).

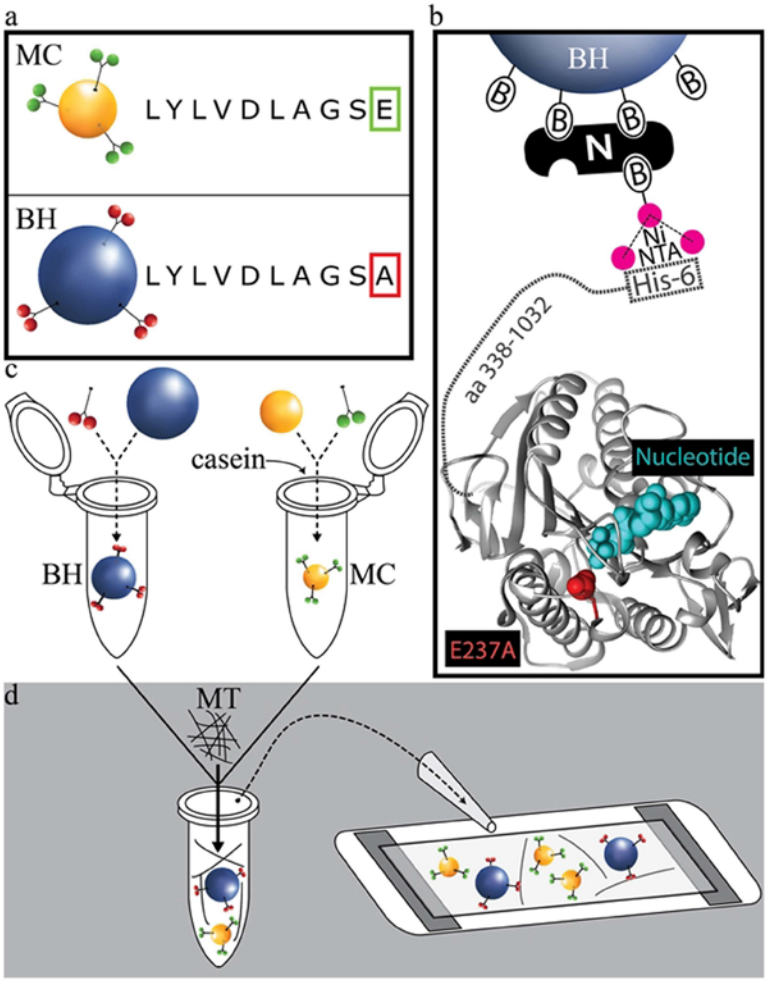

Figure 1. Basic BH-MT tethering strategy and preparation of assay constituents. (**a**) Motorized cargos are functionalized with WT hKIF5A while bead handles are functionalized with non-motile mutant hKIF5A (E237A). Construct sequences for kinesin-1 are otherwise identical, consisting of full length KHC and a HIS6 tag at the C-terminus. (**b**) BHs are specifically bound to E237A hKIF5A via a biotin-neutravidin-biotin sandwich (B-N-B in the figure) functionalized with a Nickel-activated tris-NTA molecule that binds with high affinity to the HIS6 tag on the E237A hKIF5A construct. Protein structure shows kinesin-1 motor domain. E237A mutation is highlighted in red and is in close proximity with a nucleotide (cyan). (**c**,**d**) BHs and MCs are prepared separately (see Methods), then combined together with MTs in assay buffer and finally are introduced into a flow chamber to allow filament network assembly.

The construction capabilities we show above are fully compatible with most established *in vitro* motility assay types (we also envision construction of 3D filament structures as a scaffolding for cell culture experiments). For example, kinesin-1 motors show robust motility when moving along a MT suspended above the surface (Supplementary Fig. 5a). More complex experiments, e.g. studies of kinesin inhibitors are also easy to implement. Kinesin motility can be partially inhibited, for example by the addition of ATP-γ-S (Supplementary Fig. 5b). The resultant magnitude of inhibition we observe is similar to what is expected from previous reports[25,26].

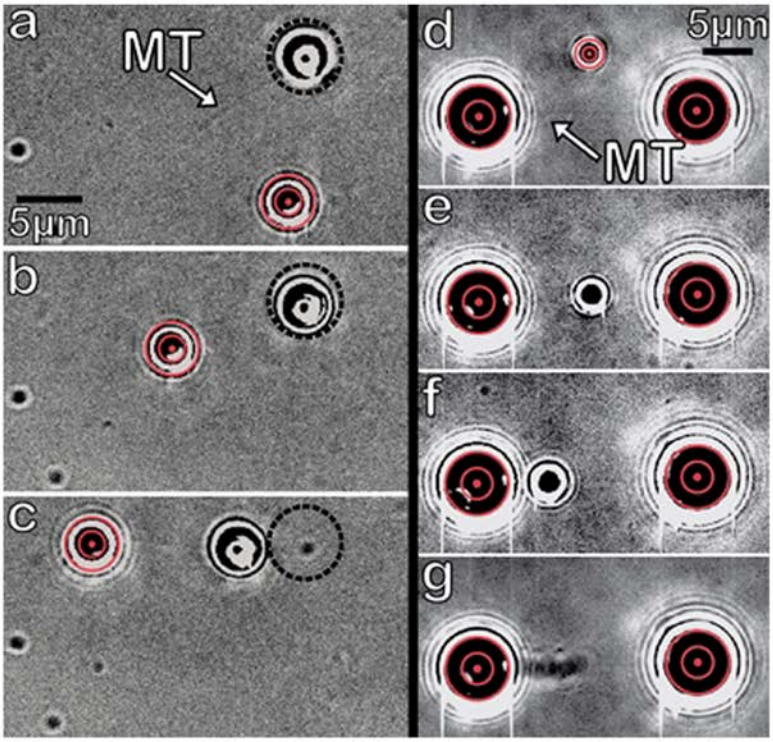

Figure 2. Dumbbell assembly and polarity characterization. (**a**) BH (highlighted by dotted black circle) starts out pre-attached to a MT and resting on the surface with second stand-alone BH close-by (red bulls-eye indicates it is being held in a HOT). (**b**) Trapped BH is maneuvered into close proximity to the "free" end of the MT. (**c**) MT attaches to trapped BH, and whole dumbbell assembly is moved by repositioning the HOT. Dotted black circle highlights original bead position. (**d**) A dumbbell is held taut by 2 HOTs, with a trapped MC nearby. (**e**) The MC is positioned to interact with the MT and is released upon binding. (**e–g**) The MC's displacement indicates the MT's polarity (here: plus end on the left). Movie frames corresponding to MC motion are averaged together to highlight that MC displacement is steady and continuous, rather than a result of detachment and reattachment.

In fact, our approach is advantageous over techniques using MT attachment to glass slides even for the simplest motility assays because cargos (artificial or *ex vivo*) can be positioned far away from the glass slide, eliminating concerns regarding non-specific cargo-glass interactions, or variations in biophysical or chemical parameters near the surface.

A model *in vitro* transport experiment (Fig. 4 and Supplementary Video 3) demonstrates the additional advantages of our approach to enable more complex motility experiments. An MC is maneuvered (via an independent HOT) to engage one of the MTs making up a pre-built 3D MT-MT intersection. The MC attaches to a MT far from the crossing site and proceeds through the intersection with a clearly observable tug of war event (Fig. 4a–f). Characterizing the forces involved in such low motor number tug-of-war events is straightforward in our suspended MT system by examining BH displacement in their respective HOTs (Supplementary Fig. 6); this is essentially impossible with prior techniques. In our system, we routinely observe teams of kinesin motors (on a single cargo) engaging in a tug of war when interacting with transverse MT filaments at an intersection. These events are common *in vivo* and play a significant role in cargo transport at MT intersections[21].

Such tug of war events affect cargo velocity and direction of motion, as well as the final outcome of the crossing events *in vitro*[9] (e.g. whether the cargo proceeds along the original MT or switches to the intersecting filament). The same dynamics is likely important *in vivo*[16]. Intracellular transport cannot be fully understood without first quantitatively studying cargo routing in a baseline environment free of confounding cellular regulatory factors[7]. Our ability to characterize forces associated with tug of war events in our system is therefore essential to accurately

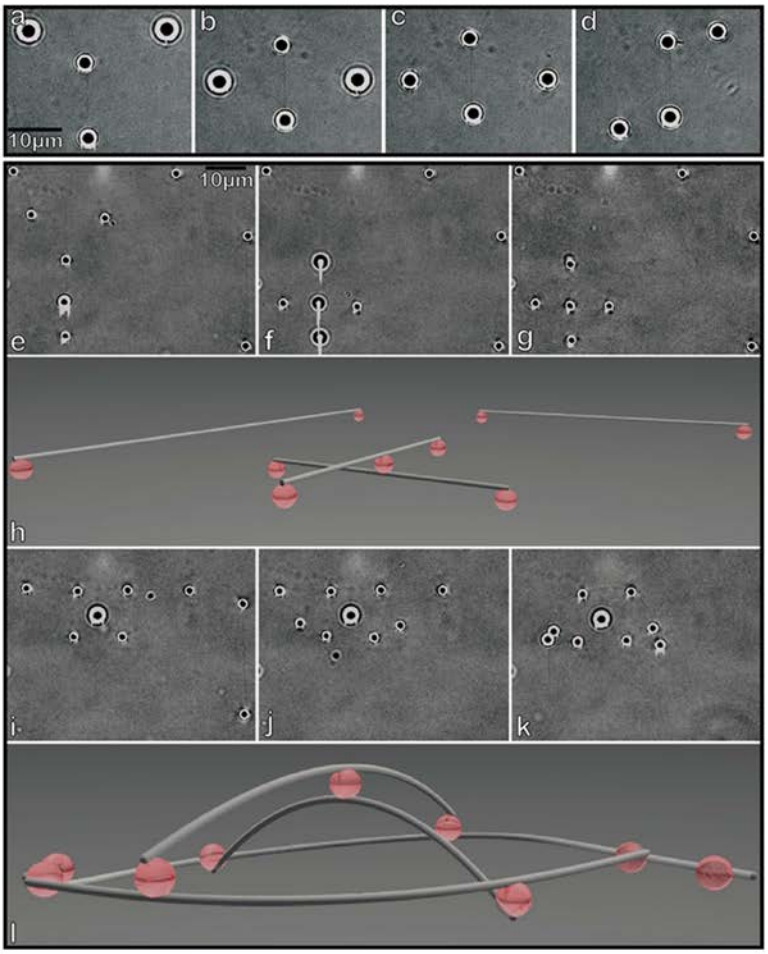

Figure 3. 3D network assemblies. Demonstration of dynamic control of a MT intersection **(a–d).** 2 dumbbells are situated perpendicular to one another with the horizontal dumbbell raised relative to the vertical dumbbell by approximately 5μm (**a**). The dumbbells are overlaid (**b**), then positioned at the same height (**c**), then reoriented to make a 45° angle (**d**), demonstrating the ability to adjust MT network geometry on demand. Assembly of a static 3D network (**e–l**). Four dumbbells are assembled, with one dumbbell featuring a BH attached in the middle (**e**). Two dumbbells are overlaid (**f**) and then bound together via the BH at the point of intersection (**g**). The 3D schematic of the resulting arrangement is shown in (**h**). The MT cross is reoriented and the outlying BHs are brought closer to the center until the central BH is displaced by ~3.5μm out of the base plane (**i**). The apparent diameter of the central bead is larger due to the bead being displaced from plane of focus. Additional dumbbells are then "wound" around the cross's peripheral BHs (**i,j**). The 3D assembly is then let go by the HOTs (**k**) and is able to maintain its own structure. 3D schematic for the final assembly is shown in (**l**).

model the general problem of cargo routing. A more detailed study is clearly desirable but is outside the scope of this work.

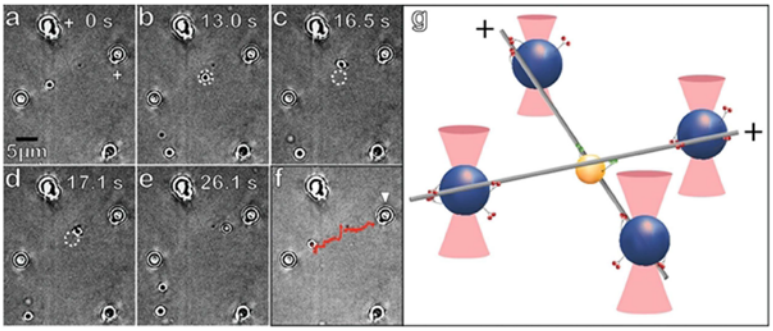

Figure 4. Technique validation for motility assays. (**a**) A MT crossing with 500 nm vertical filament separation is shown. An MC starts out progressing towards the intersection on the overlying MT. (**b**) MC reaches intersection and a tug of war ensues. The MC which is engaged on both MTs, starts to migrate up the transverse MT (**c**), but then after 0.6 seconds, disengages the transverse MT and snaps back (**d**) to once again solely translocate along the original MT (**e**). (**f**) Trace of the MC's progression (red) overlaid on the original frame of the sequence shown in (**a**). This event is representative for assays with MC-MT binding fraction slightly below saturation. White arrow in (**f**) indicates the BH whose position is tracked (Supplement Fig. 6). (**g**) Graphical model (not to scale) depicting the key aspects of the set-up in (**a**–**f**) and tug of war scenario in frame (**c**).

Discussion

Our technique has two key features which set it apart from existing approaches: 1) the ability to control individual filament positioning in 3D with high fidelity and 2) the ability to incorporate multiple filaments to create complex 3D MT networks. Our approach is not only useful for motility assays and biomechanics experiments but can also be used to "wire up" nanodevices for molecular motor based transport e.g. [3]. For example, some proposed biosensor designs[3] rely on molecular motors to transport targeted analytes throughout distinct microchip compartments in a bead assay configuration. This concept has been validated[3], but an inability to design definitive MT networks has hampered the technology's progress. Our method finally enables the construction of arbitrary MT networks to route cargo in a customized manner. Our approach can also be easily integrated with other experimental protocols, which for example, may allow investigations of the effects of MT-associated proteins on motor-driven transport in the context of complex 3D MT networks.

Holographic technology is limited by the rate at which trap positions can be updated. This precludes using the HOT technology for experiments such as probing elastic moduli of networks over a wide frequency range[27], or as force clamps[28]. This shortcoming has been overcome in our system by adding a conventional trap with fast repositioning capability to the optical train[18], but at the expense of increased setup complexity.

Another limitation of our system is that construction of structures takes many minutes. Therefore, once constructed, a given network is likely to be reused for many experiments (e.g. motility assays). This allows experiments to be performed in a nearly identical environment which is usually advantageous for experimental design but also places a premium on the ability to visualize MTs without relying on fluorophores that photobleach quickly under intense illumination for a long duration. In addition, since MTs are likely to be arranged without alignment along one direction, we found conventional DIC imaging to be suboptimal for visualization. We have found that direct brightfield illumination imaging[29] works best but our technique would benefit from extremely photostable labeling which could be demonstrated to not affect MT-based transport and elastic properties of the filaments. We stress that better visualization could help speed up the workflow and help scale the system toward more complexity, but this is not currently a critical limitation.

As we show above, our method is also well suited to create interconnected 3D MT geometries to construct shapes and engineering components. Mechanical properties of the filament building blocks can be altered by varying the number of motor cross-bridges, and/or the nature of the cross-bridges (e.g. using shorter motor constructs.) Mechanical properties of individual dumbbells can also be varied within the same assay[24] and can then be easily pre-screened (Supplementary Fig. 1,2) prior to assembly, so that mechanically heterogeneous networks can be easily designed and built with our approach.

Our approach is highly scalable. A typical volume accessible in a single field of view is far larger than typical cellular volume. This potentially allows intracellular MT networks to be replicated *in vitro*, even allowing substantial homothetic magnification. Modern HOT control software (including our setup) allows for 100–200 traps to be simultaneously created and controlled, which is sufficient to construct many MT networks of biological and technological interest. Of course, it is already conceivable that this number of traps will present a limitation if highly complex networks become desirable. In addition, for high number of traps, network visualization will become increasingly difficult and it is likely that highly complex filament structures, such as micron-scale scaffolding or mechanical metamaterials, will require extensions of the technique to permit automated assembly.

In summary, due to its high precision and extreme scalability, our approach enables a wide range of experiments, from single molecule assays to large scale construction of rigid filament scaffolding or cellular scale transport networks. Similarly, many previously inaccessible biomimetic engineering designs become feasible with our system.

Methods

BH preparation. Monodisperse 2 μm silica beads 1% (w/v) (Microspheres-Nanospheres, Cold Spring, NY) were diluted by 20x in EtOH and were reacted with Biotin-PEG-Silane (MW 3400, Laysan Bio, Arab, AL). Biotin-PEG-Silane was added to a final concentration of 11.75 mg/ml per manufacturer recommendation. This amount of Biotin-PEG-Silane ensured we had at least 100X molar excess relative to reactive sites on the 2 μm silica beads (assuming 4.9 OH groups / nm^2 for silica beads[30]). The beads were allowed to react for 1 hour at room temperature, then were washed 3 times in ultrapure water and were re-suspended in ultrapure water to maintain a 1% (w/v) bead concentration.

These biotinylated beads are incubated with an equal volume of 10 mg/ml of neutravidin (Thermo Fisher Scientific, Waltham, MA). The high molar ratio of neutravidin:surface biotin groups (~10:1) ensures that biotin groups are saturated with neutravidin. For daily use, an aliquot of the neutravidin-biotin-silica beads is incubated with 0.1 mg/ml of biotin-tris-NTA, a trivalent NTA derivative crosslinker (Biotechrabbit, Hennigsdorf, Germany) for 15 minutes. Assuming that each neutravidin has three available binding sites after being attached to the bead surface via a biotin ligand, the molar ratio of biotin-tris-NTA : neutravidin sites was at least 10:1. These beads, referred to hereafter as tris-NTA beads, are then activated with a 3X molar amount of $NiCl_2$ or other metal salt such as $CoCl_2$. After a 5 minute incubation, the Ni-NTA beads are diluted 7.5x in BH buffer (35 mM PIPES, 5 mM MgSO4 pH 7.2, supplanted with 1 mM GTP, 2.67 mM ATP, and optionally 40 μM Taxol.) Immotile E237A hKIF5A (full length HC construct, C-terminal HIS6 tag) is then added to a desired concentration (50–70 nM typically), and incubated for 30 minutes. Tris-NTA to HIS6 binding is reversible via the addition of various metal chelators or imidazole[31], which is useful for control experiments.

In summary, our strategy is to saturate previously created surface functionalizing binding sites at every step, and then use as little E237A hKIF5A as functionally necessary (a generally applicable consideration, considering that E237A hKIF5A is effectively a custom made reagent). Our kinesin to glass surface attachment strategy is similar to the one described by the Surrey lab[32].

Motorized Cargo Preparation. Monodisperse 1 μm silica beads 1% (w/v) (Microspheres-Nanospheres, Cold Spring, NY) are diluted 20x in MC buffer (35 mM PIPES, 5 mM MgSO4 pH 7.2, supplanted with 5mM ATP, 5 mM DTT). The use of silica for MCs ensures that the model cargo will have a preferred downward orientation when attached to a MT. Bead materials with density matched to our buffer result in more diffusive MC motion. The desired concentration of wild-type hKIF5A (full length HC construct, C-terminal HIS6 tag) are then added to the motorized cargo buffer, and incubated for 30 minutes. Casein (40 mg/mL stock; 100X final dilution; MP Biomedicals) is added with the motors to block the surface and reduce clumping.

Assay Buffer Preparation. Due to surface passivation, adding components sequentially will displace materials administered prior. Therefore, BHs and MTs are combined and incubated for 2 minutes. Thereafter MCs are added to the solution. The volume ratio of BH:MC:MT components is 85:10:5. The resulting mix is then quickly admitted into the flow cell.

Coverslip Silanization. #1.5 Borosilicate coverslips (VWR, Radnor, PA) are subjected to a chemical etch in Piranha solution for 1 hr. Coverslips are then washed 3 times in ultrapure water and then are dried in an oven for 1 hour at 100 degrees. The coverslips are then incubated in a beaker containing 10% Hexamethyldisilazane (HMDS) (Gelest, Morrisville, PA) solution in toluene for at least 1 hour (overnight is better). These HMDS-treated coverslips are then washed 3 times in EtOH, once in ultrapure water and are then cured in the oven at 100 degrees for 1 hour.

Flow Chamber Preparation. A flow chamber is constructed by attaching an HMDS-treated coverslip to a coverslide via parallel strips of double-sided tape (3 M, Saint Paul, MN). 1 flow chamber volume of 10% pluronic F-127 (Sigma-Aldrich, St. Louis, MO) in ultrapure water is admitted and allowed to incubate for 15 minutes. Then 2 flow chamber volumes of casein (40 mg/ml in PMEE) is administered and allowed to sit for 15 minutes.

Our approach is similar to the one described previously[33] however we find that additional blocking with casein improves surface blocking performance. Many similar techniques have been developed e.g. [33,34]. They are likely to provide similar or better performance. However, casein blocking alone, even using κ-casein isoform exclusively, does not provide acceptable blocking for our assays.

Optics and imaging. Imaging was performed using a Nikon Eclipse-Ti microscope equipped with a high-magnification, high-NA objective (Nikon Plan Apo VC 100 oil, 1.40 NA). A high-resolution camera (iXON DU897; Andor Technology USA) and Nikon NIS elements AR software (Nikon Instruments USA, Melville, NY) were used to record experiments. Typical field of view size for this work was ~55 μm × 55 μm.

The holographic optical trap system was set up as previously described[18]. Briefly, a spatial light modulator (Boulder Nonlinear Systems, Lafayette, CO) was installed in an optical plane conjugate to the back focal plane of the objective. BioRyx software (Haemonetics, Braintree, MA) was used to define and control holographic trap arrangement.

Microtubule Preparation. Porcine tubulin (Cytoskeleton, Denver, CO) was polymerized according to the manufacturer's protocol to produce MTs with a tubulin concentration of 140 μM. All MTs used in this work were

taxol-stabilized. Polymerized MTs are then diluted 100x in MT buffer (35 mM PIPES, 5 mM MgSO4 pH 7.2, supplanted with 1 mM GTP, and 40 μM Taxol.)

Kinesin Purification. hKIF5A KHC dimers (wildtype sequence with HIS6 tag on C-terminus) were expressed in an E. coli system as previously described[35]. Briefly, full length KHC with N-terminus MBP solubility tag was expressed and purified. The MBP tag was then proteolytically cleaved as a final purification step.

References

1. Hess, H. & Vogel, V. Molecular shuttles based on motor proteins: active transport in synthetic environments. *J. Biotechnol.* **82,** 67–85 (2001).
2. Muthukrishnan, G., Hutchins, B. M., Williams, M. E. & Hancock, W. O. Transport of semiconductor nanocrystals by kinesin molecular motors. *Small* **2,** 626–630 (2006).
3. Carroll-Portillo, A., Bachand, M., Greene, A. C. & Bachand, G. D. *In vitro* Capture, Transport, and Detection of Protein Analytes Using Kinesin-Based Nanoharvesters. *Small* **5,** 1835–1840 (2009).
4. Aoyama, S., Shimoike, M. & Hiratsuka, Y. Self-organized optical device driven by motor proteins. *Proc. Natl. Acad. Sci. USA.* **110,** 16408–16413 (2013).
5. Roos, W. H. *et al.* Dynamic kinesin-1 clustering on microtubules due to mutually attractive interactions. *Phys. Biol.* **5,** 046004 (2008).
6. Tarhan, M. C., Orazov, Y., Yokokawa, R., Karsten, S. L. & Fujita, H. Suspended microtubules demonstrate high sensitivity and low experimental variability in kinesin bead assay. *The Analyst* **138,** 1653–1656 (2013).
7. Vale, R. D. The role of reconstitution in cytoskeleton research. *Methods Enzymol.* **540,** xix–xxiii (2014).
8. Huber, F. *et al.* Emergent complexity of the cytoskeleton: from single filaments to tissue. *Adv. Phys.* **62,** 1–112 (2013).
9. Ross, J. L., Ali, M. Y. & Warshaw, D. M. Cargo transport: molecular motors navigate a complex cytoskeleton. *Curr. Opin. Cell Biol.* **20,** 41–47 (2008).
10. Dupont, A. *et al.* Single Particle Tracking in Living Cells: Is the Third Dimension Worth It? *Biophys. J.* **104,** 650a (2013).
11. Liu, S.-L. *et al.* Three-Dimensional Tracking of Rab5- and Rab7-Associated Infection Process of Influenza Virus. *Small* **10,** 4746–4753 (2014).
12. Liu, S.-L. *et al.* Fast and High-Accuracy Localization for Three-Dimensional Single-Particle Tracking. *Sci. Rep.* **3** (2013).
13. Katayama, Y. *et al.* Real-time Nanomicroscopy via Three-Dimensional Single-Particle Tracking. *Chemphyschem Eur. J. Chem. Phys. Phys. Chem.* **10,** 2458–2464 (2009).
14. Toprak, E., Balci, H., Blehm, B. H. & Selvin, P. R. Three-Dimensional Particle Tracking via Bifocal Imaging. *Nano Lett.* **7,** 2043–2045 (2007).
15. Huang, B., Wang, W., Bates, M. & Zhuang, X. Three-Dimensional Super-Resolution Imaging by Stochastic Optical Reconstruction Microscopy. *Science* **319,** 810–813 (2008).
16. Bálint, Š., Vilanova, I. V., Álvarez, Á. S. & Lakadamyali, M. Correlative live-cell and superresolution microscopy reveals cargo transport dynamics at microtubule intersections. *Proc. Natl. Acad. Sci.* **110,** 3375–3380 (2013).
17. Grier, D. G. & Roichman, Y. Holographic optical trapping. *Appl. Opt.* **45,** 880–887 (2006).
18. Butterfield, J., Hong, W., Mershon, L. & Vershinin, M. Construction of a high resolution microscope with conventional and holographic optical trapping capabilities. *J. Vis. Exp. JoVE* (2013). doi: 10.3791/50481
19. Plewa, J., Tanner, E., Mueth, D. & Grier, D. Processing carbon nanotubes with holographic optical tweezers. *Opt. Express* **12,** 1978–1981 (2004).
20. Agarwal, R. *et al.* Manipulation and assembly of nanowires with holographic optical traps. *Opt. Express* **13,** 8906 (2005).
21. Osunbayo, O. *et al.* Cargo Transport at Microtubule Crossings: Evidence for Prolonged Tug-of-War between Kinesin Motors. *Biophys. J.* **108,** 1480–1483 (2015).
22. Pampaloni, F. *et al.* Thermal fluctuations of grafted microtubules provide evidence of a length-dependent persistence length. *Proc. Natl. Acad. Sci. USA.* **103,** 10248–10253 (2006).
23. van Mameren, J., Vermeulen, K. C., Gittes, F. & Schmidt, C. F. Leveraging Single Protein Polymers To Measure Flexural Rigidity†. *J. Phys. Chem. B* **113,** 3837–3844 (2009).
24. Hawkins, T., Mirigian, M., Selcuk Yasar, M. & Ross, J. L. Mechanics of microtubules. *J. Biomech.* **43,** 23–30 (2010).
25. Schliwa, M., Shimizu, T., Vale, R. D. & Euteneuer, U. Nucleotide specificities of anterograde and retrograde organelle transport in Reticulomyxa are indistinguishable. *J. Cell Biol.* **112,** 1199–1203 (1991).
26. Cohn, S. A., Ingold, A. L. & Scholey, J. M. Quantitative analysis of sea urchin egg kinesin-driven microtubule motility. *J. Biol. Chem.* **264,** 4290–4297 (1989).
27. Mizuno, D., Head, D. A., MacKintosh, F. C. & Schmidt, C. F. Active and Passive Microrheology in Equilibrium and Nonequilibrium Systems. *Macromolecules* **41,** 7194–7202 (2008).
28. Lang, M. J., Asbury, C. L., Shaevitz, J. W. & Block, S. M. An Automated Two-Dimensional Optical Force Clamp for Single Molecule Studies. *Biophys. J.* **83,** 491–501 (2002).
29. Gutiérrez-Medina, B. & Block, S. M. Visualizing individual microtubules by bright field microscopy. *Am. J. Phys.* **78,** 1152–1159 (2010).
30. Zhuravlev, L. T. The surface chemistry of amorphous silica. Zhuravlev model. *Colloids Surf. Physicochem. Eng. Asp.* **173,** 1–38 (2000).
31. Huang, Z., Hwang, P., Watson, D. S., Cao, L. & Szoka, F. C. Tris-Nitrilotriacetic Acids of Sub-nanomolar Affinity Toward Hexahistidine Tagged Molecules. *Bioconjug. Chem.* **20,** 1667–1672 (2009).
32. *Microtubules, in vitro*, Volume 115, Second Edition. (Academic Press, 2013).
33. Dixit, R. & Ross, J. L. Studying plus-end tracking at single molecule resolution using TIRF microscopy. *Methods Cell Biol.* **95,** 543–554 (2010).
34. Ionov, L., Synytska, A., Kaul, E. & Diez, S. Protein-Resistant Polymer Coatings Based on Surface-Adsorbed Poly(aminoethyl methacrylate)/Poly(ethylene glycol) Copolymers. *Biomacromolecules* **11,** 233–237 (2010).
35. Smith, T. E. *et al.* Single-molecule inhibition of human kinesin by adociasulfate-13 and -14 from the sponge Cladocroce aculeata. *Proc. Natl. Acad. Sci. USA.* **110,** 18880–18885 (2013).

Acknowledgements

The authors gratefully acknowledge helpful discussions with Dr. Steven Gross and Dr. Saveez Saffarian for helpful discussions. The authors also acknowledge Leslie Mershon for help with experiments and Alyssa Jorgensen for help with figure artwork. Focused ion beam etching made use of University of Utah USTAR shared facilities supported, in part, by the MRSEC Program of the NSF under Award No. DMR-1121252.

Author Contributions

M.V. initiated and guided the project. J.B. and O.O. performed experiments and refined the conceptual implementation. J.B., O.O. and M.V. wrote the manuscript.

Additional Information

Supplementary information accompanies this paper at http://www.nature.com/srep

Competing financial interests: The authors declare no competing financial interests.

How to cite this article: Bergman, J. *et al.* Constructing 3D microtubule networks using holographic optical trapping. *Sci. Rep.* **5**, 18085; doi: 10.1038/srep18085 (2015).

Supplementary Information for

Constructing 3D microtubule networks using holographic optical trapping

J. Bergman, O. Osunbayo, M. Vershinin*

Department of Physics & Astronomy,
Department of Biology,
Center for Cell and Genome Science,
University of Utah,
Salt Lake City UT 84112

**e-mail address: vershinin@physics.utah.edu*

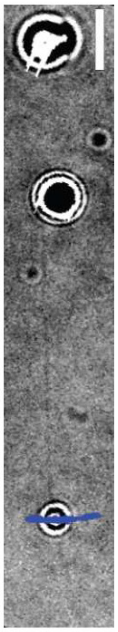

Supplementary Figure 1: MT stiffness assay. MTs were held in the imaging plane via two BHs spaced several microns apart and held in holographic optical traps at maximum displacement to assure no slack in the MT. The free end of the MT was then allowed to move under the influence of Brownian fluctuations. A BH acting as fiduciary marker was then placed on the MT to report MT displacements. Bead displacements were predominantly in the transverse direction (blue). Scale bar: 10 µm.

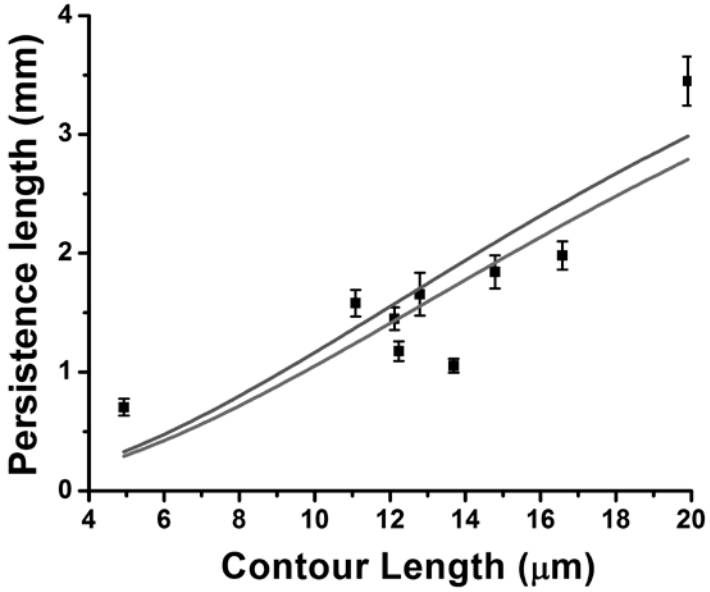

Supplementary Figure 2: MT stiffness analysis. The data acquired as shown in Supplement Figure 1 was analyzed similar to Pampaloni et al. (ref. 20, main text). Though MT lengths in our experiments were not sufficient to accurately estimate saturation level for persistence length of MTs, our data fits well to eqn. 4 in Pampaloni et al. if this parameter value is set at 6.3 mm (red curve). The cross-over length for our data (22.4 ± 1.3 μm) is close to the previously reported fit (green curve).

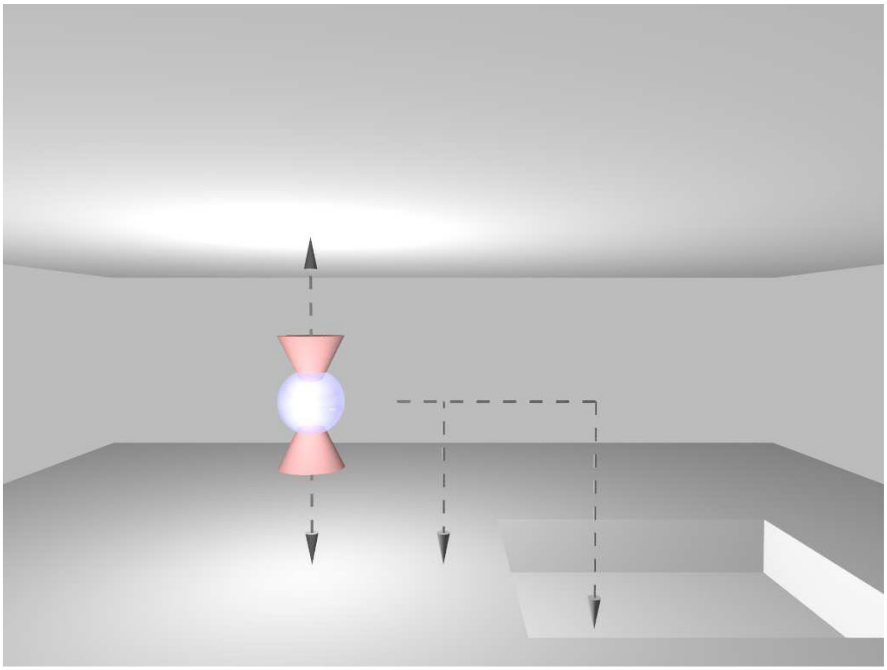

Supplementary Figure 3: Z-axis calibration. Unlike X and Y bead displacements (i.e. movement along axes orthogonal to the microscope axis), the Z-axis displacement cannot be estimated directly from video record. To calibrate Z-axis positioning, we have raised and lowered a NIST traceable silica bead (Microspheres-Nanospheres, Cold Spring, NY) in a holographic optical trap until the bead touched the bounding surface of the flow cell. In one method, the bead was limited by the upper and lower flow cell walls separated by a known distance (left dashed lines and arrows). 10µm polystyrene beads (CV=5%) (Polysciences, Warrington, PA) were typically used as spacers though other spacers (e.g. 5 µm thick double sided tape 68556, TESA, Charlotte, NC) produced nearly identical calibration values. We calibrated the HOT software Z-axis positioning units (i.e. voxel height) by dividing the bead probe's range of motion by the corresponding number of voxels. In another method, we have used focused ion beam to etch a flat bottom trench or a staircase (supplementary figure 4) into a coverslip. Etched trench depths were measured with an atomic force microscope and used as reference distance for voxel height calibration (right dashed lines and arrows). With either approach, when the focal plane of the objective coincided with the bottom plane of the flow cell our voxel height was 131 ± 2 nm (100X NA oil objective). The calibrations for other focal planes of the objective were within 10% of this value.

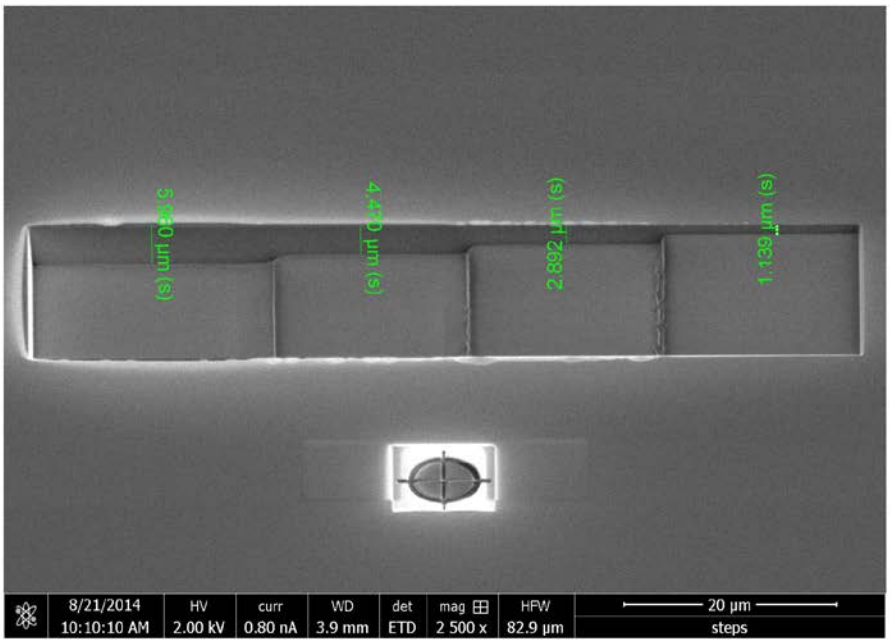

Supplementary Figure 4. Example of 3D coverslip steps used to calibrate voxel height. Focused ion beam etching was used to create step structures which could then be used for Z-axis calibration (Supplement Fig. 3). Steps of ~1µm height were typically used.

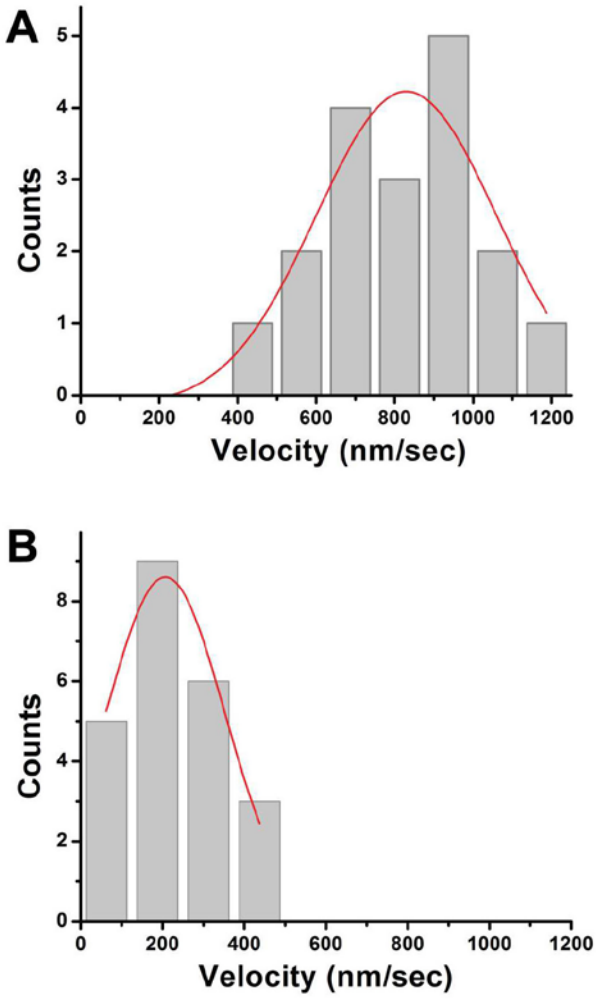

Supplementary Figure 5. Motility assays on suspended MTs. Healthy motor velocities (814±45 nm/sec; n=18; mean±SEM) are seen for kinesin-1 driven MCs (A). However, adding ATPγS inhibitor (ATP: ATPγS molar ratio 2.25:1) reduces the velocities significantly (233±117 nm/sec; n=23; mean±SEM); t-test $p<10^{-13}$.

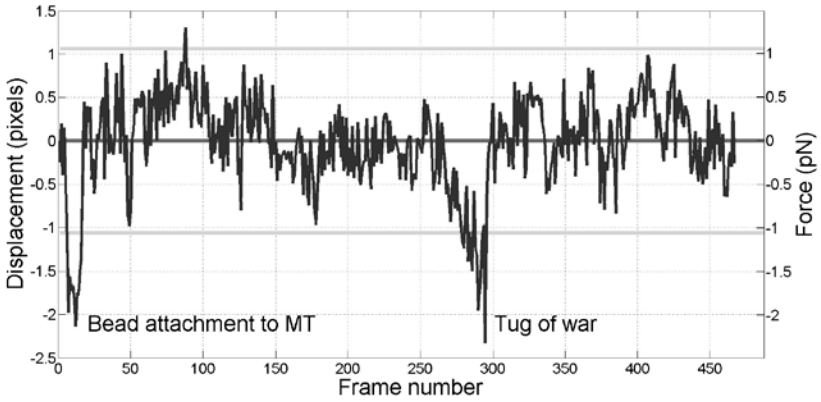

Supplementary Figure 6. BH tracking and force readout. Tracking of the position of the upper right BH in Fig. 4 and Supplementary Video 2 (bead is highlighted by arrow in Fig. 4f). The bead generally shows limited diffusion around its median bead position (red line) and instantaneous bead position is typically within 2 standard deviations of the median (green lines). However two sustained deviation outside of these limits are observed. First occurs when an MC is placed on the MT connected to the BH being tracked. The force is exerted on the BH because the MC is initially moved by the HOT resulting in a perturbation when the MC engages on the MT. The second event occurs during MC navigation at the intersection and provides direct readout of the tug of war forces involved in the process. Here the maximum pulling force of 1.4 pN is observed (107 nm/px imaging; 0.95 pN/100 nm optical trap stiffness).

Supplementary Video 1: MT asters on BHs can be induced via prolonged BH co-incubation on a nutator with an excess of MTs. Such asters are easy to discern during an experiment. The video is included for contrast with the controlled assembly we achieve when prolonged co-incubation is avoided.

Supplementary Video 2: Assembly and dynamic adjustment of MT cross arrangement shown in Fig. 3.

Supplementary Video 3: Kinesin-1 driven bead traverses a MT crossing as shown in Fig. 4.

Supplement Text 1: As discussed in the main text, it may be desirable to ascertain that dumbbells consist of two beads connected by a singular MT rather than a MT bundle. In practice, a typical dumbbell we construct is >10 μm in length. Most MTs we and others produce via polymerization under normal conditions are much shorter than this [1]. Therefore the probability of two extremely long MTs being aligned between two beads is very low. A greater concern is that it is difficult to see if shorter MTs are present near a long MT which is linking the dumbbell together. Shorter MTs will not cross-link the dumbbell but may interfere with 3D structural assembly or motility experiments. To test for these unwanted conditions, a third bead may be placed on the dumbbell as shown in Supplement Figure 1. One can then track the displacement of the marker bead (lowest bead in Supplement Figure 1) while holding the other two beads trapped. With this data, one may then conduct MT flexural rigidity analysis as shown in Supplement Figure 2 and evaluate the hypothesis that the persistence length of the dumbbell is on par with a single MT, or a bundle of MTs.

Note that most of the persistence lengths in Supplement Figure 2 are for contour lengths between 11 and 17 μm and the standard deviation for this data is ~0.33 mm (if one subtracts the fitted trend then the standard deviation becomes ~0.32 mm so that our estimate of overall noise is not notably skewed by the slope in the trend). If two MTs were connecting the dumbbell (and therefore if two MTs were diffusing together as one unit) then the second moment of MT cross-section would at least double (greater increase is likely depending on the relative geometric arrangement of the two MTs) leading to a commensurate increase in the observed persistence length. The data uncertainty is likely to add in quadrature leading to a standard deviation estimate of ~0.47 mm. Therefore, we propose discarding all dumbbells (for this range of contour lengths) with persistence length above 2*6.3*(1+(22.4/L)^2)-2*0.47 where L is contour length. In other words, we propose discarding all dumbbells whose persistence lengths are higher than or within two standard deviations of double the fitted trend. More data for the very longest dumbbells will be needed to establish that this criterion works in those cases. However in practice, all dumbbells we have tested to date have passed such a test. As expected, the probability of doubling up of MTs for dumbbells above 10 μm in length is a very unlikely possibility and this likelihood will only decrease as the dumbbell length increases (due to a decrease in number of very long MTs). Thus, such occurrences appear to be of negligible likelihood for the longest dumbbells (>20 μm) and may not be worth explicit testing.

Another consideration yields similar conclusions, though less directly. If we assume that doubling up of MTs in a dumbbell occurs randomly, then half of such dumbbells would be cross-linked by oppositely oriented MTs. In that case, kinesins on MCs would be free to engage on both MTs and such engagements would produce observable tug of war events [2]. Therefore, the healthy unidirectional MC motion routinely observed in our work further argues that dumbbells crosslinked by two or more MTs are negligibly rare.

Supplement Text 2: The development of this technique took several years and was interrupted several times due to technical difficulties. We discuss some of these difficulties below in hopes it will help other implementations of our approach. By far the biggest problem for us was our strict requirement that MTs must remain unmodified except where BHs bind to them. For example, we avoided using biotinylated MTs because we could not envision a way to ascertain that the MT-bound biotins would not interfere with the binding of any MT-associated protein under any conditions or that they would not affect any MT mechanical properties. This put a premium on finding a good agent to put on BHs to serve as "glue". Our trials of a vast number of antibodies have all been fruitless. All antibodies we tested would "slide" along MTs under applied load. Incubating beads with extremely high amounts of antibodies would result in bead clumping. Similarly many MAPs may slide along MTs under applied load and cannot be relied upon to provide a robust fixed attachment point between a bead and a MT, consistent with recent reports [3].

In addition, we desired a "glue" which would allow for nearly instantaneous binding as soon as bead and MT were brought near each other because any significant delay could affect structure assembly rate and binding reliability especially for larger structures. Therefore, our requirements placed a premium on molecular solutions where the binding site was flexibly attached to the tag which we could use to functionalize our BHs. The recombinant expression of enzymatically dead kinesin-1 HC dimers fulfilled all our requirements, although efficient expression of full length kinesins without aggregation initially proved very challenging.

The problem of separating BHs and MTs to prevent aster formation was comparatively easier. We started with polystyrene bead BHs and used extremely high bead and MT dilutions so that it often took us minutes of searching across the flow cell to find any MTs and beads. At such low dilutions, simplest structural assemblies were possible so the proof of principle was obtained early. However, extremely low dilutions and extremely long searches were not practical and moreover polystyrene beads were hard to store for later use because they diffused too readily. We therefore switched to silica beads which readily sunk to the bottom. However, casein-blocked surfaces were not blocked well-enough and beads would bind to the surface after some time. We therefore developed better surface passivation techniques which solved our issues with the storage of prebuilt components for later assembly. Through routine use of such assays we discovered that silica beads sunk fast enough that they could be mixed with MTs for a short time, then admitted into glass slides and they would efficiently spatially segregate from the MTs if MTs were at a low enough concentration as described in the main text. This finally made all the pieces we needed readily available for fast and efficient workflow.

The final challenge for us was finding a way to reliably attach enzymatically dead motors to beads. This is essential because if the attachment is not robust then such dead motors may detach from BHs and reattach along MTs. This was observed early on and efforts were made to improve bead to motor attachments.

As the technique stands today, many MT crosses and similar simple 3D structure can be assembled and used in one day by one operator. The typical assembly time for such simple structures is a few minutes

for a trained experimentalist. The workflow is convenient and practical, especially since many experimental designs allow complex 3D structures to be subjected to many repeated experiments.

References Cited:

1. Lin, Y.-C., Koenderink, G. H., MacKintosh, F. C. & Weitz, D. A. Viscoelastic Properties of Microtubule Networks. *Macromolecules* **40,** 7714–7720 (2007).
2. Osunbayo, O. *et al.* Cargo Transport at Microtubule Crossings: Evidence for Prolonged Tug-of-War between Kinesin Motors. *Biophys. J.* **108,** 1480–1483 (2015).
3. Hinrichs, M. H. *et al.* Tau Protein Diffuses along the Microtubule Lattice. *J. Biol. Chem.* **287,** 38559–38568 (2012).

CHAPTER 3

ARTIFICIAL MICROTUBULE CYTOSKELETON CONSTRUCTION, MANIPULATION, AND MODELING VIA HOLOGRAPHIC OPTICAL TRAPPING

Reprinted from Bergman, J., Doval, F., Vershinin, M. Artificial microtubule cytoskeleton construction, manipulation, and modeling via holographic trapping of network nodes. Proc. of SPIE Vol. 9930, 993005 (2015). With permission from SPIE.

Invited Paper

Artificial microtubule cytoskeleton construction, manipulation, and modeling via holographic trapping of network nodes

J. Bergman, F. Doval, M. Vershinin

Department of Physics & Astronomy, University of Utah

ABSTRACT

Cytoskeletal networks are 3D arrangements of filaments whose complex spatial structure contributes significantly to their intracellular functions, e.g. biomechanics and cargo motility. Microtubule networks in cells are a particular challenge for *in vitro* modeling because they are sparse and possess overall structure and so cannot be approximated experimentally as a random hydrogel. We have used holographic optical trapping to precisely position and hold multiple microtubule filaments in an *in vitro* assay, where chemical and environmental variables can be carefully controlled. Below we describe the relevant practical details of the approach and demonstrate how our approach can scale to accommodate modeling of molecular motor transport and biomechanics experiments.

KEYWORDS: biophysics, cytoskeleton, 3D, holographic optical trapping, microtubules, transport, biomechanics

INTRODUCTION: Traditional biology, in other words the art of reverse engineering living matter, increasingly relies upon atomic- and molecular-scale forward engineering techniques to enable and accelerate progress. Biological systems provide a seemingly endless stream of examples of practical working nanotechnology (1) but it often takes rebuilding this technology from the ground up to understand how it really works. Despite many recent developments, a quantitative description of biology extending from atomic to organismal level remains elusive, and engineering systems which rival or exceed organismal complexity from the bottom up is not practical.

For decades, nanotechnology has been borderline science fiction. Now that it has arrived, a new challenge has come to the fore: how to scale up. In the field of biology, deciphering how an individual nano-machine (for example a cytoskeletal motor) works is not the end of the road but merely the beginning. But to move forward, we need to deal with the sheer complexity of biological systems without sacrificing the control and precision achievable at the single molecule level. Understanding how living matter functions across multiple length scales, time scales, and complexity scale is a challenge whose scope and importance grows every year (2). For example, the eukaryotic cytoskeleton as a whole is merely a collection of motors, cargos, filaments, and some associated chemicals but how these elements all integrate together to yield functional intracellular logistics and organization remains unclear.

Further progress can and must be accelerated by developing techniques to experimentally and theoretically address biological complexity. The challenge is to set up biologically relevant assays with high complexity and still reproducibly probe how the system changes when just one component is altered or removed. Consider again the cytoskeleton, and even more specifically the cytosolic actin and microtubule filaments (AF and MT respectively) which support active transport. Biology, of course, presents us with a great variety of cytoskeletal arrangements so it is often desirable to restrict consideration to some specific cytoskeleton archetype, e.g. to G_0 state of some non-polar animal cell. One may then plausibly reduce the picture to a textbook scheme(3), whereby MTs form a nearly radial array anchored at the MT organizing center (MTOC) and AFs form a more random hydrogel with some statistical preference for angles between filaments interspersed with actin bundles. In this picture, AFs are far more numerous and dense than MTs and are more prevalent towards the cell periphery. So, we would ideally want an experimental capability to build an *in vitro* model which faithfully reproduces intracellular MT cytoskeleton with a well-defined organizing center. Associated proteins and cargos could then be added under controlled conditions to study the true dynamics of the subsystem. And furthermore, ideally one would then want to be able to move or remove one filament, or one associated protein, or one cargo and rerun the experiments under otherwise identical conditions to see the effect of small perturbations on the complex ensemble. After all, if we desire a quantitative description of biology then by implication we desire to do away with the notion of a phenotype and instead to be able to capture and analyze very small (nearly differential) changes.

Biosensing and Nanomedicine IX, edited by Hooman Mohseni, Massoud H. Agahi, Manijeh Razeghi,
Proc. of SPIE Vol. 9930, 993005 · © 2016 SPIE · CCC code: 0277-786X/16/$18 · doi: 10.1117/12.2237231

The above vision is still not achievable with today's technology so let's reduce complexity further. Let's neglect the fact that AFs and MTs are typically inter-independent on each other in cells and most of the regulation of cytoskeletal dynamics. Suddenly we are dealing with two independent sub-systems which can be modeled individually. It is quite informative to compare the types of questions we need to answer for these two subsystems and the type of complexity which arises in each case. Below, we will specifically focus on two major roles of the AF and MT cytoskeleton: both are venues for intracellular transport and both serve an important role in cell biomechanics.

For either filament network we are in general faced with the need to model 3D geometric complexity (or if we are thinking of the filaments as forming a network then one might also consider the topological complexity of this network). However the nature of this complexity is different in each case. For example, AFs in lamellipodia are typically shorter (length distribution on the order of a few microns), quite dense and cross-linked by factors which cannot be neglected such as the Arp2/3 complex(4). Because of the sheer filament number and density, we may be justified in many cases to consider this system in an averaged sense. Indeed, the role of an individual AF is likely to be small because as far as transport is concerned it forms only a short segment within a mesh and that single filament will not contribute much to the overall mechanical response of the system, since the flexural rigidity of actin is quite low (of order 1e-25 Nm^2 (5)). Hence, it is common and entirely reasonable (in some unsettlingly gross approximation) to model actin subsystem as a hydrogel and control its properties via overall filament density and via its cross-linkers (6–9). By contrast, MTs are not a hydrogel in a great number of cells no matter how much one coarse-grains the description. MTs in many cells are sparse. MT-MT distances on the order of 100 nm are common (10, 11). Reptation of MTs with a MT network is usually not biologically relevant but by contrast reptation of MT filaments in actin gels has received attention (12). The number of MTs in cells is fairly small, to the point where modern imaging and computing potentially allows for all filaments to potentially be tracked. For example fairly large mammalian BSC-1 cells were reported to contain only ~700 MTs (13). Crucially, rigidity of a MT filament (5) is several orders of magnitude higher than that of an AF (of order 1e-23 Nm^2) and MT lengths can be sufficient to span the cell or even extend from MTOC to cell periphery and bend backwards (14). It is not our intent to trivialize the enormous variety of MT networks (e.g. (15)) even under our simplifying assumptions, but the net result of the above considerations is that for a great number of cells the contribution of even a single MT filament to intracellular transport and biomechanics can potentially be accounted for and should not be treated in an averaged sense. Hence, it is often entirely unreasonable to generally model the MT subsystem in cells as a hydrogel (although this may be applicable in some specific cases) and one cannot simply control its properties via filament density or cross-linkers alone. Particularly for MT cytoskeleton, capturing the complexity of the network requires the ability to position multiple filaments individually and precisely in 3D. The task is complicated by the fact that MTs are polar filaments, so that one end is chemically different from the other. Therefore 3D MT assemblies must recapitulate not only the desired filament geometry but also the desired polarity of each filament. Once this minimal set of requirements is achieved, one of course further requires the potential to add associated proteins, cargos and other complexity in a controlled manner.

The benefits associated with precisely modeling transport and mechanics at the level of a complex cytoskeletal network (rather than at the scale of an individual filament) are numerous. When it comes to biomechanics, several key questions become accessible to experimental probing. We know at the level of a single filament that MT rigidity and persistence length depend on the filament contour length (16). This is a simple and intuitive consequence of the fact that longitudinal bonds within each protofilament are mechanically different from lateral tubulin-tubulin bonds. But it is unclear how this picture scales for larger MT assemblies. If individual MTs have a characteristic length scale over which mechanical properties significantly change, then does this length scale also govern the mechanics and spatial dynamics of MT filament networks? It is also unclear how MT-MT cross-links (especially multi-motor cargos) affect network properties. First, rather obviously, cross-links themselves can have variable mechanical properties. Less obvious is the fact that cross-linking of MTs by e.g. motors on cargos occurs via binding to individual tubulin binding sites. Therefore cross-links can potentially have differing effects on network properties depending on how they mechanically couple to the intrinsic anisotropy of each filament. The ability to build 3D MT structures would allow experimental access to all of the above issues. In addition, it would help clarify things on a conceptual level. There is a long standing debate (partially reviewed in 17) as to how much MT cytoskeleton can contribute to cell mechanical properties. The ability to construct increasingly complex MT networks and to study them as a function of their degree of crosslinking and spatial scale would finally establish experimental limits for this broad class of problems.

The ability to precisely model 3D MT networks would also be highly beneficial to studies of molecular motor driven transport. While much experimental modeling to date has been done *in vitro* in bead assays or with *ex vivo* cargo transport on single filaments, these assays only capture a subset of actual cargo navigation in cells. MTs are certainly sparse in many types of eukaryotic cells so there are undoubtedly stretches of cytosolic space where a single filament is all that is accessible to a given cargo. However, much of the recent super-resolution work (10, 11, 18) demonstrates that in many locations MTs are spaced close enough to each other that a single cargo's motors could geometrically reach two or more filaments (a locus which is natural to term MT intersection despite the fact that the terminology is then cargo-specific). So the question of how cargos are routed on realistic MT arrangements (or in physics terms, the problem of experimentally measuring the two point correlation function for active transport on a complex network) cannot be answered without the ability to build these arrangements and to also introduce known and well-characterized cargos into these networks. Ideally, one would start with experimentally modeling traffic rules in the simplest case: a single MT-MT crossing. The resulting statistical picture could then be applied to two or more MT-MT crossings. In principle, cargo behavior at each crossing should be governed by the same overall traffic rules and the motility of a cargo along the clear filament stretches which connect the intersections is already amenable to theoretical modeling. Therefore it should be possible to reduce the routing on a complex network to a Markov chain of navigation traversal events. However, the extent to which rules at each intersections scale for a chain of intersections needs to be experimentally constrained. In other words, if we desire to understand cargo transport on complex cytoskeletal networks it is necessary but not sufficient to be able to experimentally model just one intersection in 3D. The ability to scale up network geometry and topology cleanly and reproducibly is essential for the full benefit to accrue.

Finally, we must not overlook the fact that MTs are a fascinating materials system for nanoscale and micron-scale engineering (19). As Howard lab pointed out, the Young's modulus of MTs is "similar to Plexiglas and rigid plastics" (5). However the aspect ratios of the tubular shapes are dramatic (of order 2000:1). These structures are thus suitable for building *in vitro* scaffolds and (if the approach were sufficiently scalable) MT-based metamaterials. In this respect, one complication is that MTs can be unstable at higher temperatures and can depolymerize or change conformation due to the presence of additional chemical agents. Therefore, for engineering purposes, it is important to be able to stabilize MT structures *in situ*.

RESULTS: We have recently demonstrated an experimental approach to build 3D MT structures *in vitro* (20). Briefly, our system (21) is built around an inverted Nikon Ti-U microscope and has two optical trapping lines admitted from the objective side via a dichroic beam combiner. One optical trapping line is driven by a 1W laser at 1064 nm and is spatially modulated by a holographic mirror to allow the creation of multiple holographic optical traps (HOTs) in the field of view in 3D (i.e. not just in the focal plane of the objective). The other trapping line is driven by a high power diode laser at 980 nm and can be quickly moved in the field of view via either a piezo driven mirror (high trapping power and deflection range) or an acousto-optic deflector (maximum speed). The fast-moving ordinary trap thus compensates for the one weakness of holography – slow spatial reconfiguration.

Given our microscopy capabilities, the fundamental idea is to attach refractive microspheres to MTs and to then use these optically trappable nodes as bead handles (BHs). We assure bead affinity for MTs by decorating their surface with enzymatically dead full-length kinesin-1. Precise MT manipulation requires at least two BHs attached to it, preferably far away from each other (we usually refer to such an assembly as a dumbbell). Once such an assembly is built, it in principle allows a MT to be positioned in 3D via HOT of the two BHs. Crucially, we have shown that dumbbells can be built with high precision and high workflow throughput. In addition, we have demonstrated that model cargos and regulatory chemical agents can be introduced into the system to gradually expand experimental complexity. Our approach to constructing 3D cytoskeletal structures is optimized for MT filaments although other high aspect ratio reasonably rigid building blocks may be used by extending our basic idea.

Previous relevant publications from our lab were aimed at describing the underlying technology and at demonstrating that the approach is feasible and practical. Here, we will discuss how our approach works in practice and how the workflow can be optimized and scaled up.

Storage Depot: If one desires to build a simple 3D MT-MT crossing arrangement (described before 20), then it is often convenient to construct a dumbbell, release it from trapping so that it is allowed to settle to the coverslip "floor" of the chamber. The glass BHs are sufficiently denser than the water-based buffer that they readily sink and do not appreciably diffuse one on the coverslip, especially if both BHs are 0.5 μm in diameter or larger. The location of the dumbbell can then be remembered via some local surface imperfection and it is then usually possible for us to

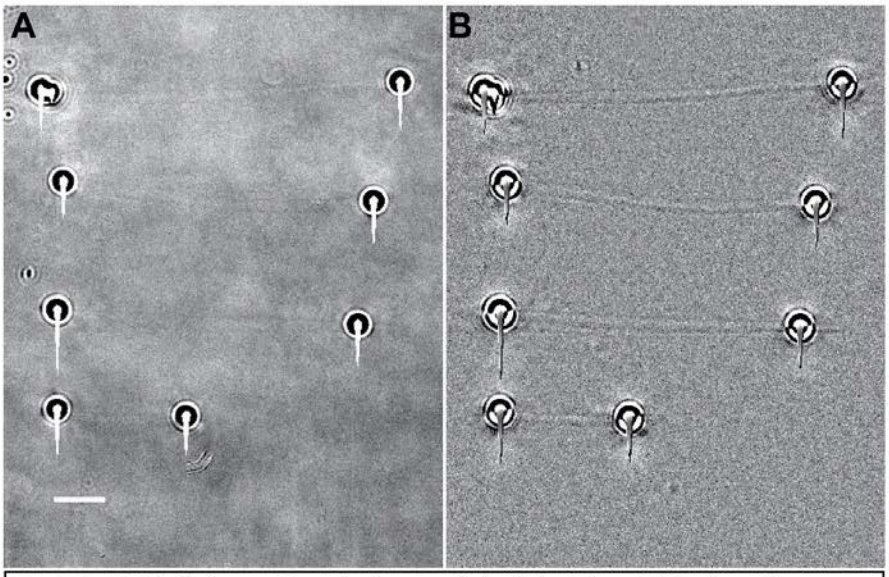

Fig. 1. Four MT dumbbells are resting on the glass coverslip in a designated area. (A) Raw image shows random impurity spots on the coverslip surface. Each bead is imaged with a streaking artefact due to camera oversaturation under our lighting conditions. (B) Filtered frame image showing MT locations more clearly. Here two nearby frames were high-pass filtered and then subtracted from each other to eliminate static background. Scale bar: 5 μm.

build another dumbbell close enough to the first location that finding the first dumbbell is easy. However this approach fails when the number of dumbbells grows. In such cases, we can build dumbbells one by one and drop them off to the coverslip in a selected location (Fig. 1).

In this way, an entire depot of building blocks can be prefabricated and made available for future use. Finding a depot routinely can be aided by adding micrometer scales to the sample stage. The scales need not be extremely high resolution; 20 micron ticks are sufficient assuming that the depot storage covers most of the field of view. Stages with built-in digital readout of global absolute position could offer even more convenience.

Although dumbbells do not diffuse much over experimental time scales when lying on the surface, they can be inadvertently "bumped" by a trap manipulating another object within the depot. That could then lead to undesirable BH-MT cross-linking. To avoid this, some minimal spacing between objects, typically on the scale of a few microns, is practical.

Bead-MT arrangements: The strength of BH-MT affinity can be easily modulated by changing the density of enzymatically dead kinesin-1 on bead surface. We have observed a continuum of assay conditions, from no BH to MT binding to very robust attachment. In the intermediate case, attachment may form slowly or not at all in each case. Testing for whether attachment occurs can be easily done by moving the BH relative to MT and observing whether a MT deforms. We usually aim for our assays to have robust BH-MT attachment. Under those conditions we can form dumbbells most efficiently as previously described (20) by finding a bead with one MT already attached randomly ("mace" arrangement). Another BH can then be placed on the MT at a desired displacement from the first bead.

The use of dumbbells is the most reliable way to assemble 3D shapes but in some cases maces can be the more flexible building blocks. To give a simple example, we can use them to build V-shaped assemblies as shown in

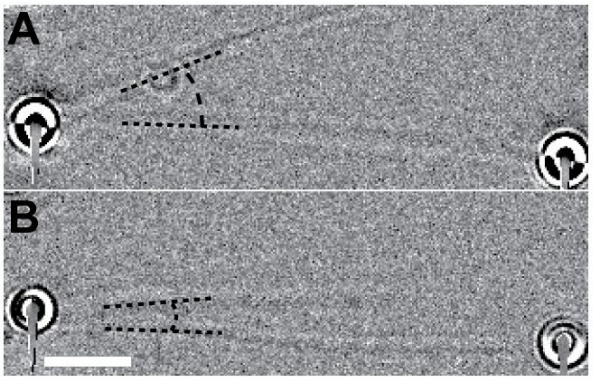

Fig. 2. A dumbbell with a side MT can be a useful construction block. In addition they inform us about the BH-MT attachment - no nodal point pivoting between a reference MT (fixed by the dumbbell) and the MT with one free end is seen. Here pivoting in the range of ~10° to ~25° is seen but larger angles are not attained even when the system is perturbed by the dumbbell moving through solution or the stage moving. Scale bar: 5 μm. Filtering as in Fig. 1B.

Figure 2. These assemblies are useful if one wants to test whether BH-MT bond is via a single dead kinesin homodimer. In particular, we expect to see nodal point pivoting (22, 23) for single kinesin-MT bonds because we use full-length kinesin molecules with unaltered stalk. However, for strong bead-MT attachment assays, we never see such pivoting, suggesting that the bonds are mediated by multiple motors which collectively constrain the angle by which a MT can pivot. One can also build V shapes where all nodes are fixed via BHs but it is not clear at the moment whether actively forcing the MTs to pivot would have the resolution to probe the exact number of BH-MT attachment cross-bridges.

Building complexity: HOT-based construction has to work well in the face of multiple challenges. Among those is the occasional difficulty of MT visualization and the fact that MT diffusion, if left unconstrained, can make it challenging to space the BHs on MTs as desired. For example, we have found placing two beads simultaneously on a completely unconstrained MT with any degree of precision difficult. It is far better to place one bead reliably and then to place the second bead at a desired offset. Therefore, we do not advise building dumbbells and then manipulating them in parallel to try to link them up via a free MT with no attached BHs. Attempting to make multiple BH-MT bonds simultaneously almost never works out well in our hands. Building MT structure one building block at a time is far more prudent.

Populating the depot area with appropriate building blocks is therefore a good start for building 3D filament shapes. Care must then be taken to assemble individual pieces into the final assembly to avoid inadvertent crosslinks and to assure that cross-links are formed at desired locations. For example, consider the pentagonal shape in Figure 3. An interesting challenge here is that this network, as shown, cannot be assembled from dumbbells alone. Instead, maces are used to build a flexible skeleton and the shape is then linked up into the final form using two dumbbells.

Manipulation of maces to allow their proper positioning can be more challenging than for dumbbells because a MT is only controlled via one node. This of course is not sufficient for deterministic 3D manipulation. Nevertheless mace-based construction, as in Fig. 3, is not too onerous. Several factors make assembly process more reliable. First, a single mace can be oriented as desired by moving the bead in space fast enough to flow-align its MT. Second, assembling "starter" shapes from maces can be performed near the surface which provides an effective steric constraint for MT rotation. Finally, one usually does not need to manipulate a single mace beyond building the key "starter" shapes. Once even just two maces are linked up, we have a dumbbell and a MT hanging off of it (a

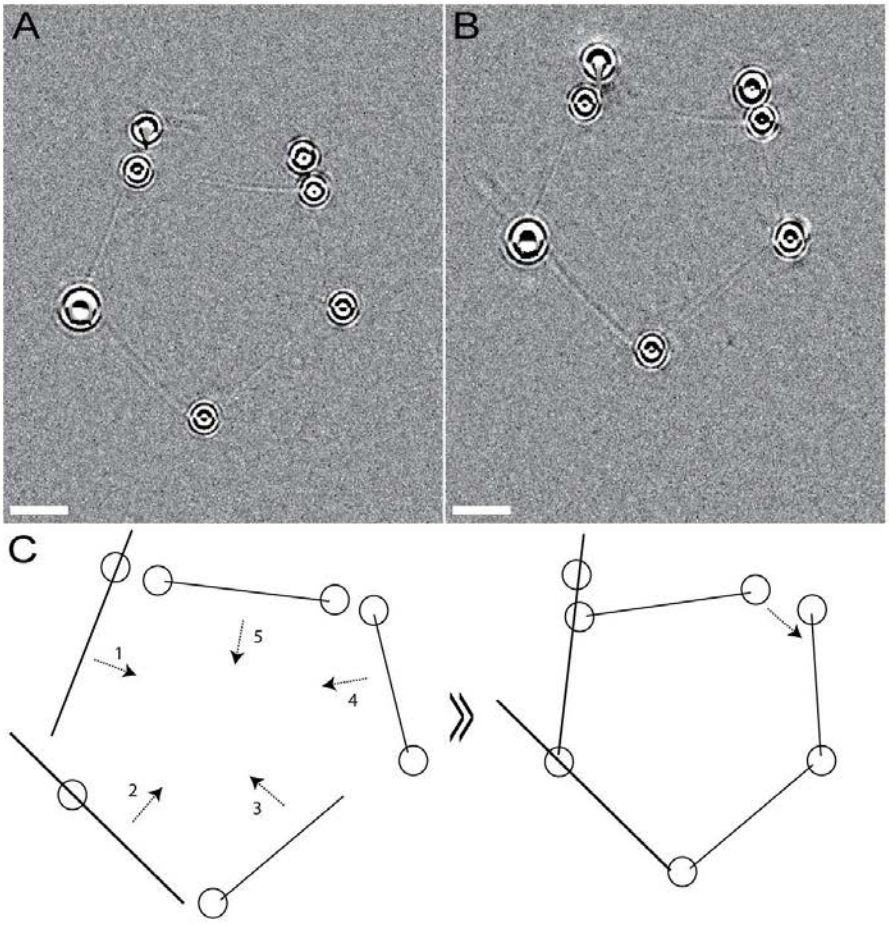

Fig. 3. Pentagonal shape is assembled out of five MTs and seven BHs. Once built (A), the shape can be moved as a whole (B). The assembly process (shown as an Ikea diagram) helps avoid inadvertent cross-links. Scale bar: 5 μm. Filtering as in Fig. 1B.

situation similar to Fig. 2). As discussed above, the MT with an unconstrained end will not diffuse around much thus minimizing the risks of inadvertent crosslinks.

Let us now consider construction into the third dimension. For our current implementation, the requirement for good visualization of MTs in 3D is somewhat limiting the complexity of what can be built with efficient workflow, hence our preference for initially building key components in plane. Construction within one 2D layer can often be facilitated by bringing building blocks in first raising above or below the plane of construction and then

lower or raising them into place. For 3D construction, building blocks can often still be built in a plane and then rotated appropriately before the final assembly.

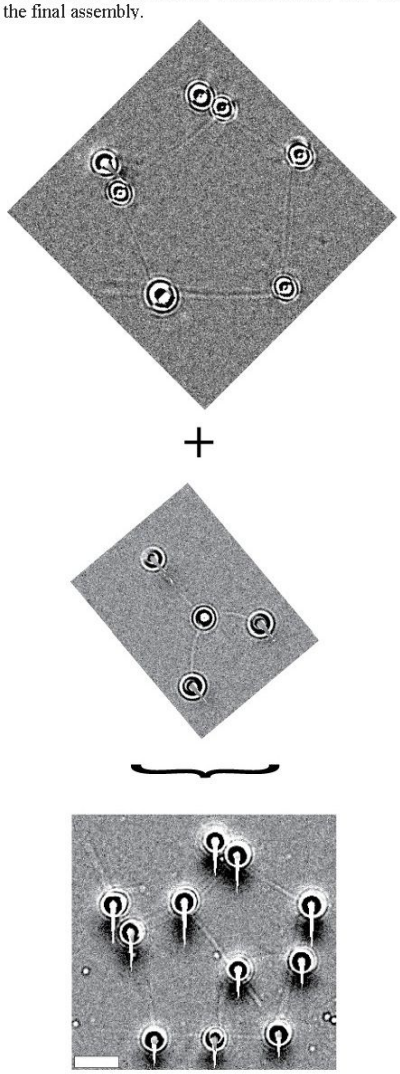

Fig. 4. Pentagonal and Y building blocks are combined to form a more complex arrangement which would be challenging to achieve efficiently by other means of nano-assembly. Assembly time (from design to completion) was ~2 hours. Scale bar: 5 μm. Filtering as in Fig. 1B.

Increasing complexity: Building blocks are not necessarily limited to just maces and dumbbells. As mentioned above, more complex building blocks can be manipulated as a whole and dropped into other shapes to combine into the desired final product (Fig. 4). In the case shown, the Y building block was first assembled from two dumbbells (not shown). The building block was then lifted above the pentagon and finally lowered into place. The Y shape was slightly angled as it was lowered to make sure that one BH at a time made contact with the pentagon MTs. Building blocks such as the ones shown here can in principle also be stored in designated depot areas.

Another barrier to increasing complexity that warrants discussion is available space. The exact dimensions of the volume accessible to HOT vary with the choice of the objective: our typical choices are Nikon 60X water immersion and 100X oil high NA objectives and of course the 60X allows for higher accessible volume. With 100X objective, our volume is nearly cubic (~50 micron on the side) though working at high z depth requires additional care. Despite this space limitation, the building capacity of the system is far greater. For example, we manipulated the pentagon shape (Fig.3 and 4) for some duration of time via only some nodes while other nodes were moved off-screen. The final assembly occurred fully within the field of view however it is now clear that stable shapes can be moved off screen so long as they are structurally connected to the structure being trapped within the field of view. Therefore MT structures can potentially be scaled from sub-micron scale to sub-millimeter scale or even larger.

Additional cytoskeletal structures: The structures considered so far have been chosen to illustrate building techniques and practical assembly issues which we have dealt with to assure reliable, scalable, high throughput construction. It is also worth highlighting how the current system can be used to build other types of biologically relevant topologies. For example, a very exciting development in the field of MT networks has been the discovery that in some cases MTs can nucleate along other MTs giving rise to internally branched MT asters (aka extended star topology). These types of topologies are experimentally accessible via HOT construction (Fig. 5).

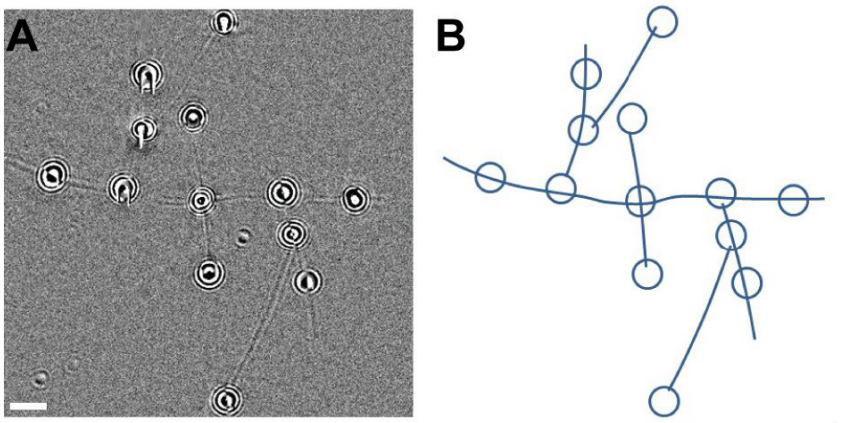

Fig. 5. An example of an extended star MT network (A) and a schematic of its topology (B) constructed *in vitro*. The network shown here is resting on the coverslip floor and its nodes are thus free to undergo limited diffusion. Thus the shape changes over time but MT bending and rotation are not sufficient to bring BHs next to nearby MTs and cross-link the structure. Scale bar: 5 μm. Filtering as in Fig. 1B.

Likewise, we have previously shown that MT-MT crosses can be built *in vitro* and used to study transport at filament intersections (20). However this demonstration focused on a single intersection. Yet, as discussed above, it will soon be necessary to show that the rules which will be experimentally established for a single intersection can scale to more complex case of multiple intersections. In this example, it is important that the MTs are held in place by optical traps. The geometry can then be adjusted on the fly as desired (Fig. 6). Of course the other benefit is that forces exerted by motors during tug-of-war events can be quantified (20).

Remaining challenges and conclusions: Several improvements to the presented technique are clearly worth pursuing in the future.

1. It is increasingly clear that the efficiency of the assembly process depends heavily on our ability to analyze the structure to be built and partition it into optimal building blocks. What constitutes optimal is a balance of several factors. The blocks themselves need to be easy to build, and space-efficient to store in a depot. Of course they should also allow for a straightforward assembly workflow which would minimize the risk of inadvertent MT-BH crosslinking.

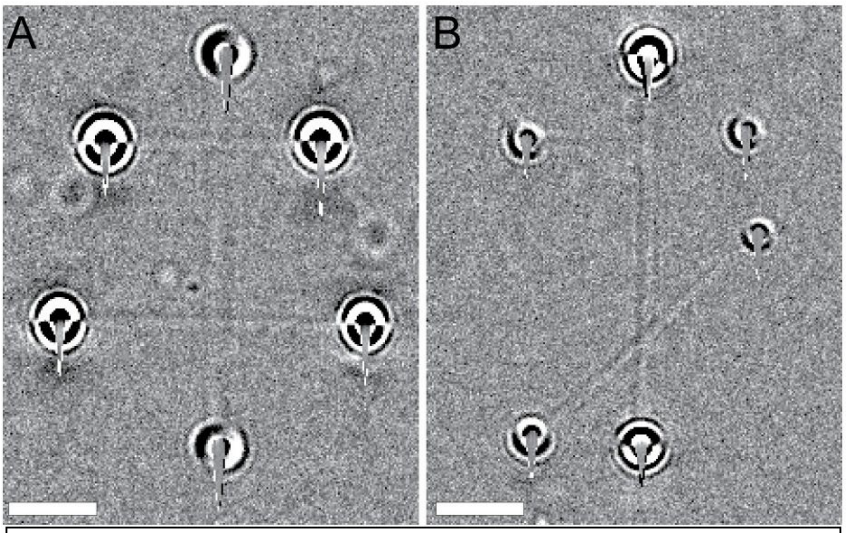

Fig. 6. Two MT-MT crosses are formed by three dumbbells. All dumbbells are held in independent traps, so that the structures are not crosslinked and intersections angle can be adjusted from e.g. normal (A) to 45° (B) for one of the intersections. Scale bar: 5 μm. Filtering as in Fig. 1B.

2. It is important to improve MT imaging. So far, label-free imaging has proven adequate but it is clear that an alternative is desirable, especially for maximizing the 3D potential of the technique. The problem is that structural assembly and subsequent imaging can take hours of work with illumination conditions dictated by the needs of the experiment. Therefore any signal type that can be readily bleached out via excessive illumination is likely not optimal. Techniques like iScat may be preferable in this case but have not yet been explored.

3. As design and build rules become more set, it will clearly be desirable to automate the construction of MT-based structures. This development would allow potentially much faster construction with higher complexity.

The MT cytoskeleton modeling technique we have developed certainly can be improved upon but as is it already holds much promise for biophysical studies, e.g. in biomechanics, MT-based transport and nanoengineering. We demonstrated here that the approach is highly scalable and extensible. Incorporating more MTs into the structures and building larger structures is possible and in fact straightforward for many biologically relevant designs.

Acknowledgements: This work was supported by NSF grant number ENG-1563280 to M.V.

References cited:

1. Firman, K., and J. Youell. 2013. Molecular Motors in Bionanotechnology. CRC Press.
2. De, S., W. Hwang, and E. Kuhl. 2014. Multiscale Modeling in Biomechanics and Mechanobiology. Springer.
3. Alberts, B., A. Johnson, J. Lewis, M. Raff, K. Roberts, and P. Walter. 2002. Molecular Biology of the Cell. 4th ed. Garland Science.
4. Blanchoin, L., R. Boujemaa-Paterski, C. Sykes, and J. Plastino. 2014. Actin Dynamics, Architecture, and Mechanics in Cell Motility. Physiol. Rev. 94: 235–263.
5. Gittes, F., B. Mickey, J. Nettleton, and J. Howard. 1993. Flexural rigidity of microtubules and actin filaments measured from thermal fluctuations in shape. J. Cell Biol. 120: 923–934.
6. Khan, S.M., R. Ali, N. Asi, and J.E. Molloy. 2012. Active actin gels. Commun. Integr. Biol. 5: 39–42.
7. Stricker, J., T. Falzone, and M. Gardel. 2010. Mechanics of the F-actin Cytoskeleton. J. Biomech. 43: 9.
8. Upadhyaya, A., and A. van Oudenaarden. 2003. Biomimetic systems for studying actin-based motility. Curr. Biol. CB. 13: R734-744.
9. MacKintosh, F.C., and P.A. Janmey. 1997. Actin gels. Curr. Opin. Solid State Mater. Sci. 2: 350–357.
10. Huang, B., W. Wang, M. Bates, and X. Zhuang. 2008. Three-Dimensional Super-Resolution Imaging by Stochastic Optical Reconstruction Microscopy. Science. 319: 810–813.
11. Min, J., C. Vonesch, H. Kirshner, L. Carlini, N. Olivier, S. Holden, S. Manley, J.C. Ye, and M. Unser. 2014. FALCON: fast and unbiased reconstruction of high-density super-resolution microscopy data. Sci. Rep. 4.
12. Shah, J.V., L.A. Flanagan, D. Bahk, and P.A. Janmey. 1997. Reptation of Microtubules in F-Actin Networks : Effects of Filament Stiffness and Network Topology on Reptation Dynamics. In: Symposium K – Materials Science of the Cell. . p. 27 (5 pages).
13. Schulze, E., and M. Kirschner. 1987. Dynamic and stable populations of microtubules in cells. J. Cell Biol. 104: 277–288.
14. Zhang, D., K.D. Grode, S.F. Stewman, J.D. Diaz-Valencia, E. Liebling, U. Rath, T. Riera, J.D. Currie, D.W. Buster, A.B. Asenjo, H.J. Sosa, J.L. Ross, A. Ma, S.L. Rogers, and D.J. Sharp. 2011. Drosophila katanin is a microtubule depolymerase that regulates cortical-microtubule plus-end interactions and cell migration. Nat. Cell Biol. 13: 361–370.
15. Chernobelskaya, O.A., I.S. Grigoriev, I.B. Alieva, and I.A. Vorobjev. 2001. Analysis of Different Methodological Approaches to Measuring Microtubule Length in the Cytoplasm of Cultured Cells. Russ. J. Dev. Biol. 32: 51–58.
16. Pampaloni, F., G. Lattanzi, A. Jonás, T. Surrey, E. Frey, and E.-L. Florin. 2006. Thermal fluctuations of grafted microtubules provide evidence of a length-dependent persistence length. Proc. Natl. Acad. Sci. U. S. A. 103: 10248–10253.

17. Brangwynne, C.P., F.C. MacKintosh, S. Kumar, N.A. Geisse, J. Talbot, L. Mahadevan, K.K. Parker, D.E. Ingber, and D.A. Weitz. 2006. Microtubules can bear enhanced compressive loads in living cells because of lateral reinforcement. J. Cell Biol. 173: 733–741.

18. Bálint, Š., I.V. Vilanova, Á.S. Álvarez, and M. Lakadamyali. 2013. Correlative live-cell and superresolution microscopy reveals cargo transport dynamics at microtubule intersections. Proc. Natl. Acad. Sci. 110: 3375–3380.

19. Bachand, G.D., E.D. Spoerke, and M.J. Stevens. 2015. Microtubule-based nanomaterials: Exploiting nature's dynamic biopolymers. Biotechnol. Bioeng. 112: 1065–1073.

20. Jared Bergman, Olaolu Osunbayo, and Michael Vershinin. in press. Constructing 3D microtubule networks using holographic optical trapping. Sci. Rep. .

21. Butterfield, J., W. Hong, L. Mershon, and M. Vershinin. 2013. Construction of a high resolution microscope with conventional and holographic optical trapping capabilities. J. Vis. Exp. JoVE. .

22. Howard, J., A.J. Hudspeth, and R.D. Vale. 1989. Movement of microtubules by single kinesin molecules. Nature. 342: 154–158.

23. Lakämper, S., A. Kallipolitou, G. Woehlke, M. Schliwa, and E. Meyhöfer. 2003. Single Fungal Kinesin Motor Molecules Move Processively along Microtubules. Biophys. J. 84: 1833–1843.

CHAPTER 4

CARGO NAVIGATION ACROSS 3D MICROTUBULE INTERSECTIONS

4.1 Abstract

The eukaryotic cell's microtubule cytoskeleton is a complex 3D filament network. Microtubules cross at a wide variety of separation distances and angles. Prior studies *in vivo* and *in vitro* suggest that cargo transport is affected by intersection geometry. However, geometric complexity is not yet widely appreciated as a regulatory factor in its own right, and mechanisms that underlie this mode of regulation are not well understood. We have used our recently reported 3D microtubule manipulation system to build filament crossings *de novo* in a purified *in vitro* environment and used them to assay kinesin-1 driven model cargo navigation. We find that 3D microtubule network geometry alone significantly influences cargo routing, and, in particular, that it is possible to bias a cargo to pass or switch just by changing either filament spacing or angle. Further, we capture our experimental results in a model which accounts for the full 3D geometry, stochastic motion of the cargo and associated motors, as well as motor force production and force-dependent behavior. We use a combination of experimental and theoretical analysis to establish the detailed mechanisms underlying cargo navigation at microtubule crossings.

4.2 Introduction

The microtubule (MT) network in eukaryotic cells is typically a dense, highly variable, three-dimensional (3D) mesh (Figure 4.1A). MT network topologies are known to vary widely between cells (Schnorrenberg et al., 2016) and even between cells of the same type and lineage (Dong et al., 2015). Within a given network, MTs converge to form crossings at a variety of filament separations, and angles of intersection. Often, the crossings feature interfilament separations that are comparable to the scale of the cargos

found within the cell (Figure 4.1A). At these “intersections,” a cargo, with multiple motors on its surface, can potentially interact with several MTs simultaneously; a scenario known as Tug-of-War (ToW) (Müller et al., 2008; Osunbayo et al., 2015). The cargo can then either pass along the original MT, switch to the intersecting filament, pause, or detach. The probabilities of these outcomes are known to be sensitive to the 3D layout of the filaments (Bálint et al., 2013; Erickson et al., 2013; Ross et al., 2008b) but the mechanistic details of this phenomenon are unclear. Given that the architecture/topology of the MT cytoskeleton serves as a persistent and pervasive regulator of cargo transport, its role in cargo routing warrants a thorough investigation.

The importance of MT cytoskeletal architecture is underscored by the fact that MT network remodeling occurs often in various diseases and during normal cellular processes. For example, neuritic de-arborization or restructuring is often encountered in neurodegenerative diseases (Di Polo, 2015; Van Battum et al., 2015). Microtubule remodeling is also observed in many neoplasias (Parker et al., 2014) and is associated with pathways often disturbed in cancers (Galmarini et al., 2003) and formins (Chesarone et al., 2010; Young et al., 2008). There is also evidence that suggests the geometry of the MT network, itself, acts as a regulator to tune insulin granule secretion in mouse pancreatic β-cells (Zhu et al., 2015).

The cell can use multiple mechanisms to modulate its MT architecture. MTs can be locked in parallel (Fink et al., 2009) or antiparallel (Subramanian et al., 2010) alignment via cross-linking. Axonal branching generally shows a preference for normal angles (Kalil and Dent, 2014); low branch angles can arise from MT nucleating factors (Petry et al., 2013). The cell can set overall MT spacing by simply controlling the amount of

polymerized tubulin, either via regulation of expression levels (Dumontet et al., 1996) or filament stability (Desai and Mitchison, 1997).

Filament spacing can also be controlled via MAPs that cross-link microtubules (Hirokawa et al., 1988). External factors which affect cell shape can also regulate MT network topology (Gomez et al., 2016). Finally, MT crossings are known to be special loci for intracellular regulation (Hamant, 2013). Currently, the implications of these topology variations for cargo logistics and overall biomechanics are not quantitatively understood.

Decoupling the influence of the MT network's 3D topology from regulatory protein factors is challenging. The same pathways that drive network remodeling can also couple to motor regulation. The result is that, to date, the impact of geometric changes in MT networks on intracellular cargo transport has been difficult to isolate and quantitate. It is common to think in terms of chemical regulation. However, to truly understand how intracellular cargo transport functions, it is critical to gain a baseline understanding of how the 3D MT geometry *alone* impacts cargo distribution, starting at the most fundamental level of the MT network: individual MT-MT intersections.

Studying cargo navigational behavior as a function of 3D network geometry poses considerable experimental challenges. *In vivo* investigations cannot easily decouple chemical and topological regulation, as discussed above. Moreover, although theoretical work highlights its importance (Erickson et al., 2013) *in vitro* bead assays that use traditional MT-glass deposition techniques are also unable to model MT-MT crossings with controlled filament separation (Ross et al., 2008b; Vershinin et al., 2007), though they provide a useful starting point for any study in full 3D.

To address this question, we developed an *in vitro* system to suspend and dynamically manipulate multiple individual MT filaments in 3D. Each MT is manipulated individually via holographic optical trapping (HOT) of two or more bead handles (BH), as previously described (Bergman et al., 2015). We used this bottom-up approach to systematically construct MT-MT intersections featuring various angles and separations. We then measured the statistics of kinesin-1 driven model cargo (MC) transport on these model MT geometries, and used this data to constrain 3D simulations. We show from experimental data and theoretical analysis that navigational outcomes exhibit systematic variation based on 3D MT intersection geometry. Further, we propose dynamic mechanisms that explain the observed preferences.

4.3 Results

4.3.1 Experimental setup

The broad aim of this work is to understand the impact of cytoskeletal geometry on intracellular transport. A comprehensive experimental model of all possible geometries (e.g., Figure 1A) is well beyond the scope of any singular study, so we restricted our scope to representative model scenarios. We focused on the simplest type of intracellular MT intersections − where just two filaments cross (Figure 4.1A, inset). We used silica microspheres, driven by full length KHC homodimers, as our MC. This is a common, albeit simplified model for *in vitro* work. We chose to focus on assays outside the single-molecule regime because there is substantial evidence that cargos in cells are often driven by multiple motor ensembles, and indeed, multiple-motor ensembles are essential for a ToW to develop.

We used *in vitro* 3D MT manipulation via HOT (Bergman et al., 2015) to examine three filament spacings: zero, radius, and diameter of the MC. Our MCs were 1 μm in diameter, hence, we constructed and observed MC transport across model intersections featuring 3 separation distances (0μm, 0.5μm, and 1μm). We decided to only parametrize this geometric range because the probability of a cargo interacting with both MTs for crossing separations greater than the cargo diameter quickly becomes negligible. For each separation distance, we examined three different angles of intersection: acute (MT polarities nearly counter aligned), normal (90°), obtuse (MT polarities nearly aligned), for a total of nine geometric conditions.

We chose silica microspheres as our MCs because their density is ≈ 2.2x that of water. This biased the cargo to hang below the MT to which it was engaged, although Brownian motion along all three axes was both expected and observed. Thus, in our setup, we always deposited the MC (via HOT) onto the "overpass" MT, such that the hanging cargo would be likely to encounter the lower, crossing MT (Figure 4.1B). With this setup, our 0μm separation experiments resemble the "underpass" MT geometry in prior crossing experiments, in which MTs were attached to a glass substrate (Ross et al., 2008b; Vershinin et al., 2007). However, our experimental model allows for MT bending, twisting, and vibrations which cannot be recapitulated when MTs are firmly attached to a solid substrate. The absence of the solid glass substrate in our work is a major difference since the cargo can explore many more three-dimensional paths as it negotiates the intersection.

4.3.2 Final navigational outcomes depend on 3D geometry

For each of the nine MT network arrangements in our assays, we quantified final cargo routing outcomes strictly in terms of, “switching” or “passing,” because detachment at intersections was negligible. In addition, we do not report pause events, because we can characterize the entire navigational event, even in cases where the MC navigational choice takes several seconds to make. Below, we report switching probability only, as passing probability is complementary.

Our results suggest that 3D MT network topology *alone* can be an effective regulator of cargo routing (Figure 4.1C). Geometries in the upper left corner of the table promote switching while those in the lower right corner promote passing. Therefore, routing outcomes are determined by multiple geometric factors interacting in nontrivial ways. Disentangling these factors by intuition alone is challenging, therefore, we relied upon *in silico* modeling. Helpfully, many fine mechanistic details are resolved by our experimental approach (see section 4.3.3), constraining the *in silico* model.

4.3.3 Characterization of Tug-of-War events

A cargo that does not engage in a ToW, does not switch; hence, precisely distinguishing between ToW and non-ToW events is critical to dissect the mechanisms that lead to differential switching probabilities. Our spatiotemporal resolution is sufficient not only to establish whether a ToW took place, but also to precisely determine ToW durations.

We can readily identify ToW start and end by observing significant MC displacements away from MT axes and associated MT deflections (Figure 4.2A). MC tracks for representative pass (Figure 4.2B), and switch (Figure 4.2C) events are shown,

along with their displacements projected along the axes of the intersecting MTs. A ToW start can be identified with the beginning of a sustained displacement upon the crossing MT's axis. ToW end can then be identified when the cargo snaps back upon dissociation from either the primary or crossing MT. BH displacements can also be used as an indicator of a ToW because the MC motors engaged in a ToW will exert force on the MTs that ultimately displaces the BHs (Figure 4.1B, 4.2A *middle*, D).

Although BH displacements can help confirm ToW presence and duration, their greatest benefit is that they are an indicator of how many motors were exerting force on the bead. We set the trap stiffness at ~1pN/100nm, so that a single kinesin motor could not pull the BH out of the trap (escape event) but two or more motors working together could do so readily (Figure 4.3). Quantifying collective activity of multiple motors via trap escape forces is a well-established approach both *in vivo* (Ashkin et al., 1990; Gross et al., 2002) and *in vitro* (McKenney et al., 2010) and has been validated *in silico* (McKenney et al., 2010). This setup allowed us to control the surface density of motors on MCs by discarding assays in which BH escape fraction exceeded 25% of total events. This provided refined control on top of the more crude and variable approach of controlling motor concentration at incubation time. It also provided confidence that ToWs in our assays were dominated by forces from 1-2 kinesin motors; more motors are likely engaged on the MT but not all are positioned to exert force during the ToW.

4.3.4 Mechanisms of cargo routing

The ability to sensitively detect ToW events allowed us to quantify their probability. We could then also examine the probability for the cargo to pass or switch

conditional on ToW occurrence. This analysis is informative because these probabilities reveal different aspects of cargo dynamics (Figure 4.4). Our data indicate that ToW probability is sensitive to 3D geometry: it is higher for narrower filament separations, and for acute/obtuse angles (Figure 4.4A). For 0μm separations, ToW probability is so high that significant differences as a function of angle may not be practical to measure. A different pattern of navigational outcomes emerged when trivial passes (no-ToW events) were omitted (Figure 4.4B vs. Figure 4.1C). Four out of nine geometries show switch probabilities close to 50%. We also record switch probabilities that are significantly higher than 50% for the following geometries: *0 μm normal*, *0 μm acute*, and *.5 μm acute* ($p < .05$ *Barnard's test)*. We conclude that geometric constraints can promote or inhibit switching outcomes for ToW events.

4.3.5 A mathematical model of cargo transport reproduces observed switch probabilities

As mentioned in the previous section, it is difficult to disentangle the mechanism through which each factor acts to (in concert) determine ToW and switching probabilities. Therefore, to gain further insight into the mechanism determining cargo routing, we constructed an *in silico* model of cargo transport. This model allows us to examine experimentally unobservable details, such as how motor locations, bound states, and force states change with time.

The model incorporates relevant experimental details including: the well-established properties of kinesin-1 motors, and cargo translational and rotational diffusion (Figure 4.5A), however, simulated MTs do not move, twist, or bend. Five hundred cargo

trajectories were simulated independently for each assay geometry, and probabilities of ToW and switching were then determined analogously to the experimental data. For full simulation details and parameter fitting procedure, see Appendix. Briefly, there were two parameters that could not be established from current experiments or prior literature: average motor number attached to MCs and each motor's on-rate. These two parameters were constrained by matching three experimental observations: ToW probability as a function of geometry, fraction of BH escape events, and MC run lengths (See Appendix). Thus, the model is fully constrained and therefore predictive.

We found good agreement between experimentally observed and theoretically predicted probabilities of ToW'ing and switching (Figure 4.5B-D). We now turn to investigate the quantitative details of ToW and switching (next two sections), and their implications for the mechanisms of cargo navigation at MT intersections.

4.3.6 The influence of intersection geometry on ToW probability

The longer a cargo spends within reach of the primary and intersecting MTs (henceforth, the ToW zone), the more chances unbound motors on the cargo have to engage the intersecting MT. This phenomenon can be understood from a simple, heuristic model. If we consider the cargo as having a single rate of binding to the crossing MT given by k_{on}^{macro}, the probability the cargo binds to the crossing MT before leaving the ToW zone is given by

$$p_{ToW} = \frac{k_{on}^{macro}}{k_{on}^{macro} + v/d_{ToW}},$$

where v is the cargo velocity and d_{ToW} is the length of the ToW zone. This simple model

can accurately reproduce experimental ToW probabilities for both the 0.5 μm and 1 μm separation distance geometries (Figure 4.6), but not for the 0 μm separation geometries. This strongly suggests that there are mechanisms at play for 0 μm separations which are not present at other distances (see below).

On the other hand, our full model closely recapitulates all experimental ToW probabilities, including 0 μm separation data. It is encouraging that the model captures several *a priori* intuitive features of the system. For 0 □m geometries, if a cargo is driven by multiple motors then there is guaranteed to be a pool of motors able to bind the crossing MT (namely, the already engaged motors). Thus, we *a priori* expect the ToW probability for all angles to be close to 1, which our model indeed reproduces. For 0.5 μm and 1 □m geometries, we expect higher ToW probability for longer ToW zones (acute and obtuse angles). Indeed, simulated ToW probabilities were smallest for 90° intersections (Figure 4.5B). Also as expected, they were symmetric about the normal angle (since kinesin binding is not affected by MT polarity). Simulated ToW probabilities also increased when MT separation decreased from 1 μm to 0.5 μm, as expected. When the intersecting MT encounters the cargo midsection, at 0.5 μm separations, it samples more of the bead's surface area. Hence, more motors are given a chance to engage on the crossing MT.

4.3.7 The influence of intersection geometry on navigational outcomes given ToW

Experimentally, we observe a large range of geometries (most 0.5 μm and 1 μm geometries) where the conditional probability to switch is ~50%. At first glance, this appears to be a relatively intuitive result: if ToW lasts ~ 1 second or more (our experimental

ToW durations average ~ 3 sec, Figure 4.7), then the motor team engaged on the crossing MT should be able to reach steady state (Erickson et al., 2011), and become equal in number to the primary motor team. With two equivalent ways to proceed, the probability of either choice would indeed be ~50%. However, such a consideration is too simplistic as we discuss directly below.

Experimental results allow for sensitive identification of ToW, so that ToW events can be analyzed separately from trivial "no-ToW" intersection passages (Figure 4.4). The same analysis can be performed for simulated events (Figure 4.5B-D) and the two sets of results largely agree. A careful analysis of the simulations helps us shed light on the mechanistic details of cargo navigation.

We first assessed whether the number of motors in the two ensembles is, in fact, equal in our simulations. We find that contrary to naïve expectation, the number of engaged motors on the secondary MT is comparable but consistently lower than that on the primary MT (ratio of ~0.7; Figure 4.8). The reason is that the motors already engaged on the primary MT constrain the bead from full range of linear and rotational diffusion. Once a ToW starts, the bead diffusion is even more constrained which then curtails the number of motors that can reach the secondary MT. We therefore find that the numbers of motors in the ToW'ing teams are not equal: the team of motors pulling along the primary MT has a consistent advantage. However, the two paths to proceed are not equivalent either. The crossing MT itself can serve as an obstacle for bead progress and exert a force which hinders the MC from passing (Figure 4.5G). The smooth decrease from passing to switching prevalence across our experimental geometries (Figure 4.4B) therefore reflects the balance between net motor activity (which is biased in favor of moving along the

primary MT) and steric hindrance from the crossing MT.

4.3.8 The limits of geometric regulation

Our results establish that a single MT intersection can significantly bias cargo routing towards more switching or more passing. Can a single MT intersection produce a near 100% bias for switching or passing? What are the mechanisms which affect these limits? It is easy to see that ~100% passing naturally occurs for intersections with filament separation much greater than MC diameter. Is 100% switching attainable? To address this, we consider two special cases which lead to elevated probability to switch, and their broader implications for geometric regulation. For completeness, we also discuss each experimental geometry individually in the appendix.

4.3.9 Low filament separations

A closer look at the geometric setup (Figure 4.5E) makes it clear that the 0 μm case is qualitatively distinct. At 0 μm separation, the crossing MT sterically hinders the motors engaged on the primary MT, but not for the MC itself. To pass, the cargo can "hurdle" over the crossing MT due to Brownian motion but this is improbable for our large silica MCs (density ≈ 2.2x water). This would also be unlikely in the viscous cytosolic environment (even for smaller cargos). The only other way to pass is by a mechanism we refer to as "monkey-barring." To pass via monkey-barring, the MC must first diffuse underneath the crossing MT so that some of the unengaged motors on its surface could bind to the distal side of the primary MT. The motors proximal to the crossing MT must then gradually disengage.

The above suggests that passing at 0 □m separation should have a sensitive dependence on the diffusion properties of the medium. This is indeed seen in our simulations (Figure 4.5F). In fact, for viscosities close to intracellular range, where cargo diffusion is suppressed, the preference to switch approaches 100%.

4.3.10 Acute angles / intermediate separations

Why is switching more prevalent for 0.5 μm acute geometry? Again, this must be due to the crossing MT acting as a strong hindrance, but the mechanism cannot be the same as in the previous section. Here, monkey-barring is not feasible but hurdling is. Evidently, in this case, for switching probability to be elevated, hurdling must be suppressed.

The vertical forces associated with the ToW for 0.5 μm acute geometry pull the MC between MTs. This effectively wedges the cargo between the two MTs, which indeed prevents hurdling. We refer to this mode of steric hindrance as “chop-sticking.” Note that in our simulations, MTs were not allowed to bend, which would likely be a factor under experimental conditions. In reality, the two motor teams engaged in a ToW during chop-sticking would be expected to pull the two MTs closer together, which would make the crossing MT an even stronger obstacle to passing. This is likely the reason why experimentally observed switching probability for 0.5 μm acute geometry is somewhat higher than theoretical prediction.

4.4 Discussion

Cargos driven by multiple motors can exhibit incredibly complex behavior. Even when one considers this for a single cargo moving along a single MT, the system complexity is sufficient to lead to highly nontrivial emergent behaviors. The number of motors in biologically relevant systems is typically small which necessitates highly detailed experiments and modeling to account for not only averaged behavior but also the effect of fluctuations. The addition of just one more filament adds such complexity that the emergent behaviors can dramatically diverge to give rise to discrete outcomes: passing and switching. It is therefore a fascinating model system for emergent behaviors in biology.

We have modeled this problem in a highly controlled experimental environment in which we imposed very specific restrictions on cargo size and other experimental variables. We then performed highly detailed modeling of our system *in silico* to generalize our experimental results. We were thus able to infer the key processes which underlie our observations. This enables us to extrapolate how cargo routing might function in cells (and other environments).

Our analysis shows that the team of motors driving the cargo along the primary MT is generally at an advantage, even when the ToW is prolonged. This implies that there is an inherent bias to pass. However, our data show that for many geometric conditions passing and switching is balanced, and in some cases, switching dominates. The missing factor which shifts the balance between passing and switching is the extent to which the crossing MT acts to sterically hinder the motors progressing along the primary MT.

We show that the crossing MT can indeed be an effective obstacle, especially when

it intersects at an acute angle with intermediate separation, or near-zero MT-MT separation. Both types of geometries significantly inhibit passing but via different mechanisms: intermediate separations with acute angles lead to chop-sticking, while near-zero filament separations mean that passing is only accessible by means of monkey-barring (which is an unlikely event).

Our simulations generally closely follow the experimental results but two important deviations are seen: the conditional probability to switch given that ToW already started is higher in experiments than in simulations. Also, the time a cargo spends at the intersection is higher in the experiment than in simulation (Figure 4.7). In both cases, the discrepancy is clearly linked to the fact that we model MTs as an infinitely rigid rod. To date, MT rigidity has been mostly studied separately from MT-based transport. Our work suggests that MT bending and more generally biomechanics of the MT cytoskeleton must be taken into account in future studies of intracellular motility as they are a non-negligible contributor to cargo routing.

A faithful and detailed *in silico* model of cargo motility and the ToW process enables us to then speculate about cargo navigation patterns beyond our specific conditions. First, we show that if viscosity increases, then switching would be further favored for near-zero filament separations. In effect, our simulations lead us to speculate that not only MT geometry but also local microrheology can be a regulator of cargo routing.

We also predict that extremely short motors should find reaching across the crossing MT for near-zero separations particularly difficult, so cargos driven by very short motors would preferentially switch at intersections. It is tempting to speculate that overall kinesin length evolved to reduce the probability of cargos getting trapped in filament-

filament switching loops.

On a more architectural level, our results suggest that for each cargo type and size there is a critical MT density at which efficient transport can be inhibited by too much switching at intersections. This prediction from the single molecule level dove-tails with the more qualitative observations for the insulin secretion process (Zhu et al., 2015).

Our work opens many new directions for future work, including studies of more complex intersections, more complex cargos and motor complexes. Together these baseline studies can then serve as a basis for studying chemical regulation of motility in the context of cytoskeletal network geometry. A gradual from-the-bottom-up increase in complexity can then gradually lead to comprehensive quantitative understanding of intracellular cargo fluxes, from a single-molecule mechanistic perspective.

4.5 Methods

Optical trapping and 3D motility experiments: our holographic optical trapping and bead assays were performed as previously described (Bergman et al., 2015). However, in present work, enzymatically dead KIF5A heavy chain dimers were adsorbed onto bead handles nonspecifically. Switch/pass outcomes were assessed live during the experiments from the video feed and recordings were conducted until definitive outcome was attained. Video records of bead positions were tracked using custom software (MATLAB, MathWorks, Natick, MA).

Statistical analysis: much of our data are in the form of contingency tables. Barnard's exact tests were used to assess significance of differences between outcomes.

Simulations: See Appendix for detailed discussion.

4.6 References

Amos, L.A., and Schlieper, D. (2005). Microtubules and maps. Adv. Protein Chem. *71*, 257–298.

Andreasson, J.O.L., Milic, B., Chen, G.Y., Guydosh, N.R., Hancock, W.O., and Block, S.M. (2015). Examining kinesin processivity within a general gating framework. Elife *2015*, 1–44.

Ashkin, A., Schütze, K., Dziedzic, J.M., Euteneuer, U., and Schliwa, M. (1990). Force generation of organelle transport measured in vivo by an infrared laser trap. Nature *348*, 346–348.

Atherton, J., Houdusse, A., and Moores, C. (2013). MAPping out distribution routes for kinesin couriers. Biol. Cell *105*, 465–487.

Bálint, Š., Verdeny Vilanova, I., Sandoval Álvarez, Á., and Lakadamyali, M. (2013). Correlative live-cell and superresolution microscopy reveals cargo transport dynamics at microtubule intersections. Proc. Natl. Acad. Sci. U. S. A. *110*, 3375–3380.

Van Battum, E.Y., Brignani, S., and Pasterkamp, R.J. (2015). Axon guidance proteins in neurological disorders. Lancet Neurol. *14*, 532–546.

Beeg, J., Klumpp, S., Dimova, R., Gracià, R.S., Unger, E., and Lipowsky, R. (2008). Transport of Beads by Several Kinesin Motors. Biophys. J. *94*, 532–541.

Bergman, J., Osunbayo, O., and Vershinin, M. (2015). Constructing 3D microtubule networks using holographic optical trapping. Sci. Rep. *5*, 18085.

Block, S.M. (2007). Kinesin motor mechanics: binding, stepping, tracking, gating, and limping. Biophys. J. *92*, 2986–2995.

Block, S.M., Goldstein, L.S., and Schnapp, B.J. (1990). Bead movement by single kinesin molecules studied with optical tweezers. Nature *348*, 348–352.

Bo Huang, Wenqin Wang, Mark Bates, and X.Z. (2008). Three-dimensional Super-resolution Imaging by Stochastic Optical Reconstruction Microscopy. Science (80-.). *319*, 810–813.

Buée, L., Bussière, T., Buée-Scherrer, V., Delacourte, A., and Hof, P.R. (2000). Tau protein isoforms, phosphorylation and role in neurodegenerative disorders. Brain Res. Rev. *33*, 95–130.

Carlier, M.F., and Pantaloni, D. (1981). Kinetic analysis of guanosine 5'-triphosphate hydrolysis associated with tubulin polymerization. Biochemistry *20*, 1918–1924.

Chesarone, M. a, DuPage, A.G., and Goode, B.L. (2010). Unleashing formins to remodel the actin and microtubule cytoskeletons. Nat. Rev. Mol. Cell Biol. *11*, 62–74.

Cross, R.A. (2016). Review: Mechanochemistry of the kinesin-1 ATPase. Biopolymers *105*, 476–482.

Cuevas, M. De, Tao, T., and Goldstein, L.S.B. (1992). Evidence That the Stalk of Drosophila Kinesin Heavy Chain Is an a-Helical Coiled Coil. J. Cell Biol. *116*, 957–965.

Derr, N.D., Goodman, B.S., Jungmann, R., Leschziner, A.E., Shih, W.M., and Reck-Peterson, S.L. (2012). Tug-of-War in Motor Protein Ensembles. Science (80-.). *338*, 662–666.

Desai, A., and Mitchison, T.J. (1997). Microtubule Polymerization Dynamics. Annu. Rev. Cell Dev. Biol. *13*, 83–117.

Dixit, R., Ross, J.L., Goldman, Y.E., and Holzbaur, E.L.F. (2008). Differential Regulation of Dynein and Kinesin Motor Proteins by Tau. Science (80-.). *319*, 8–11.

Dong, B., Yang, X., Zhu, S., Bassham, D.C., and Fang, N. (2015). Stochastic Optical Reconstruction Microscopy Imaging of Microtubule Arrays in Intact Arabidopsis thaliana Seedling Roots. Sci. Rep. *5*, 15694.

Dumontet, C., Durán, G.E., Steger, K.A., Murphy, G.L., Sussman, H.H., and Sikic, B.I. (1996). Differential expression of tubulin isotypes during the cell cycle. Cell Motil. Cytoskeleton *35*, 49–58.

Erickson, R.P., Jia, Z., Gross, S.P., and Yu, C.C. (2011). How molecular motors are arranged on a cargo is important for vesicular transport. PLoS Comput. Biol. *7*.

Erickson, R.P., Gross, S.P., and Yu, C.C. (2013). Filament-Filament Switching Can Be Regulated by Separation Between Filaments Together with Cargo Motor Number. PLoS One *8*, 1–8.

Fehr, A.N., Asbury, C.L., and Block, S.M. (2008). Kinesin steps do not alternate in size. Biophys. J. *94*, L20-2.

Fink, G., Hajdo, L., Skowronek, K.J., Reuther, C., Kasprzak, A.A., and Diez, S. (2009). The mitotic kinesin-14 Ncd drives directional microtubule-microtubule sliding. Nat. Cell Biol. *11*, 717–723.

Friedman, D.S., and Vale, R.D. (1999). Single-molecule analysis of kinesin motility reveals regulation by the cargo-binding tail domain. Nat. Cell Biol. *1*, 293–297.

Furuta, K., Furuta, A., Toyoshima, Y.Y., Amino, M., Oiwa, K., and Kojima, H. (2013). Measuring collective transport by defined numbers of processive and nonprocessive kinesin motors. Proc. Natl. Acad. Sci. U. S. A. *110*, 501–506.

Galmarini, C.M., Kamath, K., Vanier-Viornery, A., Hervieu, V., Peiller, E., Falette, N., Puisieux, A., Ann Jordan, M., and Dumontet, C. (2003). Drug resistance associated with loss of p53 involves extensive alterations in microtubule composition and dynamics. Br. J. Cancer *88*, 1793–1799.

Gittes, F., Mickey, B., Nettleton, J., and Howard, J. (1993). Flexural rigidity of microtubules and actin filaments measured from thermal fluctuations in shape. J. Cell Biol. *120*, 923–934.

Gomez, J.M., Chumakova, L., Bulgakova, N.A., and Brown, N.H. (2016). Microtubule organization is determined by the shape of epithelial cells. Nat. Commun. *7*, 13172.

Goodman, B.S., and Reck-Peterson, S.L. (2014). Engineering defined motor ensembles with DNA origami (Elsevier Inc.).

Gross, S.P., Welte, M.A., Block, S.M., and Wieschaus, E.F. (2002). Coordination of opposite-polarity microtubule motors. J. Cell Biol. *156*, 715–724.

Gross, S.P., Vershinin, M., and Shubeita, G.T. (2007). Cargo transport: two motors are sometimes better than one. Curr. Biol. *17*, R478-86.

Hamant, O. (2013). Cell biology: Cytoskeleton network topology feeds back on its regulation. Curr. Biol. *23*, R963–R965.

Hendricks, A.G., Holzbaur, E.L.F., and Goldman, Y.E. (2012). Force measurements on cargoes in living cells reveal collective dynamics of microtubule motors. Proc. Nat. Acad. Sci. *109*, 18447–18452.

Hirokawa, N. (1996). The molecular mechanism of organelle transport along microtubules: the identification and characterization of KIFs (kinesin superfamily proteins). Cell Struct. Funct. *21*, 357–367.

Hirokawa, N., and Tanaka, Y. (2015). Kinesin superfamily proteins (KIFs): Various functions and their relevance for important phenomena in life and diseases. Exp. Cell Res. *334*, 16–25.

Hirokawa, N., Shiomura, Y., and Okabe, S. (1988). Tau proteins: the molecular structure and mode of binding on microtubules. J. Cell Biol. *107*, 1449–1459.

Hirokawa, N., Niwa, S., and Tanaka, Y. (2010). Molecular motors in neurons: Transport mechanisms and roles in brain function, development, and disease. Neuron *68*, 610–638.

Howard, J., and Hyman, A.A. (2003). Dynamics and mechanics of the microtubule plus end. Nature *422*, 753–758.

Hunyadi, V., Chrétien, D., Flyvbjerg, H., and Jánosi, I.M. (2007). Why is the

microtubule lattice helical? Biol. Cell *99*, 117–128.

Kalil, K., and Dent, E.W. (2014). Branch management: mechanisms of axon branching in the developing vertebrate CNS. Nat. Rev. Neurosci. *15*, 7–18.

Khalil, A.S., Appleyard, D.C., Labno, A.K., Georges, A., Karplus, M., Belcher, A.M., Hwang, W., and Lang, M.J. (2008). Kinesin's cover-neck bundle folds forward to generate force. Proc. Natl. Acad. Sci. U. S. A. *105*, 19247–19252.

Klumpp, S., and Liposky, R. (2005). Cooperative cargo transport by several molecular motors. Proc. Natl. Acad. Sci. U. S. A. *102*, 17284–17289.

Kunwar, A., Vershinin, M., Xu, J., and Gross, S.P. (2008). Stepping, Strain Gating, and an Unexpected Force-Velocity Curve for Multiple-Motor-Based Transport. Curr. Biol. *18*, 1173–1183.

Kural, C., Kim, H., Syed, S., Goshima, G., Gelfand, V.I., and Selvin, P.R. (2005). Kinesin and dynein move a peroxisome in vivo: a tug-of-war or coordinated movement? Science *308*, 1469–1472.

Lakadamyali, M., Rust, M.J., Babcock, H.P., and Zhuang, X. (2003). Visualizing infection of individual influenza viruses. Proc. Natl. Acad. Sci. U. S. A. *100*, 9280–9285.

Leandro-García, L.J., Leskelä, S., Landa, I., Montero-Conde, C., López-Jiménez, E., Letón, R., Cascón, A., Robledo, M., and Rodríguez-Antona, C. (2010). Tumoral and tissue-specific expression of the major human alpha/beta-tubulin isotypes. Cytoskeleton *67*, 214–223.

Levi, V., Serpinskaya, A.S., Gratton, E., and Gelfand, V. (2006). Organelle transport along microtubules in Xenopus melanophores: evidence for cooperation between multiple motors. Biophys. J. *90*, 318–327.

Li, Q., King, S.J., Gopinathan, A., and Xu, J. (2016). Quantitative Determination of the Probability of Multiple-Motor Transport in Bead-Based Assays. Biophys. J. *110*, 2720–2728.

Mallik, R., and Gross, S.P. (2004). Molecular motors: Strategies to get along. Curr. Biol. *14*, 971–982.

Mallik, R., Rai, A.K., Barak, P., Rai, A., and Kunwar, A. (2013). Teamwork in microtubule motors. Trends Cell Biol. *23*, 575–582.

Marx, A., Müller, J., Mandelkow, E.M., Hoenger, A., and Mandelkow, E. (2006). Interaction of kinesin motors, microtubules, and MAPs. J. Muscle Res. Cell Motil. *27*, 125–137.

McKenney, R.J., Vershinin, M., Kunwar, A., Vallee, R.B., and Gross, S.P. (2010). LIS1 and NudE induce a persistent dynein force-producing state. Cell *141*, 304–

314.

Milic, B., Andreasson, J.O.L., Hancock, W.O., and Block, S.M. (2014). Kinesin processivity is gated by phosphate release. Proc. Natl. Acad. Sci. U. S. A. *111*, 14136–14140.

Miller, K.E., and Joshi, H.C. (1996). Tubulin transport in neurons. J. Cell Biol. *133*, 1355–1366.

Mitchison, T., and Kirschner, M. (1984). Dynamic instability of microtubule growth. Nature *312*, 237–242.

Mudrakola, H. V., Zhang, K., and Cui, B. (2009). Optically Resolving Individual Microtubules in Live Axons. Structure *17*, 1433–1441.

Müller, M.J.I., Klumpp, S., Lipowsky, R., Muller, M.J., Klumpp, S., and Lipowsky, R. (2008). Tug-of-war as a cooperative mechanism for bidirectional cargo transport by molecular motors. Proc. Natl. Acad. Sci. USA *105*, 4609–4614.

Nogales, E. (2001). Structural Insights Into Micrtoubule Function. Annu. Rev. Biochem *69*, 277–302.

Nogales, E. (2015). An electron microscopy journey in the study of microtubule structure and dynamics. Protein Sci. *24*, 1912–1919.

Nogales, E., Wolf, S.G., and Downing, K.H. (1998). Structureof the alpha-beta tubulin dimer by electron crystallography. Nature *391*, 199–204.

Nogales, E., Whittaker, M., Milligan, R.A., and Downing, K.H. (1999). High-resolution model of the microtubule. Cell *96*, 79–88.

Osunbayo, O., Butterfield, J., Bergman, J., Mershon, L., Rodionov, V., and Vershinin, M. (2015). Cargo transport at microtubule crossings: Evidence for prolonged tug-of-war between kinesin motors. Biophys. J. *108*, 1480–1483.

Pampaloni, F., Lattanzi, G., Jonás, A., Surrey, T., Frey, E., and Florin, E.-L. (2006). Thermal fluctuations of grafted microtubules provide evidence of a length-dependent persistence length. Proc. Natl. Acad. Sci. U. S. A. *103*, 10248–10253.

Parke, C.L., Wojcik, E.J., Kim, S., and Worthylake, D.K. (2010). ATP hydrolysis in Eg5 kinesin involves a catalytic two-water mechanism. J. Biol. Chem. *285*, 5859–5867.

Parker, A.L., Kavallaris, M., and McCarroll, J.A. (2014). Microtubules and their role in cellular stress in cancer. Front. Oncol. *4*, 153.

Petry, S., Groen, A.C., Ishihara, K., Mitchison, T.J., and Vale, R.D. (2013). Branching microtubule nucleation in xenopus egg extracts mediated by augmin and

TPX2. Cell *152*, 768–777.

Di Polo, A. (2015). Dendrite pathology and neurodegeneration: Focus on mTOR. Neural Regen. Res. *10*, 559–561.

Prager-Khoutorsky, M., Khoutorsky, A., and Bourque, C.W. (2014). Unique Interweaved Microtubule Scaffold Mediates Osmosensory Transduction via Physical Interaction with TRPV1. Neuron *83*, 866–878.

Rice, L.M., Montabana, E.A., and Agard, D.A. (2008). The lattice as allosteric effector: structural studies of alphabeta- and gamma-tubulin clarify the role of GTP in microtubule assembly. Proc. Natl. Acad. Sci. U. S. A. *105*, 5378–5383.

Rice, S., Lin, A.W., Safer, D., Hart, C.L., Naber, N., Carragher, B.O., Cain, S.M., Pechatnikova, E., Wilson-Kubalek, E.M., Whittaker, M., et al. (1999). A structural change in the kinesin motor protein that drives motility. Nature *402*, 778–784.

Rogers, A., Driver, Jonathan Constantinou, P., and Diehl, M.R. (2009). Negative interference dominates collective transport of kinesin motors in the absence of load. Phys. Chem. Chem. Phys. *11*, 4800–4803.

Ross, J.L., Ali, M.Y., and Warshaw, D.M. (2008a). Cargo transport: molecular motors navigate a complex cytoskeleton. Curr. Opin. Cell Biol. *20*, 41–47.

Ross, J.L., Shuman, H., Holzbaur, E.L.F., and Goldman, Y.E. (2008b). Kinesin and dynein-dynactin at intersecting microtubules: motor density affects dynein function. Biophys. J. *94*, 3115–3125.

Roux, A., Cappello, G., Cartaud, J., Prost, J., Goud, B., and Bassereau, P. (2002). A minimal system allowing tubulation with molecular motors pulling on giant liposomes. Proc. Natl. Acad. Sci. U. S. A. *99*, 5394–5399.

Santarella, R.A., Skiniotis, G., Goldie, K.N., Tittmann, P., Gross, H., Mandelkow, E.M., Mandelkow, E., and Hoenger, A. (2004). Surface-decoration of microtubules by human tau. J. Mol. Biol. *339*, 539–553.

Schaap, I.A.T., Carrasco, C., De Pablo, P.J., and Schmidt, C.F. (2011). Kinesin walks the line: Single motors observed by atomic force microscopy. Biophys. J. *100*, 2450–2456.

Schnorrenberg, S., Grotjohann, T., Vorbr??ggen, G., Herzig, A., Hell, S.W., and Jakobs, S. (2016). In vivo super-resolution RESOLFT microscopy of drosophila melanogaster. Elife *5*, 1–11.

Seetapun, D., Castle, B.T., McIntyre, A.J., Tran, P.T., and Odde, D.J. (2012). Estimating the microtubule GTP cap size in vivo. Curr. Biol. *22*, 1681–1687.

Shang, Z., Zhou, K., Xu, C., Csencsits, R., Cochran, J.C., and Sindelar, C. V.

(2014). High-resolution structures of kinesin on microtubules provide a basis for nucleotide-gated force-generation. Elife *3*, e04686.

Shibata, K., Miura, M., Watanabe, Y., Saito, K., Nishimura, A., Furuta, K., and Toyoshima, Y.Y. (2012). A single protofilament is sufficient to support unidirectional walking of dynein and kinesin. PLoS One *7*.

Shishido, H., Nakazato, K., Katayama, E., Chaen, S., and Maruta, S. (2010). Kinesin-Calmodulin fusion protein as a molecular shuttle. J. Biochem. *147*, 213–223.

Sinclair, G., Jordan, P., Courtial, J., Padgett, M., and Laczik, Z.J. (2004). Assembly of 3 dimensional structures using programmable holographic optical tweezers,. Opt. Express *12*, 5475–5480.

Sindelar, C. V. (2011). A seesaw model for intermolecular gating in the kinesin motor protein. Biophys. Rev. *3*, 85–100.

Song, Y., and Brady, S.T. (2015). Post-translational modifications of tubulin: Pathways to functional diversity of microtubules. Trends Cell Biol. *25*, 125–136.

Sparacino, J., Farias, M.G., and Lamberti, P.W. (2014). Effect of the microtubule-associated protein tau on dynamics of single-headed motor proteins KIF1A. Phys. Rev. E - Stat. Nonlinear, Soft Matter Phys. *89*, 1–8.

Subramanian, R., Wilson-Kubalek, E.M., Arthur, C.P., Bick, M.J., Campbell, E.A., Darst, S.A., Milligan, R.A., and Kapoor, T.M. (2010). Insights into antiparallel microtubule crosslinking by PRC1, a conserved nonmotor microtubule binding protein. Cell *142*, 433–443.

Svoboda, K., and Block, S.M. (1994). Force and velocity measured for single kinesin molecules. Cell *77*, 773–784.

Thoresen, T., and Gelles, J. (2008). Processive movement by a kinesin heterodimer with an inactivating mutation in one head. Biochemistry *47*, 9514–9521.

Toprak, E., Yildiz, A., Hoffman, M.T., Rosenfeld, S.S., and Selvin, P.R. (2009). Why kinesin is so processive. Proc. Natl. Acad. Sci. U. S. A. *106*, 12717–12722.

Uchimura, S., Oguchi, Y., Katsuki, M., Usui, T., Osada, H., Nikawa, J., Ishiwata, S., and Muto, E. (2006). Identification of a strong binding site for kinesin on the microtubule using mutant analysis of tubulin. EMBO J. *25*, 5932–5941.

Vale, R.D., Reese, T.S., and Sheetz, M.P. (1985). Identification of a novel force-generating protein, kinesin, involved in microtubule-based motility. Cell *42*, 39–50.

Verhey, K.J., and Gaertig, J. (2007). The tubulin code. Cell Cycle *6*, 2152–2160.

Vershinin, M., Carter, B.C., Razafsky, D.S., King, S.J., and Gross, S.P. (2007).

Multiple-motor based transport and its regulation by Tau. Proc. Natl. Acad. Sci. U. S. A. *104*, 87–92.

Weisenberg, R.C., Deery, W.J., and Dickinson, P.J. (1976). Tubulin-nucleotide interactions during the polymerization and depolymerization of microtubules. Biochemistry *15*, 4248–4254.

Woehlke, G., and Schliwa, M. (2000). Walking on Two Heads: the Many Talents of Kinesin. Nat. Rev. Mol. Cell Biol. *1*, 50–58.

Woehlke, G., Ruby, A.K., Hart, C.L., Ly, B., Hom-Booher, N., and Vale, R.D. (1997). Microtubule interaction site of the kinesin motor. Cell *90*, 207–216.

Xu, J., Shu, Z., King, S.J., and Gross, S.P. (2012). Tuning Multiple Motor Travel via Single Motor Velocity. Traffic *13*, 1198–1205.

Yildiz, A., Tomishige, M., Vale, R.D., and Selvin, P.R. (2004). Kinesin walks hand-over-hand. Science *303*, 676–678.

Yildiz, A., Tomishige, M., Gennerich, A., and Vale, R.D. (2008). Intramolecular Strain Coordinates Kinesin Stepping Behavior along Microtubules. Cell *134*, 1030–1041.

Young, K.G., Thurston, S.F., Copeland, S., Smallwood, C., and Copeland, J.W. (2008). INF1 is a novel microtubule-associated formin. Mol. Biol. Cell *19*, 5168–5180.

Zhu, X., Hu, R., Brissova, M., Stein, R.W., Powers, A.C., Gu, G., and Kaverina, I. (2015). Microtubules Negatively Regulate Insulin Secretion in Pancreatic Beta Cells. Dev. Cell *34*, 656–668.

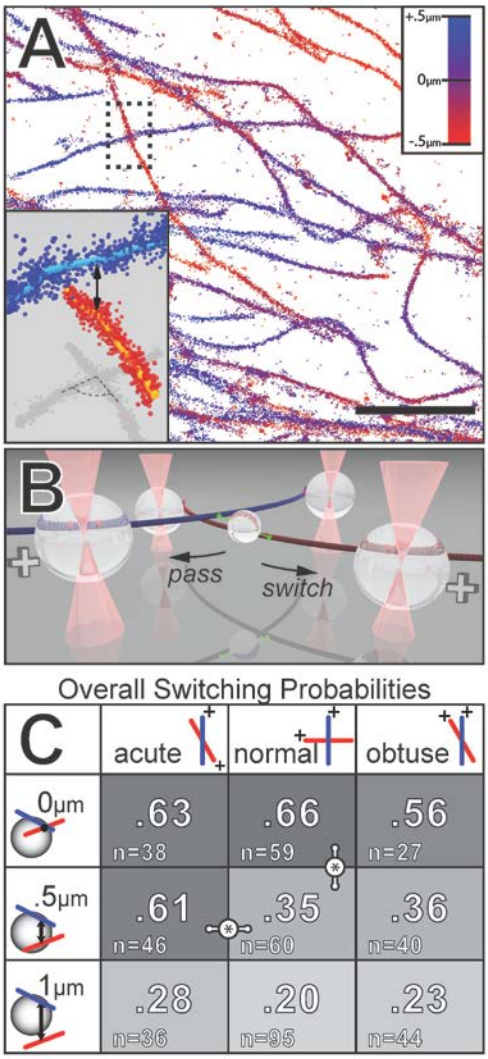

Figure 4.1: Our *in vitro* system allows us to model transport through 3D MT crossings **(A)** 3D STORM image of MT cytoskeleton from BSC-1 cell. Color coding indicates relative depth in the cell. X-Y Scale bar is 4μm. (Inset) Perspective image of the MT crossing highlighted in dashed box. Fits to MT positions (light blue and orange) are shown along with the registered photon originations (red and blue). MT separation at point of closest approach (double arrow) and MT-MT angle (protractor, dashed lines) is annotated for clarity.
(B) Illustration of *in vitro* 3D MT crossing, constructed using our technique, depicting an MC undergoing ToW. BHs (bigger beads) are permanently bound to MTs (blue and red tinted filaments bands). BHs are held in 3D via HOTs (red cones). Positive MT ends are indicated by positive signs. For clarity, we only depict two motors on the MC (smaller bead), engaged on different MTs. In our assays, cargos ultimately switch filaments, or pass through the intersection (arrows).
(C) Table showing probabilities of switching as a function of 3D MT arrangement. Higher switch rates are highlighted by darker background. Significant differences ($p < 0.05$, *Barnard's test*) are indicated by links with * symbols.

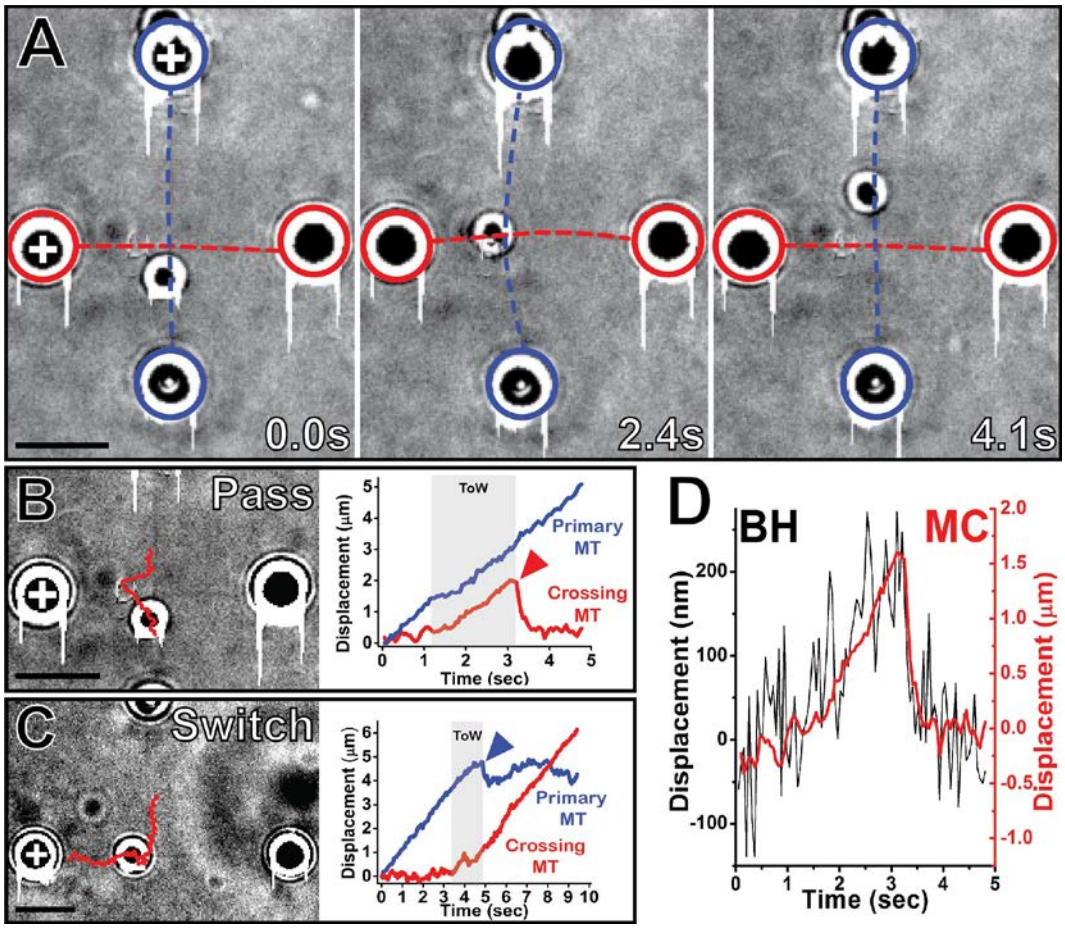

Figure 4.2: Identification and quantification of ToW

(A) Three video frames: before, during, and after ToW (left to right). Circles show BH positions in the *left panel* and are positioned identically in *middle* and *right* panels. Displacement of the top BH relative to its fiducial circle indicates presence of ToW *(middle panel)*; its original position is restored once ToW has ended (*right panel)*. White plus signs indicate the MT plus ends. Blue and red color dashed lines represent positions of both the over and underpass MTs, respectively. Frame timings shown in lower right corner.

(B) Analysis of the pass event shown in panel (A). *Left panel:* Trajectory of MC (red) overlaid on one video frame. *Right panel:* MC displacements projected along the primary (blue) and crossing (red) MT's axes. Red arrowhead highlights the snapback event which is typical of a ToW conclusion. Gray band: ToW temporal extent (~ 1.9 s).

(C) Analysis of a switch event. *Left panel:* Trajectory of MC (red) overlaid on one video frame. *Right panel:* MC displacement projected along the primary (blue) and crossing (red) MT's axes. Blue arrowhead highlights when the MC undergoes a "snapback", an event which is typical of a ToW conclusion. Gray band: ToW temporal extent (~ 1.6 s).

(D) MC displacement along the crossing (red) MT axis shown in (B) overlaid onto trace of BH's displacement from trap center, due to ToW (for the top BH in (A). *all scale bars are 5µm.*

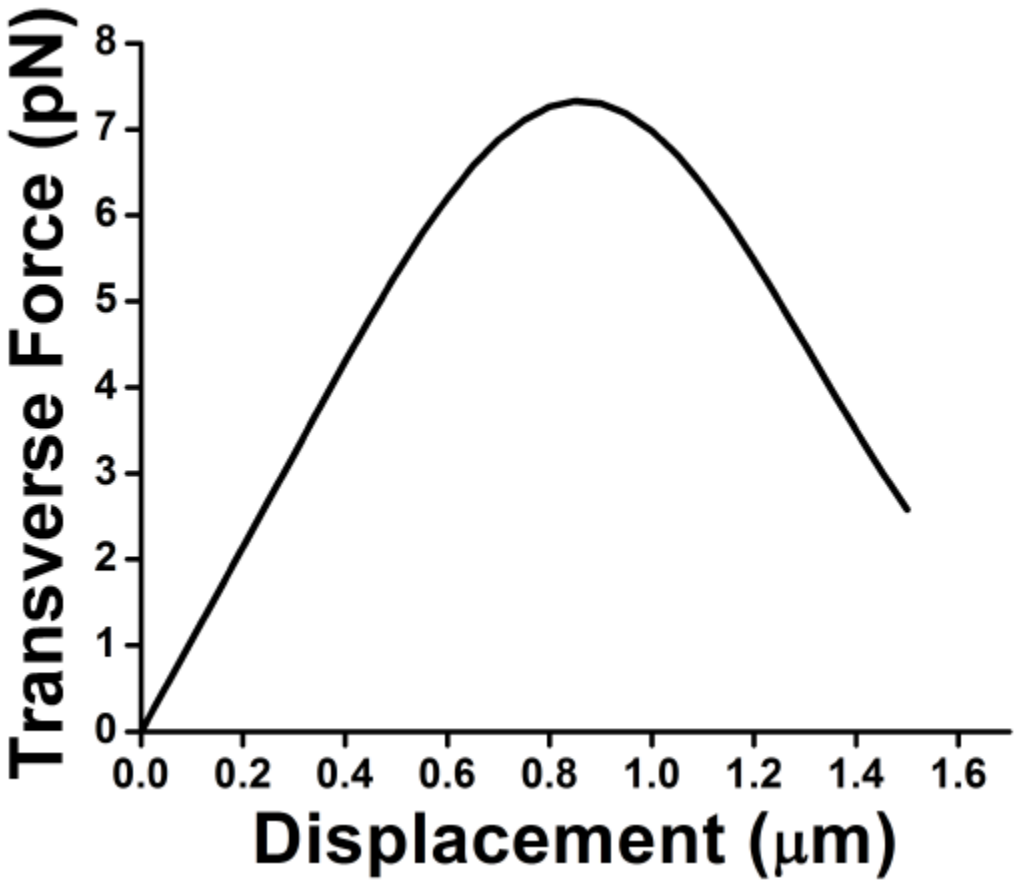

Figure 4.3: Restoring force on BH
Restoring force on a glass bead (index of refraction 1.55, 1000nm radius) exerted by the HOT for various displacements from trap center. Calculations were performed using reviously published software.

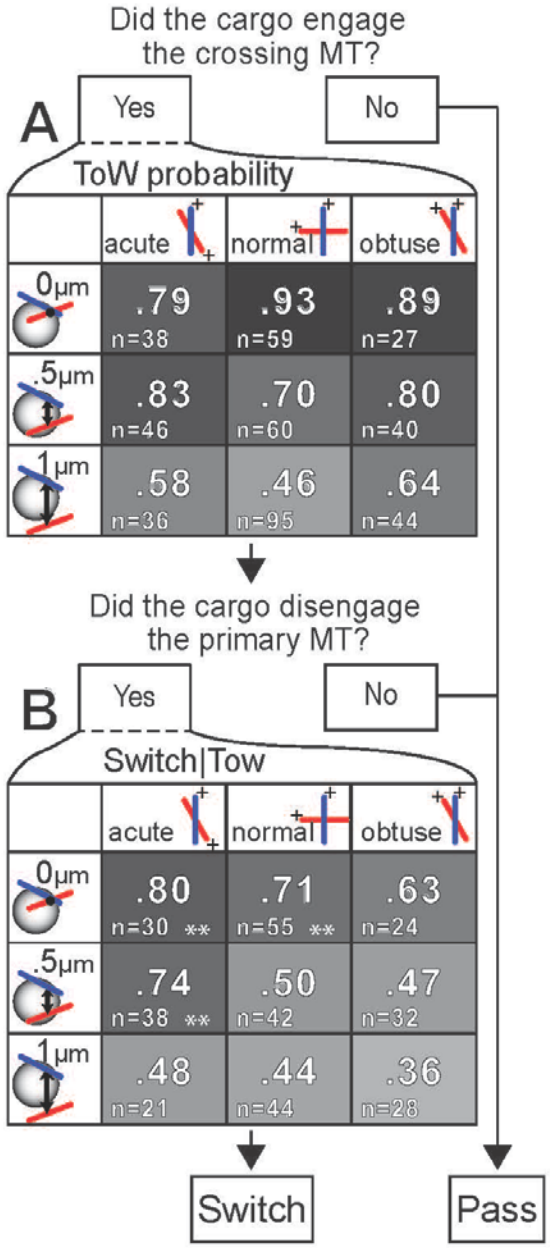

Figure 4.4: Cargo navigation flow chart, with associated probabilities
(A) Probabilities of ToW, as a function of 3D MT network geometry.
(B) Probabilities of primary MT disengagement, for ToW events only, as a function of 3D MT network geometry. ******** *indicate probability is significantly higher than 50% ($p<0.05$s, Barnard's test).*

Figure 4.5: Mathematical modeling demonstrates mechanisms of variable switch probabilities

(A) Time series of simulation snapshots. Snapshots demonstrate behavior of simulated cargos. Motors walk stochastically, pulling the cargo along with them (*left*). Motors bound to the primary MT are shown in cyan. Unbound motors are shown in green; sphere radius represents motor's reach. Teams of motors bound to opposite MTs pull against each other, demonstrating a ToW (*center*). Motors bound to the crossing MT are shown in magenta. If all motors in the primary MT team detach, the cargo continues along the crossing MT, undergoing a switch (*right*). Bead's "prime meridian" demarcated to emphasize rotational movement.

(B) Simulated probabilities to engage in ToW. Simulated ToW probabilities decrease as separation between filaments increase, and are lowest at normal geometries. For each experimental separation distance, many cargo runs were simulated for MT angles ranging from near-antiparallel (0 degrees) to near parallel (180 degrees). Probability of undergoing ToW for each is shown, with thin bars representing standard error. Curves represent quadratic fits. Experimental data are shown as crosses overlaid on simulated, with thick bars representing mean, and +/- 95% confidence interval. Experimental data points for .5μm geometries shifted slightly to aid the eye.

(C) Simulated probability to switch, given the cargo engaged in ToW. Transport outcomes for simulated cargo runs that engaged in ToW are plotted. Simulated and experimental data represented as in **(B)**.

(D) Simulated probability to switch, overall. Nonintuitive trends found in overall switching behavior are explained by multiplying probability to ToW **(B)**, by probability to switch, given ToW **(C)**. Simulated and experimental data represented as in **(B)**.

(E) Snapshot of a 0 μm ToW, normal geometry. 3D visualization reveals primary MT motors are blocked from passing the intersection by the crossing MT at 0 μm. Bound and unbound motors represented as in (**A)**.

(F) Probability to switch increases with increasing simulated fluid viscosity. Sweeping over viscosity demonstrates that passing in 0μm geometries relies upon diffusive assistance. Error bars represent standard error.

(G) Mean force exerted by the crossing MT on the cargo (.5 μm normal geometry). The crossing MT exerts significant force on the cargo at acute angles, leading to enhanced switching. Data represented as mean +/- standard error of the mean.

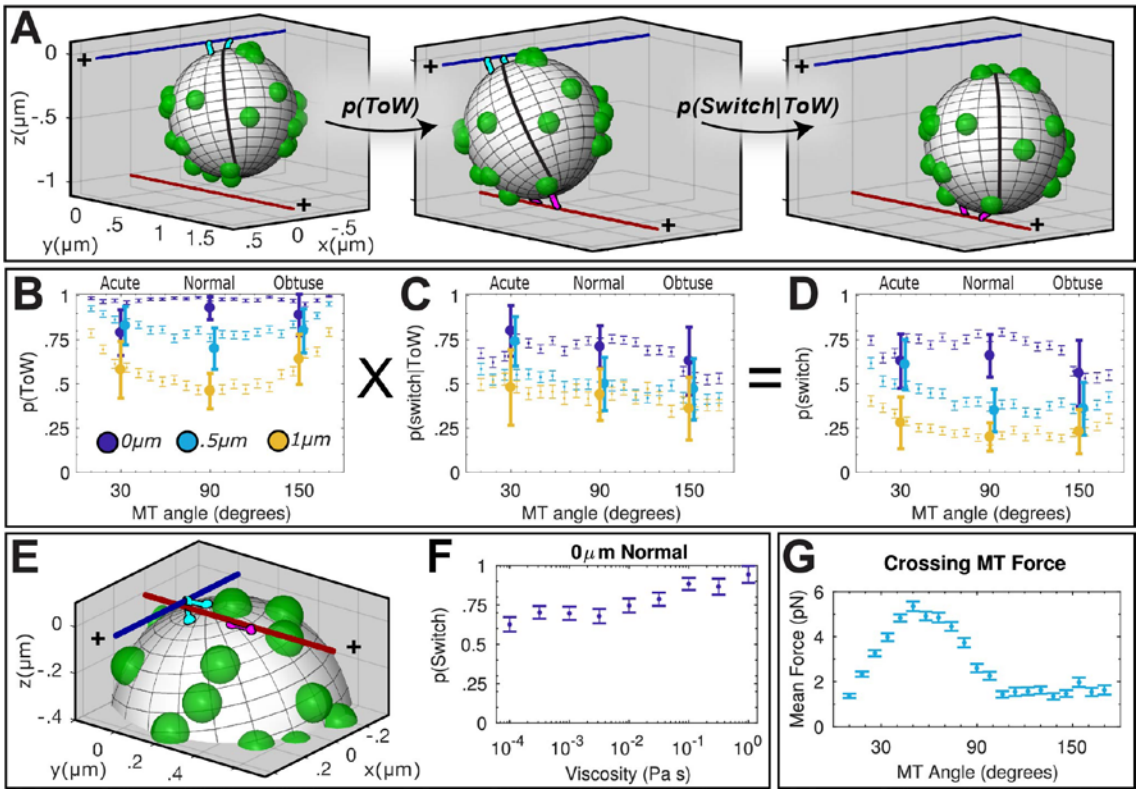
A
p(ToW)
p(Switch|ToW)
z(μm)
y(μm)
x(μm)
B
C
D
Acute
Normal
Obtuse
p(ToW)
p(switch|ToW)
p(switch)
0μm
.5μm
1μm
MT angle (degrees)
X
=
E
F
0μm Normal
p(Switch)
Viscosity (Pa s)
G
Crossing MT Force
Mean Force (pN)
MT Angle (degrees)

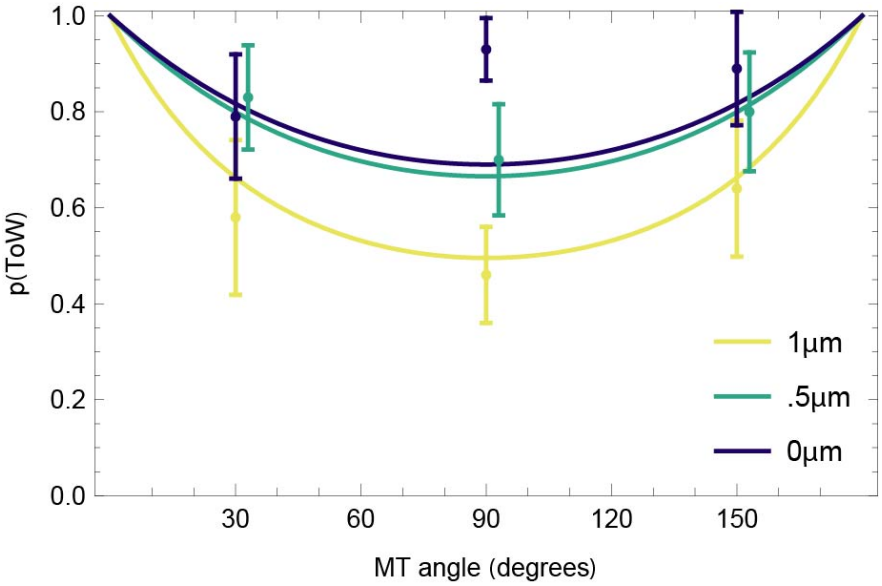

Figure 4.6: Solutions to the heuristic model for ToW probability
A heuristic model poses the probability of undergoing ToW as the the probabilityof the cargo binding (with constant binding rate) to the crossing MT before leaving the ToW zone. Solutions shown as solid curves. Bars represent 95% confidence intervals for corresponding experimental data. Bars for data at 0.5 µm shifted slightly to aid the eye.

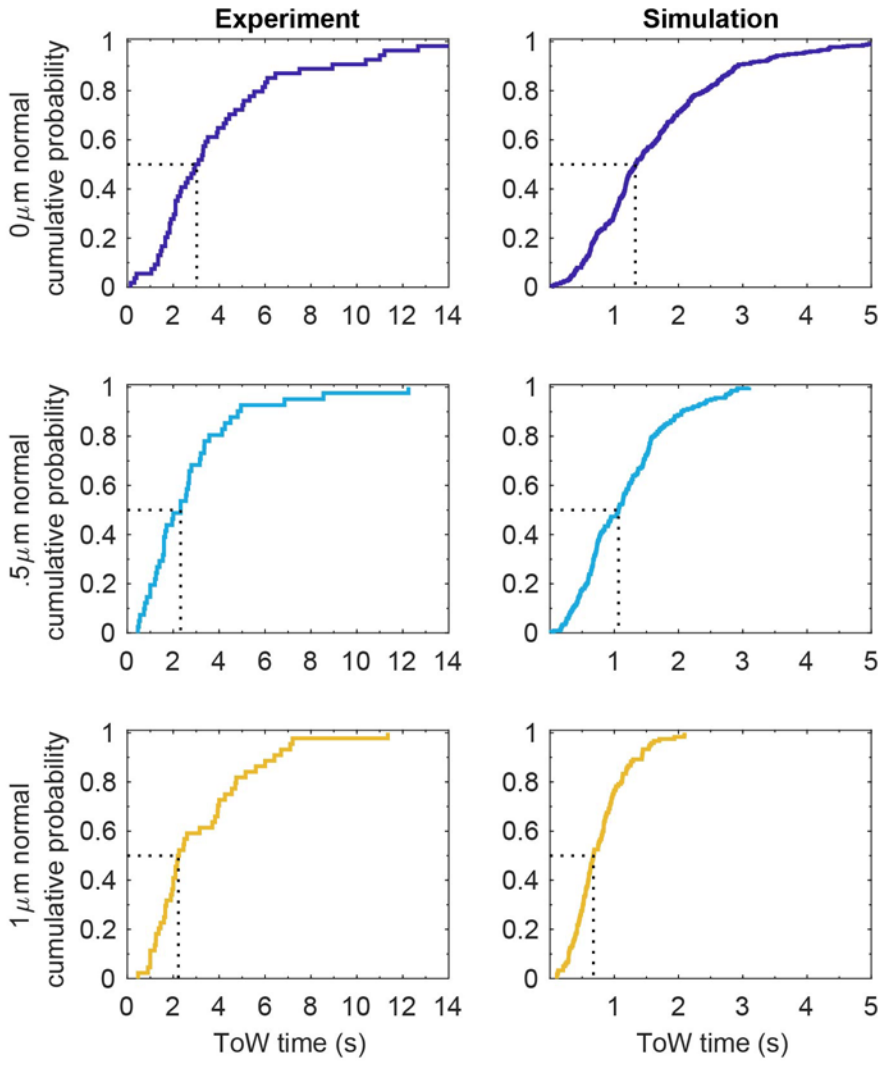

Figure 4.7: Empirical cumulative probability distributions for ToW times
The time for which cargos underwent ToW in 90 degree (normal) geometries was measured in experiments and simulations. Cumulative distributions are shown for each geometry. To aid interpretation, medians are highlighted with dotted lines.

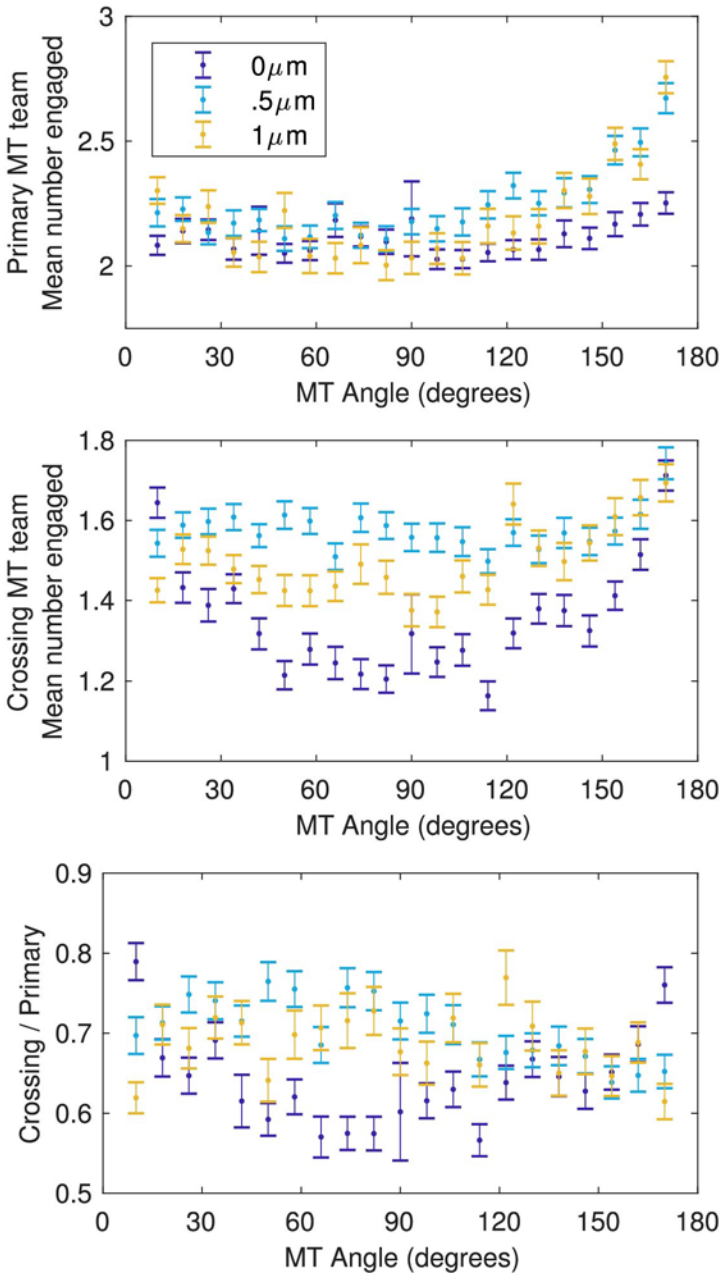

Figure 4.8: Simulated average number of motors engaged

APPENDIX

3D COMPUTER SIMULATION

SUPPLEMENT

Unpublished Data. M. Bovyn. Mathematical model of cargo Dynamics. With permission from Matthew Bovyn.

Mathematical model of cargo dynamics

1 Model description

We present a three dimensional mesoscale model for the dynamics of the cargo, which takes into account rotational and translational diffusion, as well as stochastic stepping and binding of the motors. The locations of the cargo bead and motors attached to it are governed by a set of stochastic ordinary differential equations. Binding state and location of the motor head along the microtubule (MT) are considered discrete states and transitions between them occur stochastically, modeled as Poisson processes. We construct a Monte Carlo numerical simulator, based on a hybrid Euler-Maruyama-Gillespie scheme, and simulate an ensemble of stochastic trajectories, from which we derive probabilities for tug of war and switching.

Motors in the model have two states:

Bound: A motor i is defined by two points: one represents the the motor domains, which we call the head $\vec{h}^i$; the other represents the location at which the motor is bound to the bead, which we call the anchor $\vec{a}^i$. The motor has a rate of stepping along the MT k^i_{step} and a rate of unbinding from the MT k^i_{off}.

Unbound: A motor i is defined by one point, the anchor location $\vec{a}^i$. The motor has a rate of binding to MT j, k^{ij}_{on}, that depends on its location relative to the MT as described below.

We track the anchor locations, head locations of bound motors, the location of the cargo center $\vec{c}$, and the cargo orientation $\vec{\theta}$.

1.1 Stochastic ordinary differential equations for cargo motion

We first impose force-balance on the cargo. The motion of the cargo is the inertialess regime (Reynolds number $\sim 10^{-6}$), so we omit the inertia term. A free body diagram showing the deterministic forces acting on model cargo is shown in figure S4B. All forces must balance, so

$$\sum \vec{F} = \underbrace{\sum_i \vec{F}^i_m}_{\text{motor forces}} + \underbrace{\sum_j \vec{F}^j_s}_{\text{steric forces}} + \underbrace{\vec{F}_g}_{\text{force of gravity}} + \underbrace{\vec{F}_b}_{\text{brownian force}} + \underbrace{\vec{F}_v}_{\text{viscous force}} = 0. \tag{1}$$

Similarly, we can write the balance of torques on the model cargo

$$\sum \vec{\tau} = \underbrace{\sum_i \vec{\tau}^i_m}_{\text{torque from motor forces}} + \underbrace{\vec{\tau}_b}_{\text{brownian torque}} + \underbrace{\vec{\tau}_v}_{\text{viscous torque}} = 0. \tag{2}$$

By specifying the forms of each of these forces below, we construct the equations of motion of the cargo center $\vec{c}$ and cargo orientation $\vec{\theta}$.

Motor forces

We model the force that the motor exerts on the cargo as originating from the stretch in spring-like motor stalks, based on experimental measurements [S10, S8, S3] and in line with previous models [S4, S11, S13].

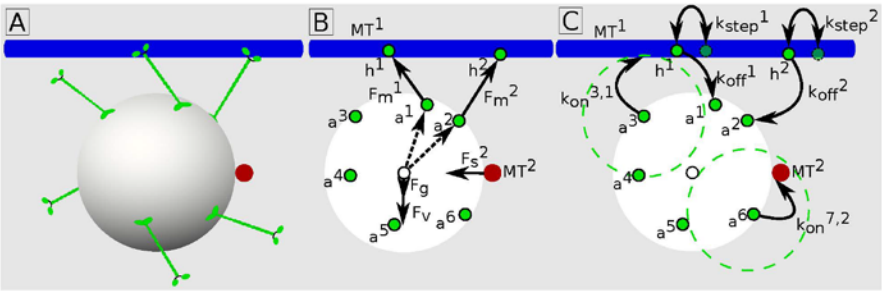

Figure S4: Diagrams of cargo dynamics
A) Schematic of a model cargo in motion. Kinesin motors are shown in green, primary MT in red, crossing MT in blue, and bead in white.
B) Free body diagram of the cargo corresponding to the cartoon in A. Anchor locations $\vec{a}^i$ and head locations $\vec{h}^i$ are shown with green dots. Cargo center location $\vec{c}$ is shown with a white dot with black outline. Forces are shown with solid arrows. Dashed arrows show the lever arm through which the motor forces exert torque.
C) Diagram showing the possible state changes corresponding to the cartoon in A. Unbound motors have on rates greater than 0 if their anchor is less than 1 motor length from a MT. Bound motors have rates of stepping and unbinding.

The form of this force is that of a one-way (tension-only) spring with rest length equal to the length of the motor. The force $\vec{F}_m^i$ exerted by motor i on the cargo bead is given by

$$\vec{F}_m^i\left(\vec{a}^i,\vec{h}^i\right)=\begin{cases}-\kappa_m\left(\left|\vec{h}^i-\vec{a}^i\right|-L\right)\left(\frac{\vec{h}^i-\vec{a}^i}{\left|\vec{h}^i-\vec{a}^i\right|}\right) & \left|\vec{h}^i-\vec{a}^i\right|>L\\ 0 & \text{otherwise}\end{cases}. \tag{3}$$

This force also exerts a torque on the cargo bead, given by the cross product of the lever arm and force vector

$$\vec{\tau}_m^i\left(\vec{a}^i,\vec{h}^i,\vec{c}\right)=\left(\vec{a}^i-\vec{c}\right)\times\vec{F}_m^i\left(\vec{a}^i,\vec{h}^i\right). \tag{4}$$

Steric forces

The cargo bead and MTs are prevented from overlapping in space by a steric force with the form of a one-way (compression-only) spring, given for MT j by

$$\vec{F}_s^j(\vec{c})=\begin{cases}-\kappa_s\left(R-\left|\vec{r}(\vec{c},j)\right|\right)\left(\frac{\vec{r}(\vec{c},j)}{\left|\vec{r}(\vec{c},j)\right|}\right) & \left|\vec{r}(\vec{c},j)\right|<R\\ 0 & \text{otherwise}\end{cases}, \tag{5}$$

where $\vec{r}(\vec{p},j)$ is a vector from point $\vec{p}$ to the nearest point on the MT. This is found by computing the perpendicular distance from $\vec{p}$ to the MT surface, given by

$$\vec{r}(\vec{p},j)=\left(1-\frac{R_{\mathrm{MT}}}{\left|\left(\vec{x}_{\mathrm{MT}}^j-\vec{p}\right)-\left(\left(\vec{x}_{\mathrm{MT}}^j-\vec{p}\right)\cdot\vec{d}_{\mathrm{MT}}^j\right)\vec{d}_{\mathrm{MT}}^j\right|}\right)\left(\left(\vec{x}_{\mathrm{MT}}^j-\vec{p}\right)-\left(\left(\vec{x}_{\mathrm{MT}}^j-\vec{p}\right)\cdot\vec{d}_{\mathrm{MT}}^j\right)\vec{d}_{\mathrm{MT}}^j\right). \tag{6}$$

Force of gravity

The experimental system uses a silica bead with density greater than water as the cargo. Therefore the model cargo experiences a small but significant force due to gravity given by the buoyancy of the bead,

$$\vec{F}_g = \frac{4}{3}\pi R^3(\rho_b - \rho_w)\vec{g}, \tag{7}$$

where ρ_b and ρ_w are the mass densities of the silica bead and water, respectively.

Brownian force

The Brownian force $\vec{F}_b$ is a random variable with mean 0 and variance $2k_BT\xi$, where ξ is the drag coefficient and k_BT is the thermal energy unit. Specifically,

$$\left\langle \vec{F}_b \right\rangle = \vec{0} \tag{8}$$

$$\left\langle \vec{F}_b(t) \cdot \vec{F}_b(s) \right\rangle = 2(k_BT)(6\pi\eta R)\delta(t-s) \tag{9}$$

where we have inserted the translational drag coefficient of a sphere at low Reynold's number and $\delta(x)$ is the Dirac delta function.

Similarly, the brownian torque on the bead is a random variable characterized by

$$\langle \vec{\tau}_b \rangle = \vec{0} \tag{10}$$

$$\langle \vec{\tau}_b(t) \cdot \vec{\tau}_b(s) \rangle = 2(k_BT)(8\pi\eta R^3)\delta(t-s). \tag{11}$$

Viscous force

In the low Reynolds limit, linear drag dominates. The drag on the cargo is thus given by Stokes' Law,

$$\vec{F}_v = -6\pi\eta R\frac{\mathrm{d}\vec{c}(t)}{\mathrm{d}t}. \tag{12}$$

The viscous torque is given by the rotational analogue to Stokes' Law,

$$\vec{\tau}_v = -8\pi\eta R^3\frac{\mathrm{d}\vec{\theta}(t)}{\mathrm{d}t}. \tag{13}$$

Construction and discretization of the stochastic ordinary differential equations

With the forms of forces known, we rewrite equations 1 and 2 as a pair of coupled ordinary stochastic differential equations

$$\frac{\mathrm{d}\vec{c}(t)}{\mathrm{d}t} = \frac{1}{6\pi\eta R}\left(\sum_i \vec{F}_m^i\left(\vec{a}^i(t), \vec{h}^i(t)\right) + \sum_j \vec{F}_s^j(\vec{c}(t)) + \vec{F}_g\right) + \frac{1}{6\pi\eta R}\vec{F}_b(t) \tag{14}$$

and

$$\frac{\mathrm{d}\vec{\theta}(t)}{\mathrm{d}t} = \frac{1}{8\pi\eta R^3}\left(\sum_i \vec{\tau}_m^i\left(\vec{a}^i(t), \vec{h}^i(t), \vec{c}(t)\right)\right) + \frac{1}{8\pi\eta R^3}\vec{\tau}_b(t), \tag{15}$$

Equation 14 is a specific implementation of the overdamped Langevin equation, used in Brownian dynamics. Equation 15 is its rotational counterpart.

We discretize these equations according to the Euler-Maruyama method. For an update from the nth timestep at time t_n to the next time t_{n+1} with $\Delta t \equiv t_{n+1} - t_n$, the discretization is

$$\vec{c}(t_{n+1}) = \vec{c}(t_n) + \frac{1}{6\pi\eta R}\left(\sum_i \vec{F}_m^i\left(\vec{a}^i(t_n), \vec{h}^i(t_n)\right) + \sum_j \vec{F}_s^j(\vec{c}(t_n)) + \vec{F}_g\right)\Delta t + \sqrt{2\frac{k_BT}{6\pi\eta R}\Delta t}\,\vec{G}_c(t_n) \tag{16}$$

and

$$\vec{\theta}(t_{n+1}) = \vec{\theta}(t_n) + \frac{1}{8\pi\eta R^3}\left(\sum_i \vec{\tau}_m^i\left(\vec{a}^i(t_n), \vec{h}^i(t_n), \vec{c}(t_n)\right)\right)\Delta t + \sqrt{2\frac{k_B T}{8\pi\eta R^3}\Delta t}\,\vec{G}_\theta(t_n). \tag{17}$$

where $\vec{G}_c^n$ and $\vec{G}_\theta^n$ are two mutually uncorrelated vectors of three independently and identically distributed gaussian random variables with mean 0 and variance 1.

Update of anchor locations

Since the motors are statically bound to the bead, the change in their locations is fully defined by the change in the location of the center of the bead $\vec{c}(t_{n+1}) - \vec{c}(t_n)$ and the change in the orientation of the bead $\vec{\theta}(t_{n+1}) - \vec{\theta}(t_n)$.

The change in the bead orientation $\vec{\theta}(t_{n+1}) - \vec{\theta}(t_n)$ corresponds to a vector pointed along the axis of rotation of the bead with a length corresponding to the magnitude of the rotation in radians. This vector can be converted into a rotation matrix $\mathbf{M}_R(t_n)$. The next location of anchor i is then calculated by finding

$$\vec{a}^i(t_{n+1}) = \vec{a}^i(t_n) + (\vec{c}(t_{n+1}) - \vec{c}(t_n)) + \left(\mathbf{M}_R(t_n)\left(\vec{a}^i(t_n) - \vec{c}(t_n)\right) + \vec{c}(t_n)\right). \tag{18}$$

1.2 Poisson processes

We model all state transitions in the system as Poisson processes, diagrammed in figure S4C. Experiments have reported exponential distributions of times between steps [S2] and times before unbinding [S14]. This is also the most basic assumption we can make for times before binding.

Stepping

Kinesin motors step processively along MT tracks in a hand-over-hand fashion, with each motor domain taking 16 nm steps [S23] that move the center of mass of the motor forward by 8 nm [S21]. The rate at which the motor steps, and thus the motor velocity, depends on the load the motor is stepping against in a way well modeled as

$$k_{\text{step}}^i = \begin{cases} \frac{v}{d}\left(1 - F_m^i/F_s\right)^w & F_m^i < F_s \\ 0 & F_m^i \geq F_s \end{cases}, \tag{19}$$

as described in [S12].

When a motor steps, it is moved forward along the direction of the MT j to which it is bound by the step distance d. This translates to an update of the head position

$$\vec{h}^i(t_{n+1}) = \vec{h}^i(t_n) + d\left(\vec{d}_{\text{MT}}^j\right). \tag{20}$$

Unbinding

Kinesin unbinds from the MT with a rate dependent on the force experienced by the motor. Measurements have shown that unbinding rate increases exponentially below stall [S17]. Above stall, measurements have shown that unbinding rate increases only slowly with increasing force [S14]. Therefore, we state the unbinding rate as

$$k_{\text{off}}^i = \begin{cases} \epsilon_0 \exp\left(F_m^i/F_d\right) & F_m^i \leq F_s \\ a + bF_m^i & F_m^i > F_s \end{cases}. \tag{21}$$

When a motor unbinds, it is simply put into the unbound state as defined at the beginning of this section.

Binding

The conditions which govern the rate of binding to the MT are not well known. In the absence of detailed experimental elucidation, we make only the most basic assumptions possible: the motor domains must be

able to reach the MT to bind, and, if this condition is met, the motor binds with a constant rate. This translates to an on rate for motor i to MT j given by

$$k_{\text{on}}^{i,j} = \begin{cases} \pi_0^{\text{micro}} & \left|\vec{r}\left(\vec{a}^i, j\right)\right| \leq L \\ 0 & \text{otherwise} \end{cases} \tag{22}$$

where $\vec{r}\left(\vec{a}^i, j\right)$ is given by equation 6.

When a motor i binds to MT j, the head location is placed at the location on the MT nearest the anchor location $\vec{a}^i$, given by

$$\vec{h}^i(t_{n+1}) = \vec{a}^i(t_n) + \vec{r}\left(\vec{a}^i(t_n), j\right). \tag{23}$$

2 Numerical simulation of the model

Section 1 outlines a numerical scheme for updating for the model's dynamic variables in equations 16, 17 and 18 over a timestep Δt. We simulate the model forward in time using these equations. Time steps are chosen dynamically. The largest stable time step for the Euler-Maruyama scheme is given by ξ/κ, where ξ is the drag coefficient and κ is the spring constant of the stiffest operating spring. The maximum time step is chosen based on the springs active during that step. The equivalent stiffness of multiple active motor springs is taken into account, but the steric spring in equation 5 remains by far stiffest in the system if it is active.

For each timestep, we generate exponential random variables from distributions with means set by each Poisson rate, given in equations 19, 21, and 22, as in the Gillespie (next-event) algorithm. If any of these times are smaller than the maximum stable time step, the smallest generated time is chosen. If the smallest generated time came from an unbinding rate, a state change is implemented at the end of the update step by setting the motor to the unbound state. If this time came from a stepping rate or binding rate, the update occurs by equation 20 or 23, respectively. If no generated time is shorter than the maximum stable time step, the update is done with the maximum stable time step and there is no state change. The memoryless property of the exponential distributions which underlie the Poisson processes ensure that these substeps do not change the overall dynamics.

The numerical simulation is written in C. It takes approximately 0.5 s to simulate 1 s of cargo motion with a 3.3 GHz Intel Core i5 processor (single thread).

2.1 Model parameters

The kif5A motors used in experiments are members of the well studied kinesin-1 family. As such, many of the model parameters have been estimated in previous experiments. The parameters used to simulate the model are given in table S1. There are two parameters in the model not well constrained by experiments in the literature: the number of motors on a cargo, N, and the on rate of a motor given that it is close enough to the MT to bind, π_0^{micro}.

2.2 Initial conditions

Beads are incubated with motors in solution to produce experimental cargos. We assume this process produces beads with motors uniformly distributed on their surface as supported by experimental evidence in [S16]. Therefore, we generate random positions for motor anchors uniformly distributed on the surface of the bead.

Simulated cargos are initially placed just below the primary MT and far enough from the intersection that the cargo can not reach both MTs simultaneously (section 3.3 and figure S9). This distance is a function of the MT geometry and is given by equation 24. All cargos begin the simulation with one motor attached to the MT. This motor is selected at random and the cargo is rotated so its anchor is next to the MT.

2.3 Special case of 0 µm geometries

As discussed in the main text, in 0 µm geometries the crossing MT presents a steric barrier to the progress of the primary MT motor team. To modify the simulation to incorporate these effects, motors walking along the

Parameter	Description	Value	Notes
N	Number of motors on the bead	30	Determined by fit to experiments in this paper
κ_m	Kinesin stalk spring constant	$320\,\mathrm{pN\,\mu m^{-1}}$	Measured in [S10, S8, S3]
L	Kinesin length	80 nm	Measured in [S7, S19]
π_0^{micro}	Base binding rate (microscopic)	$10\,\mathrm{s^{-1}}$	Determined by fit to experiments in this paper. Lower bound estimated in [S15, S9]
ϵ_0	Base unbinding rate	$0.7\,\mathrm{s^{-1}}$	Estimated from run lengths [S1, S17, S16]
a	Superstall unbinding rate intercept parameter	$1.07\,\mathrm{s^{-1}}$	Measured in [S14]
b	Superstall unbinding rate slope parameter	$0.186\,\mathrm{s^{-1}\,pN^{-1}}$	Measured in [S14]
F_s	Stall force	5 pN	Measured in [S3, S22, S14, S17]
F_d	Critical detachment force	4 pN	Measured in [S18, S14, S17]
v	Unloaded motor velocity	$1\,\mathrm{\mu m\,s^{-1}}$	From model cargo velocities measured here
d	Step size	8 nm	Measured in [S21]
w	Curvature index	2	Measured in [S22, S5]
κ_s	Steric spring constant	$40000\,\mathrm{pN\,\mu m^{-1}}$	Set high enough to ensure the cargo spends no more than 5 time steps in a row intersecting a MT
R	Cargo bead radius	0.5 µm	Provided by manufacturer
ρ_b	Cargo bead density	$2.0\,\mathrm{g/cm^3}$	Provided by manufacturer
ρ_w	Density of experimental medium	$1.0\,\mathrm{g/cm^3}$	Estimated as density of water
$\vec{g}$	Vector for gravitational acceleration	(0,0,-9.8) $\mathrm{m/s^2}$	
η	Viscosity of fluid	8.5×10^{-4} Pa s	Estimated as viscosity of water
T	Temperature of the fluid	293 K	Experiments performed at room temperature
R_{MT}	MT radius	12 nm	Measured in [S6]
$\vec{x}^1_{\mathrm{MT}}$	Defining point for primary MT	(0,0,0)	
$\vec{d}^1_{\mathrm{MT}}$	Defining direction vector for primary MT	(1,0,0)	
$\vec{x}^2_{\mathrm{MT}}$	Defining point for crossing MT		Varied in simulations
$\vec{d}^2_{\mathrm{MT}}$	Defining direction vector for crossing MT		Varied in simulations

Table S1: List of parameters. Values listed are used for all simulations unless explicitly stated.

primary MT were prevented from stepping into the volume occupied by the crossing MT. Unbound motors were also prevented from binding if their head would be placed in the volume occupied by the crossing MT. These restrictions were lifted if the cargo was above the plane of the MTs.

2.4 Fitting unknown parameters to data

While the behavior of bound kinesins under load has been intensely investigated, the binding rate of kinesin to the MT is less understood. A binding rate of $5\,s^{-1}$ has been estimated based fits to other models [S15, S9], but these estimates include diffusion processes and do not directly translate to the microscopic binding rate we use here. We define the microscopic binding rate as the rate at which a motor binds the MT given it is possible for the motor heads to reach the MT, thus $5\,s^{-1}$ represents a lower bound.

It was unfeasible to directly determine the total number of motors bound to experimental beads. Modeling binding of motors to beads in solution using Poisson statistics has enabled estimation of motor number when there are few motors (binding fraction $< .9$)[S16], but the experiments in this work are done in the many motors regime (binding fraction indistinguishable from 1) so motor number cannot be determined from binding fraction. Simple binding of motors to cargo beads in solution predicts a total numbers of motors which is Poisson distributed [S20]. We simulate with only a single number of total motors, which we identify with the mean of the experimental Poisson distribution. We do not expect this model simplification to impact the results due to the peaked nature of the Poisson distribution.

Fit to tug of war probability

To determine values for the unknown parameters (total number of motors N and microscopic on rate π_0^{micro}), we fit to the probability of cargos to undergo ToW.

Ensembles of cargo trajectories were simulated for combinations of total number of motors and off rate and assayed for ToW as outlined in section 3.1. We survey the fit to ToW probability for experimental conditions and compare the simulated probability with the experimentally measured one. We exclude 0 µm separation geometries, as prominent steric effects which might obscure the fit are present (see figure S9). Furthermore, ToW probability is symmetric about the normal (see figures S8A and S9), so angled geometries were grouped to increase statistical power. This leaves us with four experimental conditions to fit, as shown in figure S5.

The experimental geometries provide redundant information about best fit parameters, with many parameter combinations fitting all four. Therefore we examine other experimental observations to select a set of parameters.

Robust transport constraint

Experimental cargos are often observed to travel along the entire length of microtubules (10 µm or greater). Because single motor off rates are constrained by single molecule run length experiments [S1, S17, S16], we can constrain acceptable combinations of motor number and on rate by looking at simulated cargo run length. An ensemble of cargos were simulated without the crossing MT and allowed to walk until either all motors detached from the MT or a motor head passed a point 10 µm from where the cargo started. Results are shown in figure S6. In experiments, roughly half of cargos were observed to travel the entire length of the MT.

Force constraint

In experiments, force production of cargos was limited by the strength of the optical traps securing the bead handles. If generated forces were large enough, the forward bead handle was pulled out of its optical trap. Data for these cargos was discarded. The maximum force the bead handles could withstand was about 7 pN, greater than the single motor stall force but less than the maximal stall force of two motors[MB1]. Because experimental cargos often do not stall and geometric effects tend to keep all motors from exerting their maximal force on the bead handle at once, we expect there to be 2-3 motors exerting force on the bead handle.

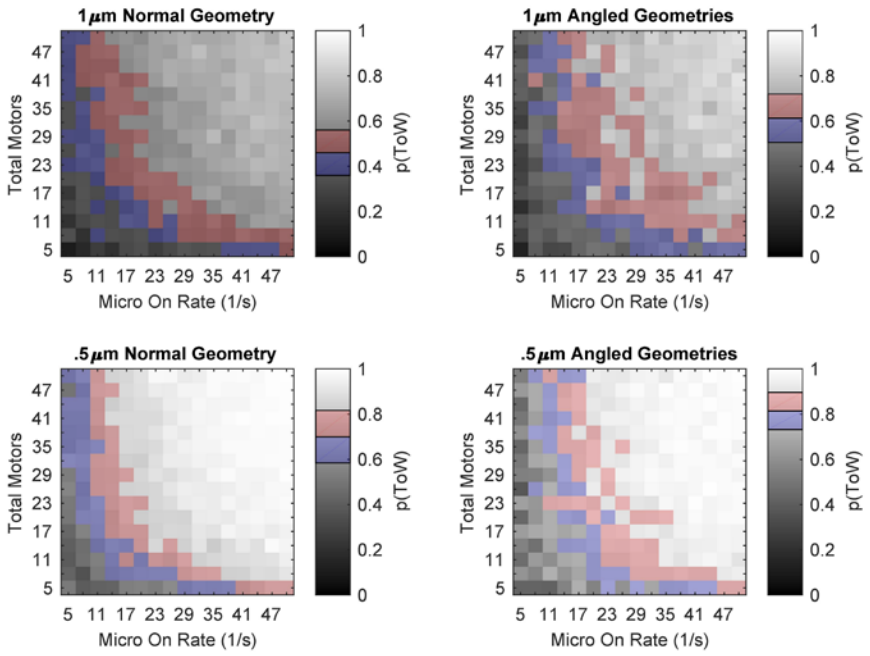

Figure S5: ToW probabilities for varying combinations of the unknown parameters
ToW probabilities are shown as grey scale heat maps for a range of parameter combinations. Those which yielded ToW probabilities within the experimental 95% confidence interval are highlighted in color. Red highlighting indicates a probability above the experimental mean, blue highlighting below. All probabilities gathered from 300 cargos. For angled geometries, 150 acute runs were grouped with 150 obtuse runs.

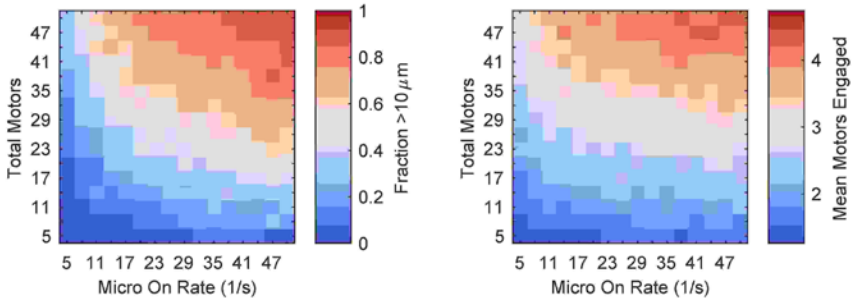

Figure S6: Experimental observations inform selection of unknown parameters
Left: Fraction of cargos that travelled more than 10 microns are shown as a heat map for a range of parameter combinations. Fractions determined by simulation of 300 cargos.
Right: Mean number of motors engaged on the MT at steady state is shown as a heat map for a range of parameter combinations. Values represent mean over 200 cargos. The number of motors engaged was assessed 1.5 s after the run began for each cargo. This time was long enough for cargos of all parameter combinations to reach steady state.

Because simulated MTs are not dynamic, average or maximal simulated forces do not necessarily correspond to those one would expect to see experimentally. Therefore we investigate the number of motors simultaneously engaged on the MT at steady state, which estimates an upper limit for the number of motors simultaneously producing force.

To find the number of motors engaged on the MT, we simulate cargos walking along the primary MT without interference from a crossing MT. First, we simulate an ensemble of cargos and examine the average number of motors engaged over the ensemble as time progresses. After an initial transient, there is a period of time where neither the number of engaged motors nor the standard deviation thereof changes much. We call the average number of engaged motors during this time the steady state number. A survey of parameter combinations revealed that 1.5 s was long enough for cargos to come to steady state. Then, we check the average number of engaged motors at steady state for many parameter combinations. The results are shown in figure S6.

Parameter selection

A survey of figures S5 and S6 reveals that only parameter combinations with high numbers of total motors and low on rate fit the ToW probability and also match estimated run length and number of engaged motors. A manual search of parameter combinations in this region yielded $N = 30$, $k_{\text{on}}^{\text{micro}} = 10\,\text{s}^{-1}$ as the best fit.

3 Model Results

Cargo trajectories were simulated forward in time as described in sections 1 and 2. Simulations were performed using the parameter values listed in table S1. All parameter values used except microscopic on rate and total number of motors on the cargo are established in the literature or set by the experiment. Section 2.4 details how values for the unknown parameters were fit.

An ensemble of trajectories was simulated for a given geometry. Trajectories were categorized as described below, and probabilities of ToW and switching were derived. As shown in figure S7, the general behavior of simulated cargos was the same as experimental ones.

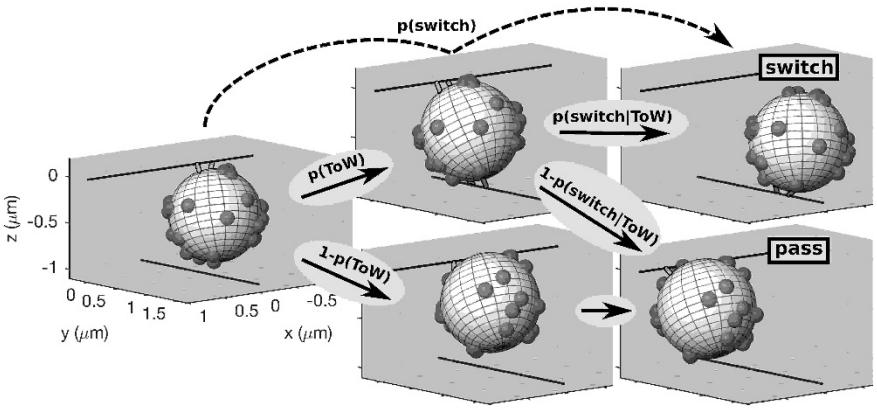

Figure S7: Snapshots from simulated cargo trajectories
During a simulation run, cargos begin outside the ToW zone with a single motor attached to the MT. Motors step stochastically, moving the cargo along the MT (*left*). The cargo diffuses translationally as well as rotationally. When the cargo encounters the crossing MT, motors may bind and induce a ToW with p(ToW) (*center,top*) or the cargo may go by the MT without any motors binding(*center,bottom*). Cargos which do not ToW always pass. ToWs may end in the primary MT motor team becoming detached, resulting in a switch, with probability p(switch|ToW) (*right,top*). Otherwise, the motor team on the crossing MT detaches, resulting in a pass (*right,bottom*). To switch, a cargo must undergo ToW, then the crossing MT team must win the ToW. Therefore, the overall probability of switching p(switch) in given by p(ToW) $\times$ p(switch|ToW).

3.1 Categorization of trajectories

Simulated trajectories were categorized using rules intended to emulate experimentally observed markers. Simulations began with the cargo outside of the ToW zone (section 3.3 and figure S9) and ended one of three ways: by the cargo detaching from the MT, by the cargo leaving the ToW zone on the primary MT, or by the cargo leaving the ToW zone on the crossing MT. The latter two cases were categorized as passes and switches, respectively. If the cargo detached from the primary MT before going by the intersection point, the run was discarded. If the cargo passed the intersection on the primary MT, but detached before leaving the ToW zone, the run was counted as a pass. Similarly, if the cargo was walking on the crossing MT but detached before leaving the ToW zone, the run was counted as a switch. Experimental runs were categorized using the same criteria.

Simulated cargos were marked as undergoing ToW when motors were attached to both MTs simultaneously for more than 0.25 s. This time was selected as the minimum time in which a ToW would be detectable experimentally, given the camera frame rate. ToW time was measured as the total time during which motors were attached to both MTs and average values during ToW were accumulated during this period.

3.2 Encounter outcome dependance on MT geometry

Ensembles of trajectories were simulated for varying separations and angles between the MTs. MT separations were varied from 0 µm to 1 µm, corresponding to 0 to 1 times the cargo diameter. Angles between the MTs were varied from nearly parallel to nearly anti-parallel. Figure S8 shows the resulting ToW and switch probabilities, along with the conditional probability of switching, given the cargo underwent ToW.

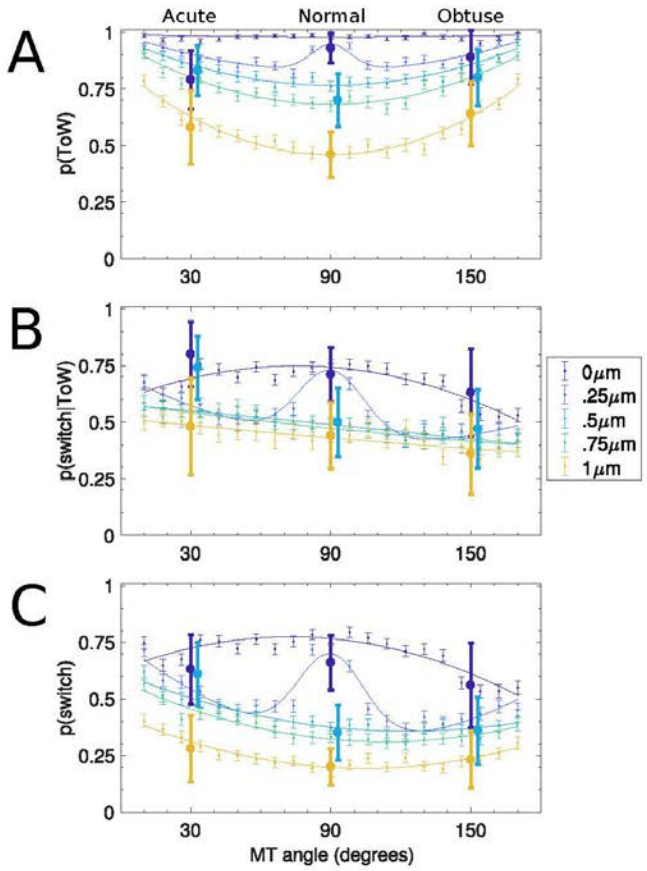

Figure S8: Probabilities of ToW and switching given ToW combine to explain switch probability
A: ToW probability as a function of the angle between the MTs is shown for separation distances corresponding to 0, 1/4, 1/2, 3/4 and 1 times the cargo diameter. Simulated data shown with thin bars representing standard error. Curves represent quadratic fits to simulated data for all but 0.25 µm separation distance, which is fit to a quadratic with an overlaid gaussian. Experimental data shown with think bars representing 95% confidence interval.
B: Conditional probability of switching, given the cargo undergoes ToW. Data represented as in *A*.
C: Overall switch probability. Data represented as in *A*

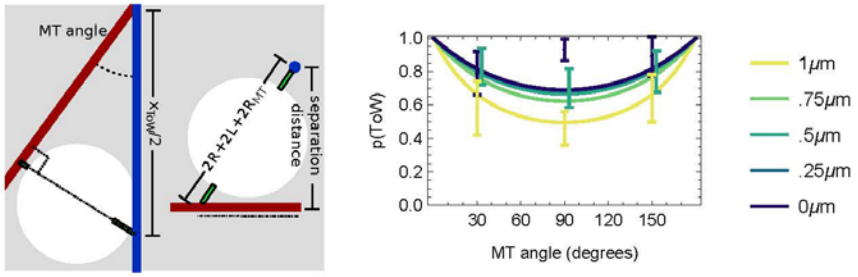

Figure S9: A heuristic model matches qualitative features of ToW probability
Left: Diagram of the ToW zone. The ToW zone is defined as the distance along the primary MT in which the cargo can reach the crossing MT. Its length was calculated geometrically and is given by equation 24. Primary MT is shown in blue, crossing MT in red, motors in green and cargo in white.
Right: Solutions to the heuristic model for ToW probability. The heuristic model poses the probability of undergoing ToW as the the probability of the cargo binding (with constant binding rate) to the crossing MT before leaving the ToW zone and is given in equation 25. Experimental probabilities are shown with error bars representing 95% confidence interval. Bars for data at 0.5 μm shifted slightly to aid the eye. Solutions plotted with $k_{\text{on}}^{\text{macro}}$ set to $1\,\text{s}^{-1}$.

3.3 Explanation of ToW probability

In agreement with intuition, ToW probability increases with the distance the cargo must travel while able to reach both MTs simultaneously, which we call the ToW zone, denoted x_{ToW}. The extent of the ToW zone was calculated from geometry diagrammed in figure S9, and is given by

$$x_{\text{ToW}} = 2\frac{\sqrt{4(L+R+R_{MT})^2 - ((\vec{x}_{\text{MT}}^1 - \vec{x}_{\text{MT}}^2)\cdot\hat{z})^2}}{\left\|\vec{d}_{\text{MT}}^1 \times \vec{d}_{\text{MT}}^2\right\|} = 2\frac{\sqrt{4(L+R+R_{MT})^2 - (\text{separation distance})^2}}{\sin(\text{MT angle})}. \tag{24}$$

The probability a cargo will undergo ToW can then be understood as a competition between the rate at which the cargo binds to the crossing MT, which happens at a rate which we denote $k_{\text{on}}^{\text{macro}}$, and the rate it leaves the ToW zone, which happens at a rate given by the cargo velocity (equal to the maximum single motor velocity v) divided by the ToW zone length. Thus,

$$p(\text{ToW}) = \frac{k_{\text{on}}^{\text{macro}}}{k_{\text{on}}^{\text{macro}} + \frac{v}{x_{\text{ToW}}}}. \tag{25}$$

The rate at which the cargo attaches to the crossing MT, $k_{\text{on}}^{\text{macro}}$, is in general a complex function of geometry as well as motor and cargo parameters. However, for this heuristic analysis we assume it is constant across different geometries. If we fit the macro on rate to the experimental data on ToW probability, we recover the qualitative features of the full simulation result as shown in figure S9.

Steric effects strongly influence ToW probabilities in 0 μm and 0.25 μm geometries

A comparison of figures S9 and S8A reveals that the heuristic model captures the features of ToW probability for MT separations 0.5 μm and greater very well. However, it fails to reproduce features of the simulated data at 0.25 μm and 0 μm. This failure shows that the peak in ToW probability near the normal for 0.25 μm separation and the overall high ToW probability at 0 μm must result from effects not considered in the heuristic model. As discussed in the main text, steric interactions play a large role.

3.4 Explanation of conditional probability of switching given ToW

The complex dependence of conditional probability of switching on geometry is not intuitive and warrants further investigation. To this end, we show the mean number of motors engaged on each MT during ToW, the mean forces exerted on the motor teams during ToW, the ToW time, and how each of these depends on the MT geometry in figure S10. Below we explain the behavior of the simulated conditional probability of switching on geometry using these results.

1 µm near-normal geometries

At 1 µm separation distance, the cargo can not sterically interact with both MTs at once. Since forces exerted by the MTs are minimal (figure S10C), motor teams in these ToWs pull directly on each other, as evidenced by high forces on the motor teams and a ratio near 1, shown in figure S10B. Furthermore, ToW times are short (figure S10D), meaning the crossing MT team often only gets one chance to cause a switch. One might expect, then, that since the ratio of crossing MT to primary MT motor number is $\approx .7$ (figure S10A), switches would happen about 30% of the time. However, a ToW between motor teams of different numbers is not directly determined by motor numbers. The slow increase of unbinding rate above stall gives the smaller team a significant chance to win the ToW, leading to an overall probability of switching higher than 30%, but still below 50%.

1 µm acute geometries

Conditional probabilities of switching at 1 µm are slightly higher for acute geometries than they are near the normal. As in the latter, motors pull directly on each other during ToWs, evidenced by high forces in figure S10B. However, an asymmetry exists between a ToW won by the crossing MT motor team and the primary MT motor team in acute geometries. When the primary MT motor team wins a ToW, the cargo continues on through the ToW zone (which is longer for more acute geometries, see equation 24). During this time motors may again bind to the crossing MT, giving another chance for a switch. Evidence of this effect can be seen in the longer ToW times shown in figure S10D. However, when the crossing MT team wins a ToW, the cargo is likely to diffuse down and away from the primary MT and avoid rebinding. This effect drives switching up slightly for acute geometries compared to near-normal.

1 µm obtuse

Unlike in near-normal and acute geometries at 1 µm, motors in obtuse geometries feel low average forces, as shown in figure S10B. ToW times are long, as seen in figure S10D, because MT alignment is close to parallel and motors walk in nearly the same direction. Motors do not feel significant load until the cargo has moved far enough from the intersection that the distance from MT to MT is greater than twice the bead diameter. These long periods of walking under low force turn the ToW into a competition of processivity as much as force. While a smaller motor team can compete against a larger motor team in a force competition, processivity grows quickly with motor number, so larger motor teams are more likely to win a processivity competition. Because there are on average more motors on the primary MT team, the probability of switching goes down as the distance walked goes up with more obtuse angles.

0.5 µm near-normal geometries

In 0.5 µm geometries, the cargo must hurdle up and over the crossing MT to pass. If the cargo is underneath the primary MT, the primary MT motors are loaded as they pull the cargo into the crossing MT, but the cargo cannot pass the intersection until it is out from underneath the primary MT. In near-normal geometries, the crossing MT team assists this process by pulling the cargo out toward the plus end of the crossing MT. While this is taking place, the primary MT motors continue to be loaded. This load sometimes causes primary MT motors to unbind, leading to a weaker team on average. As crossing MT motors walk, the force from the primary MT motors is shifted from the crossing MT to the crossing MT motor team. In the end, this interaction has similar dynamics to the ones described in the 1 µm near-normal geometries, albeit with a primary MT motor team that is now weaker on average. This slightly biases the ToW toward the crossing MT team relative to 1 µm near-normal geometries, resulting in a ToW probability near 50%.

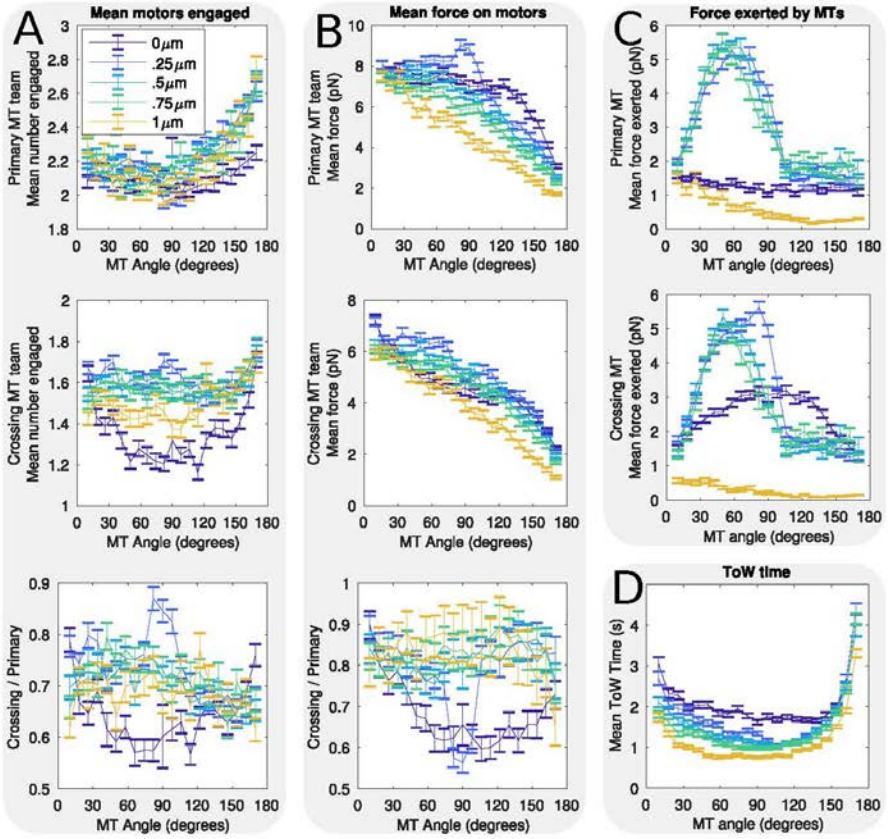

Figure S10: Numbers engaged, forces and ToW times explain conditional probability of switching
A: Mean number of motors engaged during ToW for primary and crossing MT teams. The numbers are shown as a function of MT angle. Below, the ratio of mean motors engaged on the crossing MT to the primary MT is shown. Separation distances are colored as described in the legend in the top panel of *A*. Error bars represent standard error of the mean.
B: Mean force experienced by the motor teams on the primary and crossing MTs during ToW. Forces are shown as a function of angle. Below, the ratio of the forces on the crossing MT team to the forces on the primary MT team is displayed. Data represented as in *A*.
C: Mean steric force exerted by the primary and crossing MTs during ToW. Forces shown as a function of angle and represented as in *A*. *D*: Mean ToW time as a function of angle between the MTs. ToW time is the total time motors are engaged on both MTs. Data represented as in *A*.

0.5 µm acute geometries

Unlike in near-normal geometries at 0.5 µm, the crossing MT motors do not aid hurdling behavior in acute geometries. In fact, they impede hurdling; when the crossing MT motors engage, they act to wedge the cargo between the MTs, described as "chop-sticking" in the main text. This effect can be seen in the high forces exerted by the MTs at these geometries shown in figure S10C. Because crossing MT motors impede hurdling and the cargo must travel beyond the intersection to pass, crossing MT motors often get multiple chances to cause a switch, indicated by long ToW times in figure S10D. This leads to the conditional probability of switching rising 50%.

0.5 µm obtuse geometries

As in 0.5 µm near-normal geometries, crossing MT motors aid hurdling in 0.5 µm obtuse geometries. Additionally, like obtuse geometries at 1 µm separation distance, ToW times are long (figure S10D) and forces are low (figure S10B). As described, this biases the ToW toward the larger motor team on the primary MT and results in less switching.

0.25 µm and 0.75 µm geometries

The conditional probability of switching in 0.25 µm and 0.75 µm geometries is similar to that of 0.5 µm geometries, indicating the same mechanisms are at play. There is a significant deviation at angles near the normal in 0.25 µm geometries. At these angles, the crossing MT becomes a very effective barrier to progress of the cargo. Because the crossing MT is above the cargo equator, steric forces from the crossing MT tend to push the cargo back down, causing it to get stuck below the intersection. This effect can be seen in the high MT forces near normal in figure S10C. Stuck cargos are more likely to switch, leading to an overall high switching probability.

0 µm near-normal geometries

As explained in the main text, cargos may only pass two ways in 0 µm geometries: by the cargo hurdling up and over the crossing MT, or by monkey-barring. Since cargos experience a gravitational force, they are likely to encounter the intersection below the crossing MT and not be able to hurdle. Because successful monkey-barring is a process which requires two rare events, this leads to a high probability of switching.

0 µm acute geometries

Because the ToW zone is longer in acute geometries than near-normal, cargos are more likely to undergo several ToW events. This is reflected in the long ToW times at acute geometries shown in figure S10D. In the opposite effect of that in 0.5 µm geometries, these longer ToWs lead to less switching in 0 µm geometries. This is because these longer ToWs give the cargo more chances to monkey-bar and pass the intersection.

0 µm obtuse geometries

Conditional probability of switching falls as angles become closer to parallel for 0 µm separation distance, and approaches 50%. The forces on the cargo in these geometries are such that motors on the crossing MT tend to pull the cargo up and over the top of the intersection. This leads to greater ease of passing because the crossing MT no longer blocks progress of the primary MT motor team when the cargo is above the plane.

References

[S1] Steven M. Block, Lawrence S. B. Goldstein, and Bruce J. Schnapp. "Bead movement by single kinesin molecules studied with optical tweezers". In: *Nature* 348.6299 (Nov. 1990), pp. 348–352. ISSN: 0028-0836. DOI: 10.1038/348348a0. URL: http://www.nature.com/doifinder/10.1038/348348a0.

[S2] N J Carter and R A Cross. "Mechanics of the kinesin step." In: *Nature* 435.7040 (2005), pp. 308–12. ISSN: 1476-4687. DOI: 10.1038/nature03528. URL: http://www.ncbi.nlm.nih.gov/pubmed/15902249.

[S3] Chris M. Coppin et al. "The load dependence of kinesin's mechanical cycle". In: *Proc. Natl. Acad. Sci. USA* 94.August (1997), pp. 8539–8544. ISSN: 0027-8424. DOI: 10.1016/S0006-3495(96)79323-2.

[S4] Robert P. Erickson et al. "How Molecular Motors Are Arranged on a Cargo Is Important for Vesicular Transport". In: *PLoS Computational Biology* 7.5 (May 2011). Ed. by Andreas R. Bausch, e1002032. ISSN: 1553-7358. DOI: 10.1371/journal.pcbi.1002032. URL: http://dx.plos.org/10.1371/journal.pcbi.1002032.

[S5] Todd L. Fallesen, Jed C. MacOsko, and G. Holzwarth. "Force-velocity relationship for multiple kinesin motors pulling a magnetic bead". In: *European Biophysics Journal* 40.9 (2011), pp. 1071–1079. ISSN: 01757571. DOI: 10.1007/s00249-011-0724-1.

[S6] A V Grimstone and A Klug. "Observations on the substructure of flagellar fibres". In: *J Cell Sci* 1.3 (1966), pp. 351–362. ISSN: 0021-9533. URL: http://www.ncbi.nlm.nih.gov/pubmed/5968986%7B%5C%%7D5Cnhttp://www.ncbi.nlm.nih.gov/entrez/query.fcgi?cmd=Retrieve%7B%5C&%7Ddb=PubMed%7B%5C&%7Ddopt=Citation%7B%5C&%7Dlist%7B%5C_%7Duids=5968986.

[S7] Nobutaka Hirokawa et al. "Submolecular domains of bovine brain kinesin identified by electron microscopy and monoclonal antibody decoration". In: *Cell* 56.5 (1989), pp. 867–878. ISSN: 00928674. DOI: 10.1016/0092-8674(89)90691-0.

[S8] Sylvia Jeney et al. "Mechanical Properties of Single Motor Molecules Studied by Three-Dimensional Thermal Force Probing in Optical Tweezers". In: *ChemPhysChem* 5.8 (Aug. 2004), pp. 1150–1158. ISSN: 1439-4235. DOI: 10.1002/cphc.200301027. URL: http://doi.wiley.com/10.1002/cphc.200301027.

[S9] Stefan Klumpp and Reinhard Lipowsky. "Cooperative cargo transport by several molecular motors." In: *Proceedings of the National Academy of Sciences of the United States of America* 102.48 (Nov. 2005), pp. 17284–9. ISSN: 0027-8424. DOI: 10.1073/pnas.0507363102. URL: http://www.ncbi.nlm.nih.gov/pubmed/16287974%20http://www.pubmedcentral.nih.gov/articlerender.fcgi?artid=PMC1283533.

[S10] H Kojima et al. "Mechanics of single kinesin molecules measured by optical trapping nanometry". In: *Biophysical Journal* 73.4 (1997), pp. 2012–2022. ISSN: 00063495. DOI: 10.1016/S0006-3495(97)78231-6. URL: http://linkinghub.elsevier.com/retrieve/pii/S0006349597782316.

[S11] Christian B. Korn et al. "Stochastic simulations of cargo transport by processive molecular motors". In: *Journal of Chemical Physics* 131.24 (2009). ISSN: 00219606. DOI: 10.1063/1.3279305. arXiv: 0912.2171.

[S12] Ambarish Kunwar and Alexander Mogilner. "Robust transport by multiple motors with nonlinear force-velocity relations and stochastic load sharing." In: *Phys. Biol.* 7.1 (2010), p. 16012. ISSN: 1478-3975. DOI: 10.1088/1478-3975/7/1/016012.

[S13] Ambarish Kunwar et al. "Stepping, Strain Gating, and an Unexpected Force-Velocity Curve for Multiple-Motor-Based Transport". In: *Current Biology* 18.16 (2008), pp. 1173–1183. ISSN: 09609822. DOI: 10.1016/j.cub.2008.07.027.

[S14] A. Kunwar et al. "Mechanical stochastic tug-of-war models cannot explain bidirectional lipid-droplet transport". In: *Proceedings of the National Academy of Sciences* 108.47 (2011), pp. 18960–18965. ISSN: 0027-8424. DOI: 10.1073/pnas.1107841108.

[S15] C. Leduc et al. "Cooperative extraction of membrane nanotubes by molecular motors". In: *Proceedings of the National Academy of Sciences* 101.49 (Dec. 2004), pp. 17096–17101. ISSN: 0027-8424. DOI: 10.1073/pnas.0406598101. URL: http://www.ncbi.nlm.nih.gov/pubmed/15569933%20http://www.pubmedcentral.nih.gov/articlerender.fcgi?artid=PMC535380%20http://www.pnas.org/cgi/doi/10.1073/pnas.0406598101.

[S16] Qiaochu Li et al. "Quantitative Determination of the Probability of Multiple-Motor Transport in Bead-Based Assays". In: *Biophysical Journal* 110.12 (2016), pp. 2720–2728. ISSN: 00063495. DOI: 10.1016/j.bpj.2016.05.015.

[S17] Bojan Milic et al. "Kinesin processivity is gated by phosphate release." In: *Proceedings of the National Academy of Sciences of the United States of America* 111.39 (Sept. 2014), pp. 14136–40. ISSN: 1091-6490. DOI: 10.1073/pnas.1410943111. URL: http://www.ncbi.nlm.nih.gov/pubmed/25197045%20http://www.pubmedcentral.nih.gov/articlerender.fcgi?artid=PMC4191751.

[S18] M J Schnitzer, K Visscher, and S M Block. "Force production by single kinesin motors." In: *Nature cell biology* 2.10 (2000), pp. 718–23. ISSN: 1465-7392. DOI: 10.1038/35036345. URL: http://www.ncbi.nlm.nih.gov/pubmed/11025662.

[S19] Jonathan M. Scholey et al. "Identification of globular mechanochemical heads of kinesin". In: *Nature* 338.6213 (Mar. 1989), pp. 355–357. ISSN: 0028-0836. DOI: 10.1038/338355a0. URL: http://www.nature.com/doifinder/10.1038/338355a0.

[S20] Karel Svoboda and Steven M. Block. "Force and velocity measured for single kinesin molecules". In: *Cell* 77.5 (1994), pp. 773–784. ISSN: 00928674. DOI: 10.1016/0092-8674(94)90060-4.

[S21] Karel Svoboda et al. "Direct observation of kinesin stepping by optical trapping interferometry". In: *Nature* 365.6448 (Oct. 1993), pp. 721–727. ISSN: 0028-0836. DOI: 10.1038/365721a0. URL: http://www.nature.com/doifinder/10.1038/365721a0.

[S22] K Visscher, M J Schnitzer, and S M Block. "Single kinesin molecules studied with a molecular force clamp." In: *Nature* 400.6740 (1999), pp. 184–9. ISSN: 0028-0836. DOI: 10.1038/22146. URL: http://www.ncbi.nlm.nih.gov/pubmed/10408448.

[S23] Ahmet Yildiz et al. "Kinesin walks hand-over-hand." In: *Science (New York, N.Y.)* 303.5658 (2004), pp. 676–8. ISSN: 1095-9203. DOI: 10.1126/science.1093753. arXiv: arXiv:1011.1669v3. URL: http://www.ncbi.nlm.nih.gov/pubmed/14684828.